



Cite this: *Chem. Soc. Rev.*, 2023, 52, 2193

## Electrochemical C–N coupling of CO<sub>2</sub> and nitrogenous small molecules for the electrosynthesis of organonitrogen compounds

Xianyun Peng,<sup>ID ab</sup> Libin Zeng,<sup>ab</sup> Dashuai Wang,<sup>ID ab</sup> Zhibin Liu,<sup>ab</sup> Yan Li,<sup>ad</sup> Zhongjian Li,<sup>ID ab</sup> Bin Yang,<sup>ab</sup> Lecheng Lei,<sup>ab</sup> Liming Dai<sup>ID \*d</sup> and Yang Hou<sup>ID \*abc</sup>

Electrochemical C–N coupling reactions based on abundant small molecules (such as CO<sub>2</sub> and N<sub>2</sub>) have attracted increasing attention as a new “green synthetic strategy” for the synthesis of organonitrogen compounds, which have been widely used in organic synthesis, materials chemistry, and biochemistry. The traditional technology employed for the synthesis of organonitrogen compounds containing C–N bonds often requires the addition of metal reagents or oxidants under harsh conditions with high energy consumption and environmental concerns. By contrast, electrosynthesis avoids the use of other reducing agents or oxidants by utilizing “electrons”, which are the cleanest “reagent” and can reduce the generation of by-products, consistent with the atomic economy and green chemistry. In this study, we present a comprehensive review on the electrosynthesis of high value-added organonitrogens from the abundant CO<sub>2</sub> and nitrogenous small molecules (N<sub>2</sub>, NO, NO<sub>2</sub><sup>−</sup>, NO<sub>3</sub><sup>−</sup>, NH<sub>3</sub>, etc.) via the C–N coupling reaction. The associated fundamental concepts, theoretical models, emerging electrocatalysts, and value-added target products, together with the current challenges and future opportunities are discussed. This critical review will greatly increase the understanding of electrochemical C–N coupling reactions, and thus attract research interest in the fixation of carbon and nitrogen.

Received 28th October 2022

DOI: 10.1039/d2cs00381c

rsc.li/chem-soc-rev

### 1. Introduction

The continuous combustion and utilization of natural fuels have resulted in numerous issues, including CO<sub>2</sub> emission-induced global climate change, environmental destruction, and potential depletion of non-renewable resources. With the depletion of fossil energy and the increasing environmental issues, it is urgent to seek and develop clean, cheap, and efficient renewable energy sources. In this context, the direct transformation of earth-abundant small molecules, such as N<sub>2</sub>, CO<sub>2</sub>, and H<sub>2</sub>O, into high-value-added chemicals, fuels, and fertilizers has received extensive attention.<sup>1–3</sup> However, the industrial synthesis of high-value-added chemicals from earth-abundant small molecules requires harsh conditions with high energy consumption, exacerbating the energy crisis and environmental problems.<sup>4</sup> In this case, electrocatalysis powered by renewable electricity can lower the energy barrier of the reaction, enabling

the highly efficient synthesis of valuable chemicals under milder conditions.<sup>5–9</sup> Currently, the research on electrosynthesis focuses on the efficient resource utilization of abundant gaseous molecules through electrocatalytic activation and immobilization.<sup>10–13</sup> For example, the electrocatalytic conversion of CO<sub>2</sub> into fuels or value-added chemical products provides a carbon-neutral cycle, which can mitigate the rapid consumption of fossil resources and reduce CO<sub>2</sub> emissions.<sup>14–19</sup>

Based on the “carbon neutrality” policy, the capture, transformation, and utilization of CO<sub>2</sub> have become a hot topic, which are also urgent problems to be solved. In particular, the electrochemical CO<sub>2</sub> reduction reaction (ECRR) powered by renewable energy sources has attracted considerable interest, providing possibilities for energy storage and artificial closure of the carbon cycle under mild conditions.<sup>20–25</sup> A large number of advantages have been envisioned for the wide and deep research on the electrocatalytic conversion of CO<sub>2</sub> into chemicals and fuels via C–O, C–N, and C–C bond formation.<sup>26–30</sup>

Compared to the pure ECRR technology, the combination of ECRR with the electrochemical N<sub>2</sub> reduction reaction (ENRR) using earth-abundant and nitrogenous small molecules (N<sub>2</sub>, NO, NO<sub>2</sub><sup>−</sup>, NO<sub>3</sub><sup>−</sup>, NH<sub>3</sub>, etc.) as a nitrogen source and renewable energy has been demonstrated as a promising approach for the sustainable production of valuable organonitrogen

<sup>a</sup> College of Chemical and Biological Engineering, Zhejiang University, Hangzhou 310027, China. E-mail: [yhou@zju.edu.cn](mailto:yhou@zju.edu.cn)

<sup>b</sup> Institute of Zhejiang University - Quzhou, Quzhou, 324000, China

<sup>c</sup> Donghai Laboratory, Zhoushan, China

<sup>d</sup> Australian Carbon Materials Centre (A-CMC), School of Chemical Engineering, University of New South Wales, Sydney, NSW, 2052, Australia.

E-mail: [l.dai@unsw.edu.au](mailto:l.dai@unsw.edu.au)

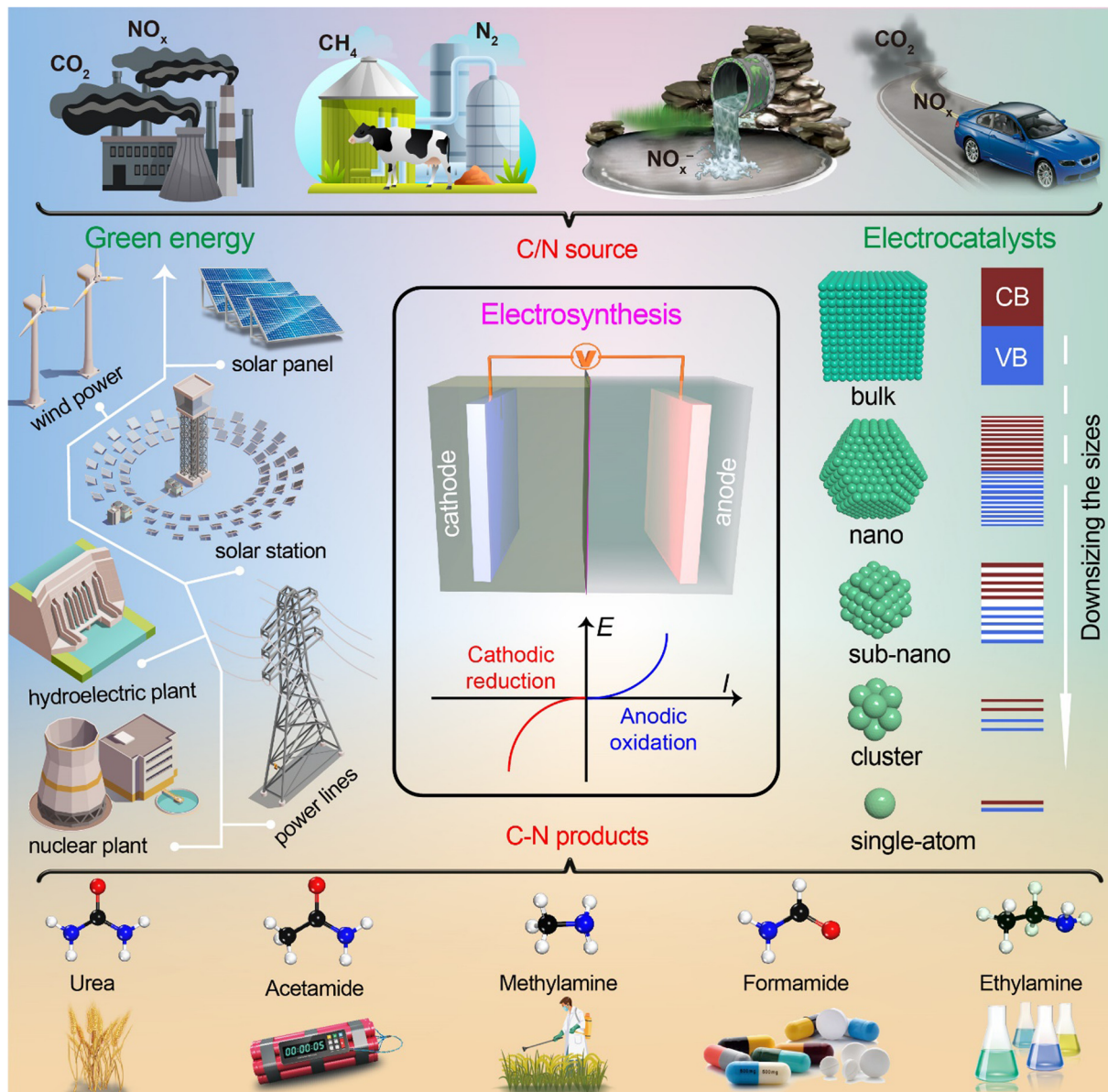


**Fig. 1** Schematic illustration of the electrosynthesis of organonitrogen compounds *via* C–N coupling reaction of CO<sub>2</sub> and nitrogenous small molecules (N<sub>2</sub>, NO, NO<sub>2</sub><sup>-</sup>, NO<sub>3</sub><sup>-</sup>, NH<sub>3</sub>, etc.) driven by renewable electricity. The black, blue, red, and white balls represent C, N, O, and H atoms, respectively.

compounds, as displayed in Fig. 1.<sup>29–32</sup> Considering that N<sub>2</sub> (making up 80% of air) is an appealing nitrogen source, the ENRR driven by renewable electricity has been proposed as a promising alternative to the energy-intensive Haber–Bosch process for artificial N<sub>2</sub> fixation to produce ammonia (NH<sub>3</sub>) by harnessing N<sub>2</sub> and H<sub>2</sub>O feedstocks under mild conditions. However, its efficiency is severely limited by the intrinsic chemical inertness, low solubility of N<sub>2</sub> (0.02 v/v, 298 K, 1 atm), and high dissociation energy of the N≡N triple bond (941 kJ mol<sup>-1</sup>).<sup>33,34</sup>

Encouragingly, compared to the non-polar N<sub>2</sub>, its derivatives (NO, NO<sub>2</sub><sup>-</sup>, NO<sub>3</sub><sup>-</sup>, etc.) have a relatively low dissociation energy (NO<sub>3</sub><sup>-</sup>: 204 kJ mol<sup>-1</sup> and NO<sub>2</sub><sup>-</sup>: 207 kJ mol<sup>-1</sup>) and high water-solubility,<sup>35,36</sup> which are more suitable nitrogen sources for the

electrosynthesis of organonitrogen compounds *via* the C–N coupling reaction. Alternatively, pesticide and fertilizer residues and industrial wastewater contain large amounts of nitrogen pollutants (such as NO<sub>2</sub><sup>-</sup> and NO<sub>3</sub><sup>-</sup>), which enter the groundwater and human body, causing various diseases such as methemoglobinemia.<sup>37,38</sup> The conventional way to remove nitrate from wastewater is to convert it to dinitrogen, which is known as “denitrification”.<sup>39</sup> However, the electrochemical conversion strategy is more appealing, not only reducing the formation of acid rain, photochemical smog, and depletion of the ozone layer due to the presence of NO, but also avoiding the consumption of a reducing agent (NH<sub>3</sub>) during the selective catalytic reduction process, which is one of the state-of-the-art and widely commercialized technologies

for abating nitrogen oxides in the flue gases from coal-fuelled power plants, automobiles, and industrial facilities.<sup>39,40</sup> Therefore, coupling CO<sub>2</sub> with nitrogenous small molecules (NO, NO<sub>2</sub><sup>-</sup>, NO<sub>3</sub><sup>-</sup>, NH<sub>3</sub>, etc.) is a promising alternative path from the standpoint of “turn waste into treasure” for cost-effective electrosynthesis and environmental remediation, especially when driven by renewable energy.

Although C–N coupling reaction experiments can yield high-value-added organic compounds containing carbon/nitrogen (urea, amide, amine, acetamide, ethylamine, formamide, glycine, methylamine, etc.), demonstrating potential as a sustainable strategy, CO<sub>2</sub> and nitrogenous small molecules (N<sub>2</sub>, NO, NO<sub>2</sub><sup>-</sup>, NO<sub>3</sub><sup>-</sup>, NH<sub>3</sub>, etc.) have mainly been studied as carbon or nitrogen sources for separate electrochemical reduction reactions thus far. Alternatively, the production of C–N bond-containing compounds can not only significantly improve the industrial value and the energy density of the target products for widespread applications in chemical synthesis, pharmaceutical chemistry, agriculture, and the aerospace industry, but also simultaneously decrease the need for the transportation of the products from simple ECRR and ENRR processes.

Currently, there are several high-quality review papers available in the literature on electrochemical C–N coupling reactions,<sup>26,29,30,41–44</sup> outlining the related reaction mechanisms and potential design principles for advanced electrocatalysts and emphasizing the effects of different reactors on the coupling reactions, which can be beneficial to scientists specializing in this field by reinforcing their expertise. However, considering that readers who have no experience in chemistry, physics, materials, chemical engineering, environmental and energy technologies, and catalysis will also be interested in electrochemical C–N coupling reactions, it is necessary to systematically review the fundamentals, concepts, characteristics, classification, key evaluation indices, quantitative and qualitative analysis of electrochemical C–N coupling reactions, which are presented in this work and will be informative and inspiring for further contributions to this fascinating and rapidly changing area.

In this review, we provide a systematic and critical understanding of the roadmap toward electrochemical C–N coupling reactions using the earth-abundant CO<sub>2</sub> and nitrogenous small molecules (N<sub>2</sub>, NO, NO<sub>2</sub><sup>-</sup>, NO<sub>3</sub><sup>-</sup>, NH<sub>3</sub>, etc.) under environmentally benign conditions. The design and development of the electrocatalysts, theoretical calculations, and reaction mechanisms for the C–N bonding reactions are systematically discussed. Particularly, we focus on the analysis of the key factors influencing the high catalytic activity and selectivity toward specific target products of the catalysts utilized in the electrochemical C–N coupling reaction based on CO<sub>2</sub> and nitrogenous small molecules (N<sub>2</sub>, NO, NO<sub>2</sub><sup>-</sup>, NO<sub>3</sub><sup>-</sup>, NH<sub>3</sub>, etc.). Finally, the research direction and opportunities for designing advanced electrocatalysts and electrolytic reactors, *in situ* characterization techniques for mechanistic understanding and product detection, and the prospects for C–N coupling reactions are proposed.

## 2. Fundamentals of electrosynthesis

Electrochemical C–N coupling reactions, as an important strategy for the efficient construction of organonitrogen compounds, have been widely used in the synthesis of drugs, natural products, ligands, and catalysts. As a new strategy for the electrosynthesis of organonitrogen compounds, the electrochemical C–N coupling reaction is based on the principle of electron gain and loss at the cathode and anode, respectively, to avoid or reduce the use of metal catalysts or quantitative oxidant in conventional methods, making the electrosynthesis system cleaner, greener and more economical. Electrosynthesis, as an emerging redox platform, is superior to traditional synthesis methods, but electrochemical reactions still have a few shortcomings, and thus further improvements are needed to fully realize the potential of electrically driven chemical reactions.

The factors that influence the electrosynthesis performance include the reaction temperature, concentration, and solvent, which need to be considered, similar to the traditional reaction. Additionally, the influence of the current density, electrode potential, electrode material, and electrolyte must be considered in electrosynthesis. The external power supply is usually a direct-current power supply, where constant current or constant potential electrolysis is realized by controlling the current or adding a reference electrode to control the potential of the working electrode. Thus, to better understand the underlying principle of the electrochemical C–N coupling reaction, initially, we introduce some basic concepts, characteristics, classifications, and key evaluation indices of electrosynthesis in this section.

### 2.1 Basic electrosynthesis concepts

As one of the most active and competitive fields in chemistry, electrosynthesis produces chemical compounds in an electrochemical cell under ambient conditions. Thus, by exploiting the cheapest and greenest source of electrons from electricity, electrolysis is an efficient and green approach to performing complex redox reactions under mild conditions. Presently, electrosynthesis is undergoing a resurgence, which will undoubtedly be one of the most efficient methods for activating small molecules. Indeed, a wide range of electrode materials has been exploited for the oxidation and reduction of various reactants for the electrosynthesis of organic and inorganic compounds by electrolysis.

In electrosynthesis, electricity is applied to replace complex redox reagents for the activation and transformation of the reactants.<sup>45,46</sup> Typically, two-electrode electrosynthesis setups are composed of an anode and cathode, which are immersed in an electrolyte solution. The oxidation or reduction reaction can occur by applying a potential difference between the cathode and anode through an external power source. In an electrosynthesis reaction, oxidation and reduction occur simultaneously in the electrolyte at the anode and cathode, respectively, which are driven by a constant current or constant potential technology in an undivided or divided electrocatalytic

reactor.<sup>47,48</sup> The purpose of electrosynthesis is to increase the electrochemical oxidation or reduction reaction rates through catalytic processes occurring at the electrode surface, where chemical bonds break and form as electron and ion transfer occurs. As the availability of renewable electricity increases, electrochemical devices can facilitate electrical-chemical conversion to enable the storage of electrical energy in chemical form or electricity-driven conversion to generate useful chemical compounds. In electrosynthesis devices, the use of highly reactive and/or toxic agents can be completely avoided (direct electrosynthesis) or produced *in situ* on the electrode surface in a controlled manner (mediated electrosynthesis). Efficient electrosynthesis processes are needed to facilitate electrical/chemical interconversions to enable renewable energy technologies and environmentally friendly processes, which are beneficial to realize a sustainable energy infrastructure.

Electrosynthesis occurs at the electrode/electrolyte interface and consists of the following main steps in series:<sup>49</sup> (1) transfer of the reactants from the electrolyte towards the electrode surface; (2) transportation of the reactants on the electrode surface and in the adjacent electrolyte layer *via* surface adsorption or chemical reaction; (3) gain and loss of electrons at the interface between the electrode and the solution; (4) conversion of the reaction product at the electrode surface and in the nearby liquid layer *via* surface desorption or chemical reaction; and (5) transfer of the reaction product(s) from the electrode surface in the electrolyte. The whole electrosynthesis process includes pre-treatment, electrolysis, and post-treatment, among which electrolysis is the most important step. The pre-/post-treatments usually include purification, dehumidification, refining, and separation.

## 2.2 The characteristics of electrosynthesis

The development of electrosynthesis technology has high research significance and commercial value for renewable energy conversion and storage. Compared to ordinary redox reactions, electrosynthesis offers several economic, ecological, and practical advantages.<sup>49–51</sup> The main advantages of electrosynthesis are as follows:

(1) Electrosynthesis does not require toxic or dangerous oxidants and reducing agents. The use of electricity instead of redox reagents reduces waste generation, thereby improving the sustainability and cost-efficiency. Moreover, the electrosynthesis products with fewer by-product(s) are easy to separate and refine with high product purity.

(2) The electrode potential as the driving force for electrochemical reactions powered by green renewable energy can be continuously varied and precisely adjusted to match the redox potential of a specific chemical compound in the electrolyte solution to enhance the selectivity.

(3) Electrosynthesis reactions are usually carried out at ambient temperature and pressure, with relatively mild reaction conditions, leading to low energy consumption, zero-emission, and reduced equipment cost.

(4) For electrosynthesis, different products can be synthesized by regulating the electrode potential for the reaction to be carried out to produce the predetermined targeted product(s) with high yield and selectivity by controlling the electrode potential.

(5) The well-controlled electrochemical reaction process facilitates the mechanistic understanding of the intrinsic relationship between the material structure and the catalytic performance of the catalyst, which are very important for the design and synthesis of high-performance next-generation electrocatalysts.

Alternatively, electrosynthesis technology is limited to oxidation and reduction reactions, leading to the simultaneous formation of oxidation and reduction products on the anode and cathode, respectively. Thus, to ensure the efficient diffusion and separation of the reactants and target products, specifically designed electrode materials, electrolytic cell structures, and diaphragm materials are often required, which greatly increases the complexity of the electrolyzer. Moreover, the existing theories and technologies for electrosynthesis, especially electrochemical reaction kinetics and reactant/product separation, need further improvement.

## 2.3 The electrosynthesis classification

For the classification of electrosynthesis, there are usually two classification methods, as follows:

(1) According to the synthesis method, electrosynthesis can be divided into two categories, *i.e.*, direct electrosynthesis and indirect electrosynthesis. The former is directly completed on the surface of the electrocatalyst, while the latter is carried out by traditional chemical methods, but the oxidant (or reducing agent) is electrochemically regenerated.

(2) According to the types of reactions occurring on the electrocatalyst surface, electrosynthesis reactions can be divided into two categories, *i.e.*, anodic oxidation and cathodic reduction processes. The oxidation reaction involves electron loss or an increase in the oxidation state, which is commonly employed for wastewater treatment.<sup>52</sup> In contrast, the reduction process involves a gain of electrons or decrease in the oxidation state. In the anodic oxidation process, the active sites lose electrons on the anode and the reactants are converted into the corresponding products, where some possible reactions include: (1) the anions lose electrons on the electrode and are converted into products with lower negative charges, such as OH<sup>−</sup> in water electrolysis to precipitate O<sub>2</sub> at the anode, Cl<sup>−</sup> in brine is anodized to generate Cl<sub>2</sub>, and F<sup>−</sup> is anodized to F<sub>2</sub> in oxygen-containing molten salt electrolyte; (2) the cations lose electrons on the electrode and are converted into a product with a higher positive charge; and (3) reaction with a change in oxygen content, such as water electrolysis to produce O<sub>2</sub>.

With the continuous development of electrosynthesis, cathode reduction has also received extensive attention. The main process for cathode reduction is that electrons transfer from the cathode to the discharge species to convert them into products. Usually, the following types of reactions occur: (1) the cation receives electrons on the electrode and is converted

into product(s) with a lower positive charge. For example, in the electrolytic extraction of metals, the metal cation ( $M^+$ ) is deposited on the cathode as metal M. In water electrolysis,  $H^+$  can obtain electrons to produce  $H_2$ ; (2) the anion gains electrons on the electrode to convert it into a product with a higher negative charge; and (3) the reduction of neutral species to form anions, such as  $O_2$  on the cathode can be reduced to  $H_2O_2$  and  $H_2O$  through 2- and 4-electron pathway, respectively.

#### 2.4 The key evaluation index for electrosynthesis

To evaluate and compare the catalytic performance for electrosynthesis, the key parameters that have been used as a gauge for evaluating the performance of an electrocatalyst include the following:

(1) **Overpotential ( $\eta$ ).** Overpotential refers to the additional driving force required to drive a redox reaction at a specific rate. Specifically, the overpotential is the voltage difference between the thermodynamic reduction/oxidation potential and actual electrode reduction/oxidation potential, which can be calculated using the formula  $\eta = E^0 - E_{cat}$ , where  $E^0$  is the standard electrode potential of a certain target product and  $E_{cat}$  is the potential applied to the working electrode. Under the same faradaic efficiency (FE) of a certain product, the smaller the overpotential, the better the catalytic performance of the electrocatalyst. When the current is small, the rate at which the electrode potential changes with the current is related to the limiting rate of charge crossing the phase boundary between the electrode and the electrolyte, which is called the charge transfer overpotential. At a certain overpotential, the charge transfer rate depends on the properties of the reactants, the electrolyte, and the electrode itself. At higher currents, the charge transfer rate is usually no longer the rate-determining step, where the reaction rate is determined by the relatively slow mass transfer rate of reactants from the electrolyte to the electrode or products from the electrode to electrolyte (called diffusion overpotential), or by a slow chemical reaction coupled with a charge transfer step (called reaction overpotential), including the adsorption–desorption process of the reacted species or the chemical reaction that occurs before and after the charge transfer reaction.

(2) **Current density ( $j$ ).** The current density is used to measure the reaction efficiency of electrosynthesis, which is significant for evaluating whether an electrocatalyst or electrochemical reaction meets the requirements for large-scale production. The current density is usually expressed as the total current measured at a specific potential divided by the geometric area of the working electrode (geometric current density,  $j_{geo}$ ,  $mA\ cm^{-2}$ ) or the mass of the loaded catalyst (mass current density,  $j_{cat}$ ,  $mA\ mg^{-1}$ ). The partial current density of a certain product corresponds to the total current density, which represents the current density of a single product among many products, which is also an important indicator for evaluating the electrocatalyst performance and calculating the Tafel slope. The current density depends on the number of active sites in the electrocatalyst, the mass transfer rate of the reaction process, and the impedance of the system (*i.e.*, the resistance

for electrons to be transferred to the reactant from the electrode surface).

(3) **Faradaic efficiency (FE).** The faradaic efficiency is used to express the percentage of electricity consumed to generate the target product in the total electricity consumed by the electrochemical reaction, which reflects the catalytic selectivity of an electrocatalyst for a certain product.<sup>53–56</sup> The formula for its calculation is:  $FE = nzF/Q$ , where  $n$  is the molar amount of the product (mol);  $z$  is the number of electrons transferred to generate the target product molecule;  $F$  is the Faraday constant ( $F = 96\ 485\ C\ mol^{-1}$ ); and  $Q$  is the amount of charge consumed by the entire electrochemical reaction.

(4) **Tafel slope.** The Tafel slope is used to express the relationship between the overpotential and the logarithm of the current density, which is used to characterize the reaction rate and is closely related to the intrinsic properties of the electrocatalyst.<sup>57–60</sup> The Tafel slope is given by the partial derivative of the overpotential with respect to the log of the current density as follows:  $\eta = a + b \times \log(j)$ , where  $a$  is a constant usually associated with the structure of the electrolyte and the electrode surface,  $b$  is the Tafel slope,  $\eta$  is the overpotential and  $j$  is the partial current density of the target product. According to this formula, it can be seen that the  $a$  and  $b$  values can be obtained from the linear part of the Tafel plot, where the  $a$  value is the intercept of the  $y$ -axis and the  $b$  value is the slope of the linear region of the Tafel plot. The Tafel slope represents the potential difference required to increase or decrease the current density by a factor of 10. A smaller  $b$  indicates that less  $\eta$  is required to deliver the same current density increment, indicating a faster electron transport rate. A high-performance electrocatalyst should have a small  $b$  value. The Tafel slope can be applied to analyze the electrochemical reaction mechanism and kinetics.<sup>61–64</sup> For example, it can be employed to infer the rate-determining step (RDS) and judge the mechanism of the reaction according to the magnitude of its slope. Specifically, a slope of  $-120\ mV\ dec^{-1}$  implies that the RDS for the ECRR is the initial step of  $CO_2^{*-}$  generation, whereas the RDS is the chemical step following the fast one-electron pre-equilibrium when the Tafel slope is  $-60\ mV\ dec^{-1}$ .<sup>59,65</sup>

(5) **Yield rate.** The yield of electrosynthesis is expressed both in terms of chemical yield and current efficiency. The current efficiency is the ratio of Coulombs consumed in forming the products to the total number of Coulombs passed through the cell. Side reactions decrease the current efficiency. The yield rate is a measure of the reaction rate for the formation rate of target products. The yield rate for a certain product can be calculated using the following equation:

$$r = (C \times V)/(t \times A)$$

where  $C$  is the measured concentration of the product,  $V$  is the volume of the electrolyte,  $t$  is the reduction reaction time, and  $A$  is the geometric area, electrochemical-specific surface area, the weight of the catalyst, or the amount of active atoms.

(6) **Turnover frequency (TOF).** In electrosynthesis, the same metal nanoparticles are often loaded on supports with

different specific surface areas. Consequently, their specific activities are different. However, although the catalytic activity of identical metal nanoparticles is initially the same, this is not reflected in their specific activity. Thus, the specific activity cannot reflect the real catalytic activity of the catalyst, which is mainly due to the specific activity being greatly influenced by the specific surface area of the support, the mass transfer, and the diffusion of the substrate. To exclude these effects, Michel Boudart first proposed in 1968 the TOF to evaluate the catalytic rate of a catalyst, that is, the number of molecules that undergo reaction per second per active site.

Recently, TOF has been redefined as the total number of molecules converted to the desired product per catalytically active site per unit time,<sup>66,67</sup> which is expressed as  $\text{TOF} = (j_{\text{product}}/NF)/(m_{\text{cat}}w/M)$ , where  $j_{\text{product}}$  is the partial current for a certain product (A),  $N$  is the number of electrons transferred for product formation,  $m_{\text{cat}}$  is the catalyst mass in the electrode (g),  $w$  is the metal loading in the catalyst,  $M$  is the atomic weight of the metal ( $\text{g mol}^{-1}$ ), and  $F$  is the Faraday constant ( $96\,485 \text{ C mol}^{-1}$ ).<sup>68–71</sup> Therefore, the TOF calculation largely depends on determining the number of active sites. It can be assessed by various methods, including copper underpotential deposition,<sup>72</sup> counting the number of molecules on the exposed surfaces of the catalyst,<sup>73,74</sup> and cyclic voltammetry quantitative tests.<sup>75,76</sup> However, for most solid-state catalysts, especially some emerging complex catalysts, it is not easy to obtain the TOF value precisely because not all surface atoms in the catalyst are catalytically active or equally available. Nevertheless, although the calculated TOF is relatively imprecise at the current stage, it still provides a useful way to compare the intrinsic catalytic activity among various catalysts.

(7) **Stability.** The stability of an electrocatalyst is an important parameter to evaluate its potential practical application. Generally, two methods are used for stability measurements, *i.e.*, cyclic voltammetry (CV) or linear sweep voltammetry (LSV), and electrolysis with a constant current or constant potential. The CV and LSV methods are used to compare the changes in the overpotential before and after a certain cycle test by performing CV or LSV in a certain potential range. After certain repeated cycles, the smaller the change in the potential, the higher the stability of the electrocatalyst. The constant current or potential method monitors the potential or current density change as a function of the reaction time at a constant current density or potential. With an increase in the reaction time, the longer the duration with no potential or current density change, the better the electrocatalytic stability.

### 3. Electrocatalytic reactor

The electrochemical C–N coupling reaction is carried out in an electrocatalytic reactor driven by an electrochemical workstation with a two-/three-electrode system, which is different from the equipment used in traditional chemical reactions. The effect of the reactor on the electrochemical performances of the C–N coupling reaction is crucial, where its design and

development mainly involve fluid mechanics, structural mechanics, chemical mass transfer, and electrical engineering. Overall, in electrochemical C–N coupling reaction systems, more research efforts are focused on the design of catalysts rather than engineering innovations in the electrocatalytic reactor. Therefore, the development of an electrocatalytic reactor is a relatively slow process.

In general, an electrolytic reactor is an electrochemical cell that utilizes an external source of electrical energy to drive a non-spontaneous redox reaction. Typically, an electrolytic reactor is composed of three components, including a cathode, anode, and electrolyte. When an external voltage is applied to the electrodes, the ions in the electrolyte will be driven to the electrode with the opposite charge. The commonly used three-electrode electrolytic cell consists of a working electrode, counter electrode, and reference electrode, forming one circuit between the working and reference electrodes for the electrochemical reaction process on the working electrode and another circuit between the working and counter electrodes to transmit electrons from the former to the latter for reaction on the counter electrode. In short, a closed loop circuit is created between the counter electrode and the working electrode, and the potential of the working electrode is related to the reference electrode. A typical three-electrode system consists of a measurement circuit (constituted by the working electrode and the reference electrode) and a polarization circuit (constituted by the working electrode and the counter electrode).

The design of electrochemical reactors is an important strategy for any type of efficient and practical electrosynthesis. Various reactor designs have been developed for electrosynthesis.<sup>24</sup> Currently, there are three typical types of electrosynthesis reactors, including H-type cells, flow cells, and membrane electrode assembly (MEA) cells, which can be adapted for electrochemical C–N coupling reactions (vide infra). In this section, we briefly describe the setup of these three types of reactors and the associated experimental procedures for electrosynthesis. Furthermore, the advantages and disadvantages of each of the reactors will be discussed.

#### 3.1 H-Type cell

The representative H-type cell is composed of a cathode compartment for the reduction reaction and an anode compartment for the oxidation reaction, which is the most widely used cell. Typically, the cathode chamber and the anode chamber are separated by a proton/ion-exchange membrane (Fig. 2) to enable ionic conductivity but prevent the crossover of gaseous and aqueous products.<sup>77</sup> However, the H-type cell has two major drawbacks. Firstly, the gas mass transfer in the H-type cell is not substantial due, for example, to the extremely low solubility of  $\text{CO}_2$  in the electrolyte, thus resulting in slow ECRR reaction kinetics.<sup>78</sup> Secondly, H-type cells can only use neutral electrolytes for the ECRR, while alkaline electrolytes cannot be used given that  $\text{CO}_2$  can react with hydroxide ions to form carbonates, while acidic electrolytes can cause severe hydrogen evolution reaction (HER) from water splitting.<sup>79,80</sup> Despite the

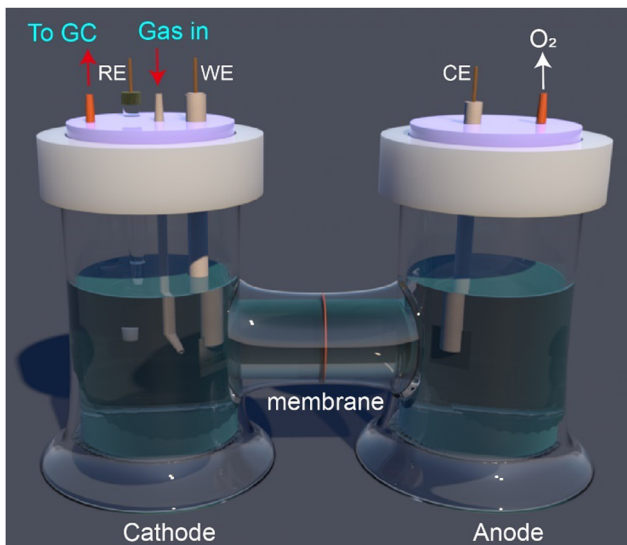


Fig. 2 Schematic illustration of an H-type cell with a typical three-electrode system. (WE: working electrode, CE: counter electrode, and RE: reference electrode).

slow reaction kinetics and high energy consumption associated with the H-type cell, it has significantly contributed to the early research on ECRR and other electrolysis reactions. For the C–N coupling reaction in an H-type cell, a mixture of CO<sub>2</sub> and N<sub>2</sub> gas is continuously purged in the catholyte, and the dissolved CO<sub>2</sub> and N<sub>2</sub> molecules are adsorbed on the electrocatalyst surface and undergo subsequent reduction for C–N coupling. Thus, a flow cell is required.

### 3.2 Flow cell

In comparison to the conventional H-type cell, the flow cell (Fig. 3), which is composed of a gaseous cathode compartment, a catholyte cathode compartment, and an anode compartment,<sup>81–84</sup> enables the ECRR to operate at much higher current densities by mitigating the mass-transport limitation.<sup>85</sup> Typically, the catholyte and anolyte compartments are separated by a proton/ion exchange membrane. The working electrode, membrane, and counter electrode are positioned and clamped together using a polytetrafluoroethylene spacer, enabling the catholyte and anolyte to be pumped to the cathode and anode chamber, respectively, which are separated by a membrane.<sup>78,86</sup>

CO<sub>2</sub> and N<sub>2</sub> flow through the gas flow channel at the back side of the gas diffusion layer to diffuse to the catholyte on the catalyst. A port is drilled in the polytetrafluoroethylene spacer, enabling the reference electrode to be positioned at a predetermined distance from the working electrode. The electrolyte is circulated through the electrochemical cell with a certain flow rate controlled by a peristaltic pump.

In a flow cell, the gas diffusion electrode (GDE) plays a crucial role, which serves as the place for the electrochemical reactions in the triple-phase boundary. A gas diffusion layer (GDL) is used to support the catalytic layer, transfer reaction gases and products, and conduct electrical current.<sup>87,88</sup> The

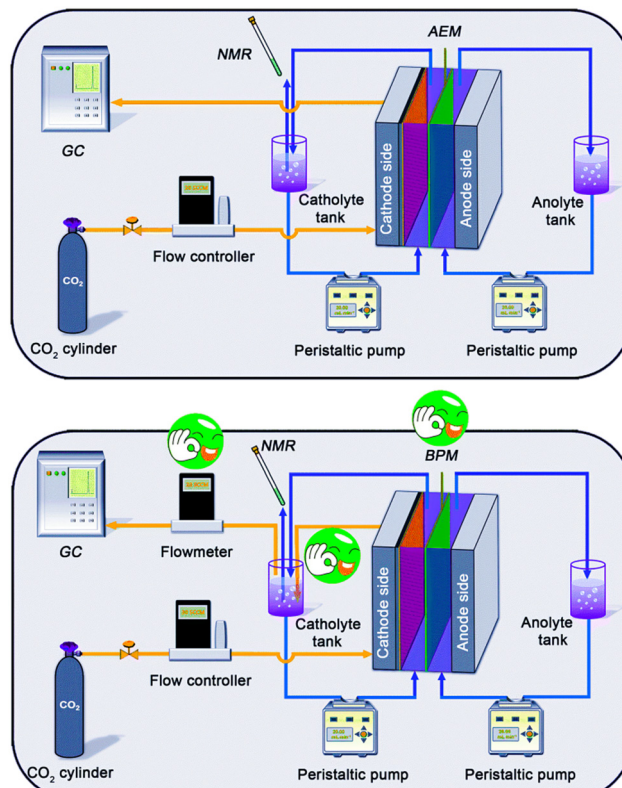


Fig. 3 Schematic comparison of the conventional (a) and modified (b) flow cell measurement systems. Reproduced with permission from ref. 85 Copyright 2021, The Royal Society of Chemistry.

substrate is usually a porous conductive material (such as carbon paper and carbon cloth), and is hydrophobized with polytetrafluoroethylene (PTFE) to facilitate the formation of gas channels. The GDL is located between the catalytic layer and the flow field/polar plate and plays a role in regulating the water and gas redistribution. Although the GDL does not directly participate in electrochemical reactions, it plays an important role in improving the electrode performance. An ideal GDL needs to have good electrical conductivity, high structural porosity, appropriate hydrophilic/hydrophobic balance, long-term chemical and thermal stability, and low cost.

Fig. 3a shows a typical flow electrochemical cell for the ECRR, together with the qualitative and quantitative product analysis units (*i.e.*, nuclear magnetic resonance, NMR, and gas chromatography (GC)), peristaltic pump, and mass flowmeter (Fig. 3a).<sup>85</sup> For a modified flow cell (Fig. 3b), the outlet gas in the system is first scrubbed by the catholyte, which is further mixed with potential gas products from the catholyte chamber, and then flows to the online GC for quantification analysis through a mass flowmeter. Consequently, the liquid products that evaporated into the outlet gas, as well as that dissolved in the catholyte can be collected and analyzed, respectively. The modified measurement protocol also enables the gas products to be fully collected and accurately assessed. For electrolyte crossing, a bipolar membrane (BPM) can be used instead of a

traditional anion exchange membrane (AEM), which suppresses electromigration and electroosmotic resistance.

Compared with the conventional H-type cell, the significant difference in the flow cell is the GDE configuration, which allows the coexistence of the gas, liquid, and solid phases by exposing one side to the feeding gas and the other side to the electrolyte.<sup>89–93</sup> However, the flow cell also has some drawbacks, as follows:<sup>24</sup> (1) relatively high resistance due to the existence of two compartments; (2) GDE flooding, carbonate formation, and crossover issues; and (3) cost disadvantages due to the use of a large amount of electrolytes, especially alkaline electrolytes. These disadvantages lead to significant uncertainty for the industrial production of flow cells.

### 3.3 MEA cell

The MEA, also known as “fuel cell-type”, “zero-gap”, “catholyte-free”, or “gas-phase electrolysis”, is the core component of a fuel cell and plays a decisive role in its catalytic performance, which consists of a proton/ion exchange membrane, catalyst layers, and GDLs.<sup>94,95</sup> The catalysts on each side of the MEA enable reactions and the middle membrane allows the passage of protons, while keeping the gases separate. Unlike the H-type cell and flow cell, the MEA cell is a two-electrode system. In the MEA cell, no catholyte electrolyte is needed for the cathode side and water is provided by the vapor phase or diffusion from the anolyte electrolyte.

The GDL is a key component in MEAs, which usually uses PTFE or proton conductors as a binder. The PTFE binder is prepared on the GDL after mixing the catalyst with a certain amount of PTFE by scraping, spraying, or rolling method. After calcination, the surfactant can be removed to ensure PTFE shows binding and hydrophobic effects. To complete the three-dimensional electrode architecture and form the GDE, a layer of low-concentration proton conductor solution is sprayed on the surface of the catalytic layer. Finally, the electrode and the proton exchange membrane (PEM) are hot-pressed to form the MEA. In the case of the proton conductor binder, the proton conductors (*e.g.* Nafion and perfluorosulfonic acid) contain both hydrophobic (C–F main chain) and hydrophilic groups ( $-\text{SO}_3^-$ ). When some of the sulfonic acid groups of Nafion are lost by thermal decomposition, it will exhibit hydrophobic properties, while the remaining sulfonic acid groups are hydrophilic, thus forming a uniformly distributed hydrophilic and hydrophobic interpenetrated network in three-dimensional space. A typical preparation method is as follows:<sup>96</sup> firstly, the catalyst is uniformly mixed with a certain amount of Nafion solution, and then coated on the GDL. Thereafter, it is calcined above 280 °C under the protection of inert gas, where some of the Nafion in the catalytic layer loses its sulfonic acid groups to act as a hydrophobic material in the electrode, similar to PTFE in the PTFE-bonded electrode. Therefore, the catalytic layer of the electrode not only ensures the sufficient contact of the catalytically active components with the proton conductors and electronic conductors but also provides sufficient gas and water channels to expand the three-dimensional reaction area of the cell, thereby improving the performance of the whole cell.

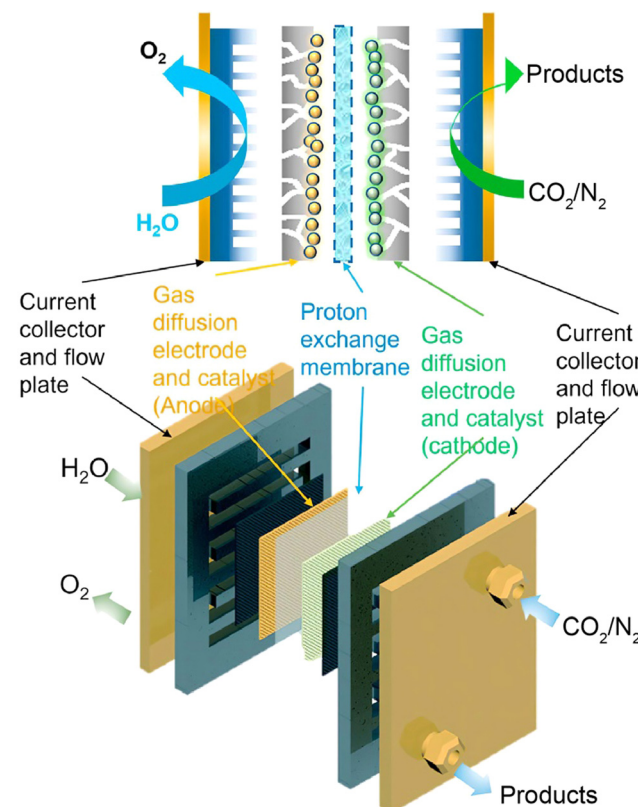


Fig. 4 Schematic of MEA cell for  $\text{CO}_2$  and  $\text{N}_2$  electrocatalysis. Reproduced with permission from ref. 102. Copyright 2022, Elsevier.

Recently, MEA cells have become an attractive design for various electrochemical reduction reactions due to their low ohmic loss and high energy efficiency.<sup>97–99</sup> Numerous reports have demonstrated the feasibility of MEA-like cells for  $\text{CO}_2$  reduction with current densities of up to 100  $\text{mA cm}^{-2}$ , an order of magnitude higher than that achieved using typical aqueous architectures.<sup>100,101</sup> In general, a proton exchange membrane is commonly applied as an electrolyte in MEA cells, and gaseous reactants can be fed directly and there is no aqueous electrolyte between the electrodes.<sup>102</sup> MEA cells do not have a mainstream cathode electrolyte, but an electrolyte is required at the interface between the catalyst and the membrane to allow ion transport across the ion-exchange membrane. As shown in Fig. 4, the main advantageous structure of MEA cells is that GDE and ion exchange membrane are attached as a solid catholyte, in which the gas/liquid products are collected at the feed side, and the flow between the catalyst layer and ion exchange membrane can be eliminated by the catholyte. Therefore, this membrane-based fabrication technique can greatly reduce the ohmic resistance during the reaction, thereby increasing the current density.<sup>97</sup>

Overall, the development of electrocatalytic reactors is crucial for electrosynthesis, which can lead to a switch from laboratory-scale processes to industrial-scale production. For electrochemical C–N bond formation from carbon and nitrogen sources, the MEA cell is an ideal choice, which can enable  $\text{CO}_2$

electrolysis to work at conditions relevant to the industrial electrolyzer. In this case, an ideal electrocatalytic reactor should not only efficiently facilitate electron transfer, ion transport, and controllable gas diffusion, but also prevent the mixing of the anolyte and catholyte. Electrochemical C–N coupling reactions have been performed under various reaction conditions, such as coupling at the cathode, generating intermediates at the cathode and anode, and through redox mediators. Based on the coupling method and the nature of the substrate, an electrosynthesis reactor can be specifically designed. The appropriate design of an electrosynthesis electrolyzer is crucial for achieving a high energy efficiency toward C–N coupling.

## 4. Quantitative and qualitative analysis

To properly evaluate the catalytic performances of electrosynthesis, some precise methods for the analysis of the products generated in the experiments are crucial, which must be extremely sensitive, reliable, precise, and reproducible. This is because many factors affect the accurate determination of the product, such as quantitative time and pH value of the solution, cleaning agent (such as methanol and propanol). In the electrocatalytic C–N coupling reaction system, both gas-phase products and liquid-phase products are generated, which will be discussed here.

### 4.1 Gas-phase products

Regarding gas-phase products, generally gas chromatography (GC) is applied for their quantitative and qualitative analysis. A GC is made of a narrow tube, known as the column, carrying a continuous flow of inert or nonreactive gas. GC is an experimental technique for separating a mixture into its components and is commonly used in the qualitative and quantitative determination of sample components. GC is a time-based separation technique, in which the components of a sample pass through the column at different rates depending on their chemical and physical properties and the resulting relationship with the column lining or packing (called stationary phase) interaction. The column is usually enclosed in a temperature-controlled oven. As chemicals exit the column, they are electronically detected and identified. The time at which the peak appears is called the retention time, which can be used to characterize each component, and the size of the peak (peak height or peak area) is a measure of the content of the component.

Commonly, a flame ionization detector (FID) and thermal conductivity detector (TCD) are applied for the detection of the gas products in the ECRR system. The FID is primarily sensitive to hydrocarbons and is more sensitive than the TCD. However, the FID cannot detect H<sub>2</sub>O or CO<sub>2</sub>, making it ideal for the analysis of environmental organic analytes. The TCD is a concentration-type detector, which responds to the difference in thermal conductivity between the measured component and the carrier gas. The TCD relies on the thermal conductivity of the substance when an electric current is passed through a thin

wire of tungsten–rhenium. In this setup, helium (He) or N<sub>2</sub> is used as the carrier gas because of their relatively high thermal conductivity, which keeps the filament cool and maintains a uniform resistivity and electrical efficiency in the filament. As analyte molecules elute from the column and mix with the carrier gas, the thermal conductivity decreases, while the filament temperature and resistivity increase, thus causing voltage fluctuations, which eventually cause the detector to respond. The detector sensitivity is directly proportional to the filament current and inversely proportional to the immediate ambient temperature of the detector and the carrier gas flow.

The FID is a typical destructive and mass detector, which is powered by a flame, which is generated by the combustion of hydrogen and air. When organic compounds enter the flame from hydrogen and oxygen combustion, chemical ionization occurs at high temperatures, and the ionization generation is several times higher than the base flow. An order of magnitude of ions, under the directional action of the high-voltage electric field, forms an ion flow, and the weak ion flow (10<sup>-12</sup>–10<sup>-8</sup> A) is amplified by high resistance (10<sup>6</sup>–10<sup>11</sup> Ω) and becomes proportional to the amount of organic compounds entering the flame. The increase in the current is converted to a peak in the chromatogram, and thus the organic matter can be quantitatively analyzed according to the magnitude of the signal. The FID-compatible carrier gases include helium, hydrogen, nitrogen, and argon. In an FID, sometimes the flow path is modified before entering the detector. A mechanized system converts CO and CO<sub>2</sub> into CH<sub>4</sub> for detection. A different technology is the Polyarc, developed by Activated Research Inc., which converts all compounds to methane.

### 4.2 Liquid-phase products

The quantitative and qualitative analysis of the liquid-phase products in the electrochemical C–N reaction system is not as straightforward as other common gases such as N<sub>2</sub>, O<sub>2</sub>, H<sub>2</sub>, and CO, which are practically insoluble in water, and thus can be easily quantified using GC. Typical, NH<sub>3</sub> is a polar small molecule, which is highly soluble in water (482 g L<sup>-1</sup> at 24 °C).<sup>103</sup> Therefore, the quantitative determination of NH<sub>3</sub> is usually carried out in aqueous solution. In a typical experiment, a solution is used to absorb NH<sub>3</sub> and the concentration of NH<sub>3</sub> in the solution is determined using various techniques. However, the actual measurement is greatly affected by the NH<sub>3</sub> in the background of the test system and the non-electrochemical effect on NH<sub>3</sub> synthesis, which can be determined by a set of control experiments. At present, the relatively mature methods for the quantitative and qualitative analysis of NH<sub>3</sub> include ion chromatography, spectrophotometry, ion selective electrode method, and nuclear magnetic resonance (NMR) spectroscopy.

Spectrophotometry, also known as colorimetry, is widely used in the detection of NH<sub>3</sub> due to its high precision and low price. The methods to measure NH<sub>3</sub> can be subdivided into three categories, *i.e.*, the indoxyl blue method, salicylic acid method, and Nessler reagent method.<sup>104</sup> The indoxyl blue method is based on the Berthelot reaction to detect NH<sub>3</sub>, with the detectable concentration of 0–0.6 mg L<sup>-1</sup> because

phenol/salicylic acid and hypochlorite in alkaline solution will produce a blue indoxyl product. Sodium nitroprusside and potassium ferrocyanide are both used as catalysts to speed up the reaction, and citrate prevents the precipitation of ions that may form during the alkaline reaction. Salicylic acid is used instead of phenol to avoid the formation of hazardous *o*-chlorophenol during the reaction. The concentration of NH<sub>3</sub> can be detected by measuring the absorbance of indoxyl between 630–650 nm by ultraviolet spectroscopy. Typically, 2 mL of the diluted electrolyte is taken from the electrochemical reaction vessel for determination. Afterward, 2 mL 1.0 M NaOH solution containing 5 wt% salicylic acid and 5 wt% sodium citrate is added. Subsequently, 1 mL of 0.05 M NaClO and 0.2 mL of an aqueous solution of 1 wt% C<sub>5</sub>FeN<sub>6</sub>Na<sub>2</sub>O (sodium nitroferricyanide) are added. After standing for 2 h at room temperature, the absorption spectrum is measured using a UV-vis spectrophotometer. The formation of indophenol blue is determined using the absorbance at a wavelength of 655 nm. The concentration-absorbance curves are calibrated using standard ammonia chloride solutions, which contain the same concentration of electrolyte as that used in the electrolysis experiments.<sup>105,106</sup> Although this method is precise and reliable, it has some disadvantages due to its time-consuming and laborious procedures. The Nessler reagent process involves the use of potassium hydroxide and potassium tetraiodomercurate. Mercury and iodide react with NH<sub>3</sub> to form a reddish-brown compound, which can be detected by UV spectroscopy at an absorbance of 420 nm. It is worth noting the following: (1) nessler reagent contains the highly toxic mercury; therefore, care must be taken during the detection process; (2) nessler reagent has a short life; therefore, it should be used within three weeks; and (3) for accurate results, it is recommended to detect NH<sub>3</sub> with Nessler reagent within 10–30 min to avoid any unreliable output.

#### 4.3 Isotope labeling experiments

Isotope labeling experiments should be performed to further validate the origin of the products and deduce the plausible reaction pathways in the electrochemical C–N coupling reaction, especially for N-containing catalysts or the use of nitrogen-containing raw materials. Normally, the detected amount of organonitrogen compounds should agree well with that detected by another method. The feed carbon and nitrogen sources should only contain <sup>15</sup>N and <sup>13</sup>C, and therefore can be determined using different methods such as infrared spectroscopy (IR), mass spectroscopy (MS), and NMR spectroscopy to distinguish <sup>15</sup>N and <sup>13</sup>C from the possible contaminants <sup>14</sup>N and <sup>12</sup>C.

<sup>1</sup>H NMR is widely used because it is a very convenient method. Given that the chemical shifts between <sup>14</sup>N and <sup>15</sup>N are different, <sup>1</sup>H NMR can distinguish isotopes very well.<sup>107–109</sup> According to <sup>14</sup>N in <sup>14</sup>NH<sub>4</sub><sup>+</sup>, the scalar interaction between <sup>1</sup>H and <sup>14</sup>N in <sup>15</sup>N shows two symmetric signals separated by 53 Hz. In contrast, in <sup>15</sup>N, the <sup>1</sup>H resonance interacting with <sup>15</sup>N in <sup>15</sup>NH<sub>4</sub><sup>+</sup> is divided into three symmetric signals separated by 73 Hz.<sup>108–110</sup> Additionally, by using <sup>13</sup>CO<sub>2</sub> as the feed gas, a

doublet (188 Hz) appears at 8.63 and 8.16 ppm, suggesting the yield of H<sup>13</sup>COOH, compared to a singlet at 8.40 ppm originating from H<sup>12</sup>COOH when using <sup>12</sup>CO<sub>2</sub> as the feed gas.<sup>111</sup> These results indicate that the reaction products evolve from CO<sub>2</sub> reduction. The CO generated during the reaction can be confirmed to originate from CO<sub>2</sub> by GC with mass spectrometer (GC-MS) measurements.

It is worth noting that the labeled products should be of high purity to avoid any other contamination during the reaction. Therefore, additional purification of the feed gas is essential to avoid the presence of other carbon and nitrogen species.<sup>112,113</sup> In conclusion, the results obtained through a series of strictly controlled experiments are convincing.

## 5. Electrocatalytic C–N coupling reaction

Currently, it is still a big challenge to electrochemically convert CO<sub>2</sub> and nitrogenous small molecules (N<sub>2</sub>, NO, NO<sub>2</sub><sup>−</sup>, NO<sub>3</sub><sup>−</sup>, NH<sub>3</sub>, etc.) into the target products *via* ECRR or ENRR with high selectivity and high yield rate, while it is more difficult to simultaneously drive these two electrochemical reduction reactions (ECRR/ENRR) to selectively form C–N-coupled products in the same electrochemical system. The bottleneck of this technique is the competitive nature of the C–N coupling reaction with the individual reduction reaction of CO<sub>2</sub> and nitrogenous small molecules (N<sub>2</sub>, NO, NO<sub>2</sub><sup>−</sup>, NO<sub>3</sub><sup>−</sup>, NH<sub>3</sub>, etc.), together with the competing hydrogen evolution reaction. Therefore, to better explore the C–N coupling reaction, we first provide a systematic understanding of the ECRR and ENRR.

### 5.1 Electrocatalytic CO<sub>2</sub> reduction reaction

CO<sub>2</sub> is a typical triatomic molecule with linear symmetry, in which the two sp hybrid orbitals of the C atom and the 2p<sub>x</sub> orbitals of two O atoms (assuming that the CO<sub>2</sub> molecule is placed along the x-axis) form two σ bonds in a head-to-head format.<sup>114</sup> Meanwhile, the C atom has two 2p orbitals that are not involved in hybridization, which are located on the y-axis and z-axis, namely, 2p<sub>y</sub> and 2p<sub>z</sub> orbitals. They overlap side-by-side with the 2p orbitals of the O atoms on both sides, respectively, forming two stable three-center four-electron p–p delocalized large π bonds (*i.e.*,  $\pi_3^4$ ) which is a non-bonding orbital, and its electron cloud is mainly bound to two O atoms. The O atom is very electronegative, and thus the reactivity of the electrons on the two highest occupied molecular orbitals is relatively poor. The C atom is an electron-deficient center, which can act as an electrophile body and react with nucleophiles and electron-bearing groups. Accordingly, it is known that an effective way to achieve CO<sub>2</sub> activation is to input electrons electro-/photo-chemically or capture electrons from other molecules during the reaction process and use them as a reductant. At present, the CO<sub>2</sub> conversion technologies mainly include chemical reduction, photocatalytic conversion, photoelectric catalytic conversion, and electrochemical conversion.<sup>115–117</sup>

Among the various conversion strategies, the electrocatalytic reduction of CO<sub>2</sub> into high-value-added products has the dual promise of neutralizing carbon emissions and providing a long-term pathway to create energy-dense chemicals and fuels from atmospheric CO<sub>2</sub>. Since the first report of ECRR on metal electrodes in the 19th century, its potential for reducing the global greenhouse effect has been investigated. With substantial endeavors in developing efficient materials (*e.g.*, nanostructured catalysts and electrodes) and technologies for the reduction of CO<sub>2</sub> emission in the past decade, research on ECRR for emission abatement and fuel production has been extensively reported, together with the development of various renewable energy technologies (*e.g.*, solar, wind, and hydro-power). Theoretical predictions also indicated that ECRR by a non-renewable energy source can reduce the emission of carbon and produce high value-added chemicals.<sup>14,15,118</sup> Despite the important value in sustainable energy utilization and environment protection, the large-scale deployment of the ECRR for practical applications is still limited to date by its generally low efficiency and suboptimal selectivity.

As mentioned above, the CO<sub>2</sub> molecule possesses linear central symmetry with two carbon–oxygen double bonds (C=O) with a bond length of 116.3 pm. The energy required to dissolve the C=O bond in CO<sub>2</sub> (800 kJ mol<sup>-1</sup>) is significantly higher than that for most carbonyl groups due to the fact that the bond length of C=O is much shorter than that of the C–O bond and most multiple-bonded functional groups. Because of this, CO<sub>2</sub> has a significant energy difference between its highest occupied and lowest empty molecular orbitals, making it chemically inert. The innate stability of CO<sub>2</sub> molecules makes it difficult to activate them for participation in chemical processes unless they are subjected to extreme circumstances.

The electrolyte used in the ECRR system is usually low-cost inorganic salt solutions (*e.g.*, KHCO<sub>3</sub>, NaHCO<sub>3</sub>, and Na<sub>2</sub>SO<sub>4</sub>), which can donate activated protons to break the C=O bond. Besides, the electrodes can readily be scaled up or miniaturized, which are also feasible for being assembled with the energy or gas reactant input for mass production. However, the rational design and realization of highly efficient, selective, stable, and low-cost ECRR electrocatalysts remain a major challenge. As described above for electrosynthesis, the ECRR is performed using the typical three-electrode cell, including a working electrode loaded with the ECRR catalyst (cathode), a reference electrode to determine the applied potential, and a counter electrode to balance the charge and ion flow during the reaction (anode).<sup>80,120–124</sup>

In the ECRR system, the CO<sub>2</sub> molecules adsorbed on the surface of the catalyst will change their molecular configuration, which can reduce their activation energy. Usually, CO<sub>2</sub> molecules can adsorb on the catalyst surface in several different ways (Fig. 5a)<sup>119,125–127</sup> and will undergo different changes under different potentials. The electrode potential for different paths of CO<sub>2</sub> transformation is summarized in Table 1. Although the theoretical electrode potential of various products presented in Table 1 is not very negative, the applied reduction potential will be much greater than the

theoretical value because the electrode potential required for the activation of CO<sub>2</sub> molecules into \*CO<sub>2</sub> intermediates is very negative.

The ECRR is a multi-proton coupled multi-electron transfer process. A typical ECRR catalytic process is usually divided into three steps, as follows:<sup>20,128</sup> (1) chemisorption of CO<sub>2</sub> molecule on the catalyst surface; (2) dissociation of C=O bonds and/or generation of C–H and C–O bonds by transfer of electrons and protons; and (3) rearrangement of product species, followed by desorption from the electrode surface and diffusion into the electrolyte. In most heterogeneous ECRR processes, these steps occur at the interface of the solid electrocatalyst and CO<sub>2</sub>-containing electrolyte (H-type cell) or the three-phase interface of CO<sub>2</sub> (gas), electrolyte (liquid), and electrocatalyst (solid) (flow cell). Generally, electrodes/catalysts that have higher reactivity with CO<sub>2</sub> than that with competitive H<sub>2</sub> are preferred to suppress the electrochemical hydrogen evolution reaction. At the thermodynamic level, transferring the first electron to a CO<sub>2</sub> molecule requires large reorganizational energy to activate the CO<sub>2</sub> molecule,<sup>129–132</sup> during which the original linear structure of CO<sub>2</sub> is rearranged to a bent radical anion, forming the key intermediate (CO<sub>2</sub><sup>\*</sup><sup>-</sup>) for the ECRR.<sup>133</sup> The subsequent multi-proton-coupled electron transfer processes proceed faster given that they are thermodynamically more advantageous than the first activation phase (Fig. 5b). Nevertheless, the product selectivity will become the primary problem of the ECRR due to the high activity of CO<sub>2</sub><sup>\*</sup><sup>-</sup> and the small potential differences among the various potential reduction products, which highly depend on the specific activity of various catalyst surfaces and active sites. In addition, product selectivity can be further altered, especially when kinetic features are also considered. Typically, the rate of hydrogenation of low-carbon intermediates is faster than the rate of C–C bond formation, resulting in catalytic selectivity for C<sub>1</sub> over C<sub>2+</sub> products.

The direct reduction of CO<sub>2</sub> involves one-electron transfer to the CO<sub>2</sub><sup>\*</sup><sup>-</sup> intermediate. However, this step is highly unfavorable because it has a large formal redox potential of -1.97 V *versus* the standard hydrogen electrode (*vs.* SHE) in an aprotic solvent (*N,N'*-dimethylformamide, DMF) and -1.90 V in water (pH = 7). Thus, electrocatalytic strategies have been developed to bypass the formation of the CO<sub>2</sub><sup>\*</sup><sup>-</sup> intermediate through proton-assisted multiple-electron transfer to reduce CO<sub>2</sub> at lower energetic costs. Depending on the number of electrons and protons transferred, CO<sub>2</sub> can be reduced to different products *via* the ECRR (Table 1), including C<sub>1</sub> (CO, HCOOH, HCHO, CH<sub>4</sub>, and CH<sub>3</sub>OH), C<sub>2</sub> (C<sub>2</sub>H<sub>4</sub>, CH<sub>3</sub>CHO, and C<sub>2</sub>H<sub>5</sub>OH, and C<sub>2</sub>H<sub>6</sub>), and C<sub>3</sub> (C<sub>3</sub>H<sub>7</sub>OH). In contrast, the competing proton reduction *via* the hydrogen evolution reaction is a two-electron process.<sup>133,134</sup> Depending on the binding energies between different metals and the key intermediates involved in the ECRR process, different catalysts show distinct properties and performances for the ECRR. In aqueous solution, \*H, \*OCHO, \*COOH, and \*CO are common intermediates in the ECRR process, and the binding energy difference between these intermediates and the surface of the metal material can induce a completely different reaction path.<sup>135,136</sup>

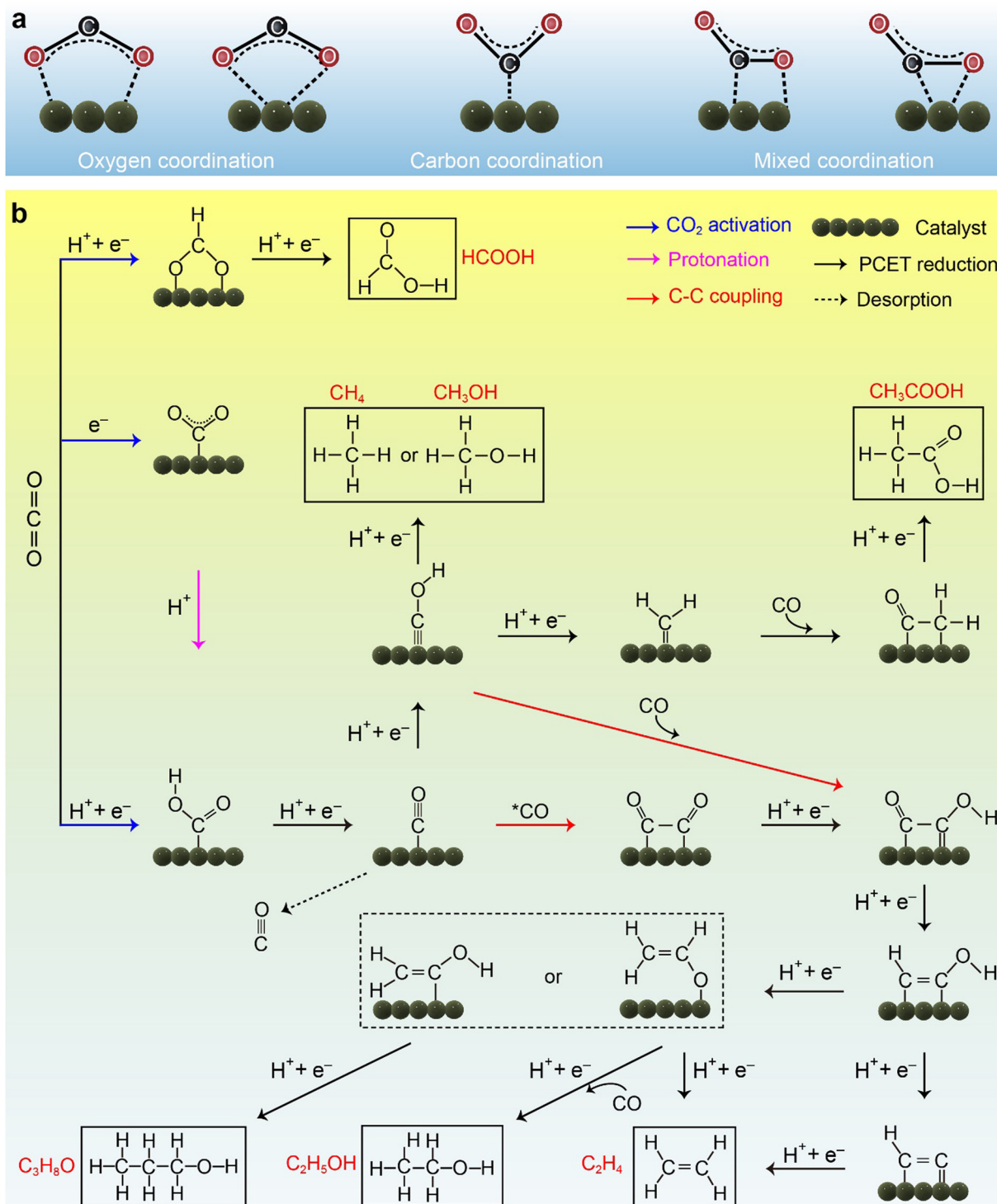


Fig. 5 (a) Schematic illustration of the different types of  $\text{CO}_2$  molecule adsorption modes. Reproduced with permission from ref. 119. Copyright 2016, The Royal Society of Chemistry. (b) Proposed mechanisms for  $\text{CO}_2$  activation, C-C bond formation and elemental reaction pathways to various products during the ECRR. Reproduced with permission from ref. 25 Copyright 2022, John Wiley & Sons, Inc.

Although ECRR technology has promising prospects in solving the energy and environmental problems, it still faces several key challenges. Firstly, the large bond energy of  $\text{C}=\text{O}$  with a stable linear structure will lead to a high overpotential

for the activation of  $\text{CO}_2$  molecules. Secondly, in aqueous electrolytes, hydrogen evolution usually occurs easier than the ECRR due to its low reaction overpotential and simple kinetic process. Given that the ECRR process involves multiple

**Table 1** The equilibrium potentials for electrochemical reduction of CO<sub>2</sub> (25 °C), 1 atmosphere of gases, and 1.0 M solutes in aqueous solution<sup>20</sup>

Reaction	<i>E</i> <sup>0</sup>	Products or name
$x\text{CO}_2 + n\text{H}^+ + ne^- \rightarrow \text{product} + y\text{H}_2\text{O}$		CO <sub>2</sub> reaction
CO <sub>2</sub> + e <sup>-</sup> → CO <sub>2</sub> <sup>*</sup>	-1.90 V vs. SHE	Carbonate anion radical
CO <sub>2</sub> + 2H <sup>+</sup> + 2e <sup>-</sup> → CO (g) + H <sub>2</sub> O	-0.10 V vs. RHE	Carbon monoxide
CO <sub>2</sub> + 2H <sup>+</sup> + 2e <sup>-</sup> → HCOOH (aq) + H <sub>2</sub> O	-0.12 V vs. RHE	Formic acid
2CO <sub>2</sub> + 2H <sup>+</sup> + 2e <sup>-</sup> → (COOH) <sub>2</sub> (s)	-0.47 V vs. RHE	Oxalic acid
CO <sub>2</sub> + 4H <sup>+</sup> + 4e <sup>-</sup> → C (s) + 2H <sub>2</sub> O	0.21 V vs. RHE	Graphite
CO <sub>2</sub> + 4H <sup>+</sup> + 4e <sup>-</sup> → HCHO (s) + H <sub>2</sub> O	-0.10 V vs. RHE	Formaldehyde
CO <sub>2</sub> + 6H <sup>+</sup> + 6e <sup>-</sup> → CH <sub>3</sub> OH (aq) + H <sub>2</sub> O	0.03 V vs. RHE	Methanol
CO <sub>2</sub> + 8H <sup>+</sup> + 8e <sup>-</sup> → CH <sub>4</sub> (g) + 2H <sub>2</sub> O	0.17 V vs. RHE	Methane
2CO <sub>2</sub> + 8H <sup>+</sup> + 8e <sup>-</sup> → CH <sub>3</sub> COOH (aq) + 2H <sub>2</sub> O	0.11 V vs. RHE	Acetic acid
2CO <sub>2</sub> + 10H <sup>+</sup> + 10e <sup>-</sup> → CH <sub>3</sub> CHO (aq) + 3H <sub>2</sub> O	0.66 V vs. RHE	Acetaldehyde
2CO <sub>2</sub> + 12H <sup>+</sup> + 12e <sup>-</sup> → C <sub>2</sub> H <sub>4</sub> (g) + 4H <sub>2</sub> O	0.08 V vs. RHE	Ethylene
2CO <sub>2</sub> + 12H <sup>+</sup> + 12e <sup>-</sup> → C <sub>2</sub> H <sub>5</sub> OH (aq) + 3H <sub>2</sub> O	0.09 V vs. RHE	Ethanol
2CO <sub>2</sub> + 14H <sup>+</sup> + 14e <sup>-</sup> → C <sub>2</sub> H <sub>6</sub> (g) + 4H <sub>2</sub> O	0.14 V vs. RHE	Ethane
3CO <sub>2</sub> + 16H <sup>+</sup> + 126e <sup>-</sup> → C <sub>2</sub> H <sub>5</sub> CHO (aq) + 5H <sub>2</sub> O	0.09 V vs. RHE	Propionaldehyde
3CO <sub>2</sub> + 18H <sup>+</sup> + 18e <sup>-</sup> → C <sub>3</sub> H <sub>7</sub> OH (aq) + 5H <sub>2</sub> O	0.10 V vs. RHE	Propanol
2H <sup>+</sup> + 2e <sup>-</sup> → H <sub>2</sub> (g)	0 V vs. RHE	Hydrogen
H <sub>2</sub> O → O <sub>2</sub> (g) + 4H <sup>+</sup> + 4e <sup>-</sup>	1.23 V vs. RHE	Oxygen

electrons and multiple protons and the thermodynamic reduction potentials of different reaction pathways are very close, it will produce many types of products with poor selectivity. Thirdly, it is still difficult to realize the production of high-value-added C<sub>2+</sub> reduction products *via* the ECRR in a single electrolysis device. Finally, the upstream supply of CO<sub>2</sub> and the purification of downstream products still face challenges. Thus, to address these challenges, it is necessary to develop highly efficient and highly selective CO<sub>2</sub> reduction electrocatalysts to promote ECRR technology for industrial applications.<sup>137–142</sup>

## 5.2 Electrocatalytic N<sub>2</sub> reduction reaction

An N<sub>2</sub> molecule is composed of two N atoms and each N atom has a total of 5 valence electrons in its outer 2s and 2p orbitals. In an N<sub>2</sub> molecule, the 4 s-p atomic orbitals on each N atom combine to generate 8 new molecular orbitals (4 bonding orbitals with 2σ and 2π orbitals and 4 antibonding orbitals with 2σ\* and 2π\* orbitals), as shown in Fig. 6.<sup>160</sup> The shared electrons on the π and 2σ orbitals form a high-strength N≡N triple bond. Thus, the N<sub>2</sub> molecule is very stable and is usually used to provide an inert atmosphere. The high dissociation energy of the N≡N triple bond (941 kJ mol<sup>-1</sup>) with a bond length of 110 pm cannot be fully used to explain the inertness of the N<sub>2</sub> molecule. This is because the dissociation energy of the HC≡CH (962 kJ mol<sup>-1</sup>) in C<sub>2</sub>H<sub>2</sub> and the triple bond (1070 kJ mol<sup>-1</sup>) in CO are also much higher than that of the N≡N triple bond, but both are more active than N<sub>2</sub>.<sup>143,144</sup> Here, the difference is thought to be that 410 kJ mol<sup>-1</sup> is required to dissociate the first bond in N≡N, which is almost half of the total dissociation energy, but only 222 kJ mol<sup>-1</sup> is needed for the cleavage of the first bond in HC≡CH, proving that the initiation of the triple bond dissociation in N<sub>2</sub> is much more difficult. Additionally, the N<sub>2</sub> molecule lacks permanent dipoles with a negative electron affinity of -1.90 eV, an ionization potential of 15.84 eV, and a proton affinity of 493.8 kJ mol<sup>-1</sup>, which is even lower than that of CH<sub>4</sub> (543.5 kJ mol<sup>-1</sup>). These

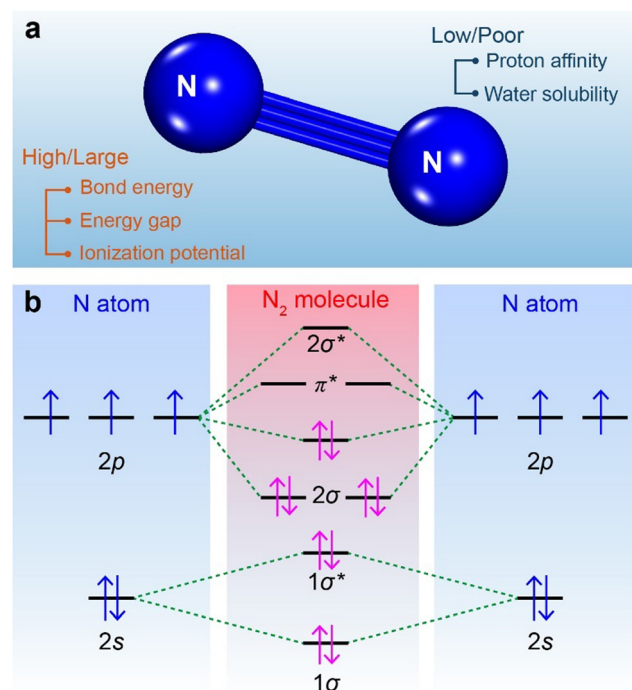


Fig. 6 (a) Molecular structure of N<sub>2</sub>. (b) Schematic of N atomic orbitals and N<sub>2</sub> molecular orbitals. Reproduced with permission from ref. 148. Copyright 2020, the American Chemical Society.

unique molecular characteristics increase the resistance of the N<sub>2</sub> molecule to Lewis acids/bases. Moreover, N<sub>2</sub> has a significant unfavorable energy gap (10.82 eV), making electron transport difficult.<sup>145,146</sup> Therefore, N<sub>2</sub> molecules are difficult to activate. Consequently, the direct protonation of N<sub>2</sub> is not possible under ambient conditions, even under strong acid conditions.<sup>145,147</sup>

Considering that N<sub>2</sub> is the main component in the Earth's atmosphere, N<sub>2</sub> fixation *via* the conversion of atmospheric N<sub>2</sub> to ammonia (NH<sub>3</sub>) has been regarded as a promising industrial process. NH<sub>3</sub> not only plays a key role in producing fertilizers,

organisms, drugs and chemicals to sustain the rising global population but also serves as a green energy carrier as an alternative transportation fuel.<sup>149–153</sup> Biological N<sub>2</sub> fixation occurs in nature when atmospheric N<sub>2</sub> is converted to NH<sub>3</sub> by nitrogenase enzyme in the presence of water and iron-molybdenum cofactor. This biological N<sub>2</sub> fixation process is vital to sustaining life on Earth. However, the ultralow natural biological N<sub>2</sub> fixation rate seriously restricts its industrial application. In industry, the dominant N<sub>2</sub> fixation to produce NH<sub>3</sub> is the Haber process, also known as the Haber–Bosch process. NH<sub>3</sub> is a required precursor to produce fertilizers, explosives, and other important products. The industrial N<sub>2</sub>-to-NH<sub>3</sub> conversion requires high pressures (>10 MPa) and high temperatures (>400 °C) over Ru- or Fe-based catalysts. On each pass, only about 15% of N<sub>2</sub>-to-NH<sub>3</sub> conversion occurs, but any unreacted gases are recycled, and eventually, an overall conversion of 97% is achieved. Furthermore, high temperatures are needed to offset the sluggish kinetics of this reaction. However, the thermodynamics of this process favors NH<sub>3</sub> decomposition to N<sub>2</sub> and H<sub>2</sub> at elevated temperatures, and hence high pressure is also required. Besides, additional energy is usually required to obtain the pure feed gases, pressurization, etc. Under these harsh conditions, the N<sub>2</sub>-to-NH<sub>3</sub> conversion process requires a high energy input of roughly 485 kJ mol<sup>−1</sup>. Consequently, the industrial N<sub>2</sub> fixation process alone consumes about 2% of the global annual energy supply and produces about 2.0 tons of CO<sub>2</sub> for every ton of NH<sub>3</sub> produced, accounting for about 1% of the annual greenhouse gas emissions globally.<sup>37,147,154–157</sup> Therefore, the development of eco-friendly, highly efficient, and sustainable alternative approaches for N<sub>2</sub> fixation is urgent.

Among the various artificial N<sub>2</sub> fixation methods, driven by renewable electricity, the ENRR has emerged as a very attractive approach for the fixation and high-value conversion of N<sub>2</sub> under mild conditions.<sup>158–164</sup> Compared with the Haber–Bosch process, the electrochemical N<sub>2</sub> fixation process has additional advantages, as follows: (1) potentially higher energy efficiency than that for the traditional Haber–Bosch process; (2) environmental compatibility through coupling with carbon-free renewable energy resources (solar, tidal, and wind energy); (3) elimination of fossil fuels as H<sub>2</sub> sources, whereby the required protons are generated *in situ* from water oxidation; (4) flexible control of the reactions by adjusting external parameters (such as voltage and current), which is attractive for modular and small-scale operations; and (5) good scalability for on-demand, on-site NH<sub>3</sub> production.

Similar to the ECRR, the ENRR process also occurs at the electrode–electrolyte three-phase interface and requires proton transfer from the electrolyte, electron transfer from the electrode, and optimized active sites on the electrode surface onto which the N<sub>2</sub> molecules can be adsorbed, and subsequently activated. Accordingly, three major elementary steps should be considered when modeling the fundamental processes for the ENRR, as follows: (1) the diffusion and chemical adsorption of N<sub>2</sub> molecules and protons on the cathode surface; (2) the cleavage and hydrogenation of N≡N triple bond; and (3)

rearrangement and desorption of the NH<sub>3</sub> product, or other reduction products (*e.g.*, hydrazine and diazene) from the electrode surface and migration to the electrolyte.

Thermodynamically, N<sub>2</sub> can be completely hydrogenated to form NH<sub>3</sub>, but this does not occur naturally. The formation of NH<sub>3</sub> from the ENRR has a very high energy barrier due to the fact that the partially hydrogenated N<sub>2</sub>H<sub>2</sub> ( $\Delta H_f^\circ = 212.9 \text{ kJ mol}^{-1}$ ) and N<sub>2</sub>H<sub>4</sub> ( $\Delta H_f^\circ = 95.35 \text{ kJ mol}^{-1}$ ) have high enthalpies of formation, given that the energy of their possible intermediates (*e.g.*, \*N<sub>2</sub>H and \*NH<sub>2</sub>, respectively) is expected to be high.<sup>165,166</sup> In the electrosynthesis of NH<sub>3</sub>, the chemisorbed intermediate complexes provide an alternative reaction pathway, in which the energy barrier is significantly reduced, and thus it can even be overcome by thermal energy.<sup>165</sup> However, given that the proton affinities of N<sub>2</sub>H<sub>2</sub> and N<sub>2</sub>H<sub>4</sub> are as high as 803 and 853.2 kJ mol<sup>−1</sup>, respectively, which are significantly higher than that of N<sub>2</sub>, this indicates that they are more protonated than N<sub>2</sub>. Thus, a large energy input is still required. Moreover, the energy gap (7.44 eV) of N<sub>2</sub>H<sub>4</sub> is also lower than that of N<sub>2</sub> (10.82 eV),<sup>144,162</sup> which makes the N≡N bond unfavorable for electron transfer. Therefore, these features of the N<sub>2</sub> molecule impede electron transfer and the reaction kinetics for the ENRR and NH<sub>3</sub> production.<sup>166</sup>

Theoretically, when a sufficiently negative potential is applied to the electrodes, it should be possible to achieve the ENRR under ambient conditions.<sup>167</sup> The equilibrium potentials ( $E^0$ ) of the ENRR process and the HER process are comparable in both acidic and alkaline electrolytes (Table 2), indicating that the HER process is the main competing reaction,<sup>168</sup> while the HER only requires two electrons for each H<sub>2</sub> produced in a single-half reaction. However, the ENRR is a multi-step process involving the transfer of 6 electrons and 6 protons as well as multiple intermediates,<sup>144,169</sup> as summarized in Table 2. The higher reduction potential for the formation of the \*N<sub>2</sub>H intermediate indicates that the initial H atom addition (N<sub>2</sub> + H<sup>+</sup> + e<sup>−</sup> ⇌ N<sub>2</sub>H) is very difficult. In the process of N≡N triple bond breaking, the second and third bonds are easier to break than the first bond, and thus the potentials of the four- and six-electron reduction processes (N<sub>2</sub> + 4H<sup>+</sup> + 4e<sup>−</sup> ⇌ N<sub>2</sub>H<sub>4</sub> and N<sub>2</sub> + 4H<sub>2</sub>O + 6e<sup>−</sup> ⇌ N<sub>2</sub>H<sub>4</sub> + 4OH<sup>−</sup>) are lower than that of the one- and two-electron reduction processes (N<sub>2</sub> + H<sup>+</sup> + e<sup>−</sup> ⇌ N<sub>2</sub>H and N<sub>2</sub> + 2H<sup>+</sup> + 2e<sup>−</sup> ⇌ N<sub>2</sub>H<sub>2</sub>).<sup>147,170</sup> These higher reduction potentials for the ENRR intermediates suggest that N<sub>2</sub> hydrogenation is more difficult thermodynamically.

Table 2 The equilibrium potentials for the ENRR in aqueous solution

Reaction	$E^0$
N <sub>2</sub> + 6H <sup>+</sup> + 6e <sup>−</sup> ⇌ 2NH <sub>3</sub> (g)	−0.148 V vs. RHE
2H <sup>+</sup> + 2e <sup>−</sup> ⇌ H <sub>2</sub> (g)	0 V vs. RHE
N <sub>2</sub> + 6H <sub>2</sub> O + 6e <sup>−</sup> ⇌ 2NH <sub>3</sub> + 6OH <sup>−</sup>	−0.736 V vs. SHE (pH 14)
2H <sub>2</sub> O + 2e <sup>−</sup> ⇌ H <sub>2</sub> + 2OH <sup>−</sup>	0 V vs. RHE
N <sub>2</sub> + H <sup>+</sup> + e <sup>−</sup> ⇌ N <sub>2</sub> H (g)	−3.2 V vs. RHE
N <sub>2</sub> + 2H <sup>+</sup> + 2e <sup>−</sup> ⇌ N <sub>2</sub> H <sub>2</sub> (g)	−1.1 V vs. RHE
N <sub>2</sub> + 4H <sup>+</sup> + 4e <sup>−</sup> ⇌ N <sub>2</sub> H <sub>4</sub> (g)	−0.33 V vs. RHE
N <sub>2</sub> + 4H <sub>2</sub> O + 6e <sup>−</sup> ⇌ N <sub>2</sub> H <sub>4</sub> + 4OH <sup>−</sup>	−1.16 V vs. SHE (pH 14)
N <sub>2</sub> + 5H <sup>+</sup> + 4e <sup>−</sup> ⇌ N <sub>2</sub> H <sub>5</sub> <sup>+</sup> (aq)	−0.23 V vs. RHE
N <sub>2</sub> + e <sup>−</sup> ⇌ N <sub>2</sub> <sup>−</sup> (aq)	−3.37 V vs. RHE (pH 14)

A complex concerted proton–electron transfer (CPET) pathway or a sequential proton–electron transfer (SPET) pathway process is involved in the ENRR.<sup>144</sup> At present, it is not clear whether the electron and proton transfer in the ENRR process is CPET or SPET. The results in the literature show that the CPET process is preferred on the surface of metal-based catalysts, while the SPET process also plays an important role. The SPET process has a relatively small activation energy to couple with the H atom when a proton and electron are transferred synchronously in the CPET process. In the SPET process, firstly  $\text{H}^*$  tends to interact with the activated  $\text{N}_2$ , and then the electrons are transferred to the positively charged protonated  $\text{N}_2$  intermediate.<sup>171</sup> To date, the reported studies have shown that the use of the CPET or SPET process in the ENRR process depends on the pH value of the electrolyte.<sup>172</sup> However, most of the current theoretical calculations ignore the influence of pH when simulating the reaction process. Also, the reaction mechanism is not fully understood thus far due to the multi-step proton–electron transfer and various intermediates involved in the ENRR process. Thus, more research is needed.

In general, the electrochemical conversion of  $\text{N}_2$  to  $\text{NH}_3$  is based on two basic reaction mechanisms, namely, the dissociative pathway and associative pathway, which differ in terms of the different reaction intermediates involved (Fig. 7).<sup>174</sup> In the case of the dissociative pathway, the  $\text{N}\equiv\text{N}$  bond is broken first, and then hydrogenation occurs after the  $\text{N}_2$  molecules adsorb on the surface of the catalyst, which requires a large adsorption energy. According to the dissociative reaction mechanism, the adsorbed  $\text{N}_2$  molecules first undergo cleavage of the  $\text{N}\equiv\text{N}$  triple bond with a high energy input before the hydrogenation process due to the inertness of the  $\text{N}\equiv\text{N}$  bond, which explains why the Haber–Bosch process requires harsh

conditions, given that it follows the dissociative reaction pathway.<sup>175</sup> Regarding the associative pathway, the adsorbed  $\text{N}_2$  molecule binds with two H atoms before forming the first  $\text{NH}_3$  molecule. The breakage of the  $\text{N}\equiv\text{N}$  bonds occurs only when  $\text{NH}_3$  molecules are released during the ENRR process. Prior to this, the  $\text{N}_2$  molecules are first adsorbed on the surface of the heterogeneous catalyst, and then a multi-step  $1\text{H}^+/1\text{e}^-$  PCET process occurs.

According to the different hydrogenation sequences, the association pathway can be divided into the distal pathway and alternate pathway (Fig. 7). In the distal pathway, the successive hydrogenation of N atoms away from the catalyst surface releases an  $\text{NH}_3$  molecule, and then the remaining N atoms are re-hydrogenated to release a second  $\text{NH}_3$  molecule. In contrast, in the alternate pathway, two N atoms in the  $\text{N}_2$  molecule undergo a one-step  $1\text{H}^+/1\text{e}^-$  PCET process simultaneously, and then the two N atoms are alternately hydrogenated, and finally, two  $\text{NH}_3$  molecules are gradually released.<sup>144,147,176</sup>

The great progress achieved in the ENRR field is sufficient to confirm the feasibility of the electrochemical reduction of  $\text{N}_2$  to produce  $\text{NH}_3$  in aqueous solution under ambient conditions. However, great challenges are still encountered with the ENRR in both the design and preparation of catalysts and the precise detection of the  $\text{NH}_3$  product. With the rapid development of advanced characterization techniques and the continuous improvement of theoretical tools as well as the development of highly efficient, selective, and stable ENRR catalysts, the industrialization of artificial green  $\text{NH}_3$  synthesis will be realized in the near future.

### 5.3 Electrocatalytic $\text{NO}/\text{NO}_2^-/\text{NO}_3^-$ reduction reaction

The electrochemical reduction of  $\text{NO}/\text{NO}_2^-/\text{NO}_3^-$  is enriched by the fact that nitrogen is known to exist in at least ten different oxidation states ranging from  $-3$  to  $+5$ . The electrochemical reduction of  $\text{NO}/\text{NO}_2^-/\text{NO}_3^-$  involves reactant diffusion, adsorption, charge transfer, product desorption, and separation. Given that both  $\text{NO}_2^-$  and  $\text{NO}_3^-$  are negatively charged, their transport can be augmented by an electric field, which has been employed in capacitive desalination devices.<sup>177,178</sup> The adsorption of  $\text{NO}_2^-$  and  $\text{NO}_3^-$  on the active site is the first step for electrochemical reduction. The main processes that occur during the electrochemical reduction of  $\text{NO}/\text{NO}_2^-/\text{NO}_3^-$  are listed in Fig. 8. As shown,  $\text{NO}$  and  $\text{NO}_2^-$  are the key intermediates during the electrochemical reduction of  $\text{NO}_3^-$  to  $\text{NH}_3$  or  $\text{N}_2$ . Therefore, next, we introduce the electrochemical reduction mechanism of  $\text{NO}_3^-$  and further transition from the key intermediates ( $\text{NO}$  and  $\text{NO}_2^-$ ) to the introduction of the reduction mechanism of  $\text{NO}$  and  $\text{NO}_2^-$ . Overall, the electrochemical reduction mechanism of  $\text{NO}/\text{NO}_2^-/\text{NO}_3^-$  will be systematically introduced in this section.

The formation of  $\text{NO}_3^-$  often proceeds *via* a concerted electrochemical–chemical–electrochemical mechanism. In detail, the initial electrochemical reduction yields  $\text{NO}_3^{2-}$  with a short life span (about 20  $\mu\text{s}$ ) ( $\text{NO}_3(\text{ad})^- + \text{e}^- \rightarrow \text{NO}_3^{2-}$ ,  $E^\circ = -0.89$  V vs. SHE).<sup>180,181</sup> Then,  $\text{NO}_3^{2-}$  is hydrolyzed *via* a

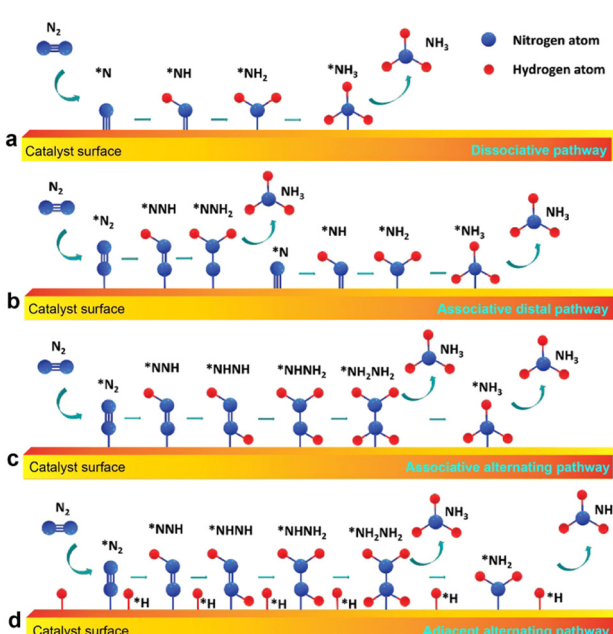
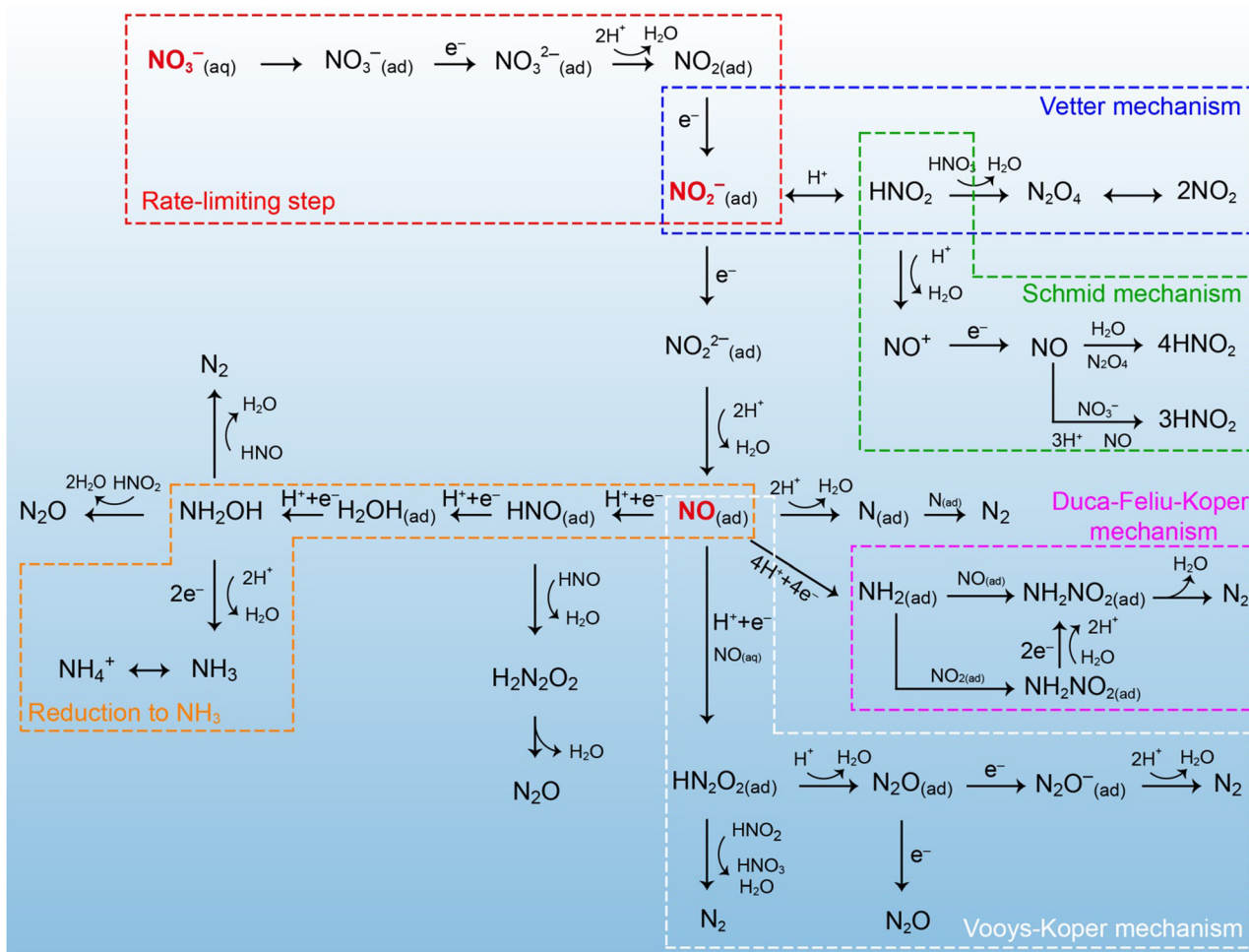


Fig. 7 Mechanisms of the ENRR. Reproduced with permission from ref. 173. Copyright 2019, Elsevier.



**Fig. 8** Various mechanisms and main processes during the electrochemical reduction of nitrate. Reproduced with permission from ref. 179. Copyright 2018, Elsevier.

homogenous chemical reaction to the nitrogen dioxide radical ( $\text{NO}_2^*$ ) ( $\text{NO}_{3(\text{ad})}^- + 2\text{H}^+ \rightarrow \text{NO}_{2(\text{ad})} + \text{H}_2\text{O}$ ).<sup>182</sup> Consequently,  $\text{NO}_2^*$  is further reduced to  $\text{NO}_2^-$ , which adsorbs on the substrate *via* a second electron transfer reaction ( $\text{NO}_{2(\text{ad})}^- + \text{e}^- \rightarrow \text{NO}_{2(\text{ad})}^-$ ,  $E^\circ = 1.04 \text{ V vs. SHE}$ ).<sup>181</sup> When the electrochemical reduction of  $\text{NO}_3^-$  to  $\text{NO}_2^-$  is performed at high acidity and concentration (1.0–4.0 M  $\text{NO}_3^-$ ), an autocatalytic reaction may simultaneously occur in the presence of a catalytic concentration of  $\text{HNO}_2$  ( $>10^{-6} \text{ M}$ ).<sup>183</sup> Different initiators in the catalytic cycle result in two possible autocatalytic mechanisms, as follows: (1) the Vetter mechanism<sup>184</sup> and (2) the Schmid mechanism.<sup>185,186</sup>

In the Vetter mechanism,  $\text{NO}_2^*$  acts as the electroactive species in the autocatalytic cycle. The electroreduction of  $\text{NO}_2$  will generate  $\text{NO}_2^-$ , which protonates to  $\text{HNO}_2$  ( $\text{NO}_2^- + \text{H}^+ \rightarrow \text{HNO}_2$ ) under highly acidic conditions. The  $\text{NO}_2^*$  species will be propagated in the autocatalytic cycle ( $\text{HNO}_2 + \text{HNO}_3 \rightarrow \text{N}_2\text{O}_4 + \text{H}_2\text{O}$ ;  $\text{N}_2\text{O}_4 \rightarrow 2\text{NO}_2$ ), in which  $\text{HNO}_2$  reacts with  $\text{HNO}_3$ , yielding  $\text{N}_2\text{O}_4$ , which quickly releases two electroactive  $\text{NO}_2$  species.

In the Schmid mechanism, the deprotonation of  $\text{HNO}_2$  ( $\text{HNO}_2 + \text{H}^+ \rightarrow \text{NO}^+ + \text{H}_2\text{O}$ ) in highly acidic electrolytes will

produce  $\text{NO}^+$ , which will be formed to  $\text{NO}$  by capturing an  $\text{e}^-$  ( $\text{NO}^+ + \text{e}^- \rightarrow \text{NO}$ ,  $E^\circ = 1.28 \text{ V vs. SHE}$ ).<sup>187</sup> Subsequently,  $\text{NO}$  species will react with  $\text{N}_2\text{O}_4$  or  $\text{HNO}_3$  to form  $\text{HNO}_2$  ( $\text{N}_2\text{O}_4 + 2\text{NO} + \text{H}_2\text{O} \rightarrow 4\text{HNO}_2$  or  $\text{HNO}_3 + 2\text{NO} + \text{H}_2\text{O} \rightarrow 3\text{HNO}_2$ ).<sup>188,189</sup>

Both mechanisms occur only in highly acidic conditions below nitrate concentrations of 4.0 M. At nitric acid concentrations of  $>4.0 \text{ M}$ , nitric acid naturally decomposes into  $\text{NO}$  and  $\text{N}_2\text{O}_4$  ( $2\text{HNO}_3 \rightarrow 2\text{NO} + 3/2\text{O}_2 + \text{H}_2\text{O}$ ;  $2\text{HNO}_3 \rightarrow 2\text{N}_2\text{O}_4 + 1/2\text{O}_2 + \text{H}_2\text{O}$ ).<sup>190</sup> Both  $\text{NO}$  and  $\text{N}_2\text{O}_4$  can lead to the formation of  $\text{HNO}_2$  ( $\text{N}_2\text{O}_4 + 2\text{NO} + \text{H}_2\text{O} \rightarrow 4\text{HNO}_2$  or  $\text{HNO}_3 + 2\text{NO} + \text{H}_2\text{O} \rightarrow 3\text{HNO}_2$ ), which occurs without requiring electrochemical charge transfer reactions. Therefore, they cannot be considered a part of an indirect electrochemical reduction of  $\text{NO}_3^-$  in an autocatalytic cycle.

With the further reduction of  $\text{NO}_2^-$ ,  $\text{NO}$  will be produced as a divergent center, leading to the formation of undesirable (*e.g.*,  $\text{NH}_4^+$  and  $\text{N}_2\text{O}$ ) and innocuous (*i.e.*,  $\text{N}_2$ ) products. The direct charge injection to  $\text{NO}_2^-$  leads to the formation of dianion radical  $\text{NO}_2^{2-}$  ( $\text{NO}_{2(\text{ad})}^- + \text{e}^- \rightarrow \text{NO}_{2(\text{ad})}^{2-}$ ,  $E^\circ = -0.47 \text{ V vs. SHE}$ ).<sup>191,192</sup> Similar to the unstable  $\text{NO}_3^{2-}$ , the dianion radical  $\text{NO}_2^{2-}$  will quickly hydrolyze and produce  $\text{NO}_{(\text{ad})}$  ( $\text{NO}_{2(\text{ad})}^{2-} + \text{H}_2\text{O} \rightarrow \text{NO}_{(\text{ad})} + 2\text{OH}^-$ ).<sup>193,194</sup> In weak acidic solution, the

reduction of  $\text{NO}_{\text{(ad)}}$  will lead to the formation of nitroxyl ( $\text{HNO}$ ) ( $\text{NO}_{\text{(ad)}}^- + \text{H}^+ + \text{e}^- \rightarrow \text{HNO}_{\text{(ad)}}$ ,  $E^\theta = -0.78 \text{ V vs. SHE}$ ). Katsounaros and Kyriacou identified that  $\text{HNO}$  can dimerize into hyponitrous acid ( $\text{H}_2\text{N}_2\text{O}_2$ ) ( $\text{HNO} + \text{HNO} \rightarrow \text{H}_2\text{N}_2\text{O}_2$ ). Under ambient conditions, the chemical decomposition of the unstable  $\text{H}_2\text{N}_2\text{O}_2$  to  $\text{N}_2\text{O}$  occurs ( $\text{H}_2\text{N}_2\text{O}_2 \rightarrow \text{N}_2\text{O} + \text{H}_2\text{O}$ ).

In an alternative reaction path, NO can be electrocatalytically dimerized to produce  $\text{N}_2\text{O}$  ( $\text{NO}_{\text{(ad)}} + \text{NO}_{\text{(aq)}} + \text{H}^+ + \text{e}^- \rightarrow \text{HN}_2\text{O}_{2\text{(ad)}}, E^\theta = 0 \text{ V vs. SHE}$ ;  $\text{HN}_2\text{O}_{2\text{(ad)}} + \text{H}^+ + \text{e}^- \rightarrow \text{N}_2\text{O}_{\text{(ad)}} + \text{H}_2\text{O}, E^\theta = 1.59 \text{ V vs. SHE}$ ).<sup>195,196</sup> Regarding  $\text{N}_2\text{O}$  formation, early studies on Pt suggested that it may adopt the Langmuir–Hinshelwood mechanism, in which two  $\text{NO}_{\text{(ad)}}$  yield dimers such as ON–NO, NOH–NO, and HON–NOH.<sup>197</sup> However, first-principles calculations show that it is energetically unfavorable for two  $\text{NO}_{\text{(ad)}}$  to proceed in the Langmuir–Hinshelwood-like reaction.<sup>198</sup> The Eley–Rideal-like mechanism has also been proposed, in which the solvated NO ( $\text{NO}_{\text{(aq)}}$ ) combines with  $\text{NO}_{\text{(ad)}}$  to create  $\text{HN}_2\text{O}_{2\text{(ad)}}$ .<sup>199</sup> Further,  $\text{HN}_2\text{O}_{2\text{(ad)}}$  is reduced to  $\text{N}_2\text{O}_{\text{(ad)}}$  ( $\text{HN}_2\text{O}_{2\text{(ad)}} + \text{H}^+ + \text{e}^- \rightarrow \text{N}_2\text{O}_{\text{(ad)}} + \text{H}_2\text{O}, E^\theta = 1.59 \text{ V vs. SHE}$ ). In this reaction system, the autocatalytic process will be inhibited due to the continuous consumption of NO. For  $\text{N}_2$  evolution,  $\text{NO}_{\text{(ad)}}$  was reduced into  $\text{N}_{\text{(ad)}}$  by coupling two protons ( $\text{NO}_{\text{(ad)}} + 2\text{H}^+ + 2\text{e}^- \rightarrow \text{N}_{\text{(ad)}} + \text{H}_2\text{O}$ ). Subsequently, the two  $\text{N}_{\text{(ad)}}$  will be combined to form an  $\text{N}_2$  molecule ( $\text{N}_{\text{(ad)}} + \text{N}_{\text{(ad)}} \rightarrow 2\text{H}^+ + \text{N}_2$ ).<sup>200</sup> However, to date, this mechanism has not been confirmed experimentally.

For the electrochemical  $\text{NO}/\text{NO}_2^-/\text{NO}_3^-$  reduction,  $\text{NH}_3$  is the most desired product. The electrochemical-electrochemical theory is commonly recognized as the mechanism for the electrochemical conversion of NO to  $\text{NH}_3$ , which involves several consecutive direct charge transfer reactions. Also, the rate-determining step of the reaction is the reduction of  $\text{HNO}$  to  $\text{H}_2\text{NO}$  ( $\text{HNO}_{\text{(ad)}} + \text{H}^+ + \text{e}^- \rightarrow \text{H}_2\text{NO}_{\text{(ad)}}, E^\theta = 0.52 \text{ V vs. SHE}$ ),<sup>200</sup> which is followed by quick charge transfer, releasing hydroxylamine ( $\text{NH}_2\text{OH}$ ) ( $\text{H}_2\text{NO}_{\text{(ad)}} + \text{H}^+ + \text{e}^- \rightarrow \text{H}_2\text{NOH}_{\text{(ad)}}, E^\theta = 0.9 \text{ V vs. SHE}$ ).<sup>195</sup> Subsequently,  $\text{H}_2\text{NOH}$  is protonated depending on the pH ( $\text{pK}_a = 5.93$ ) ( $\text{H}_2\text{NOH} + \text{H}^+ \rightarrow \text{H}_3\text{NOH}^+$ ). Finally,  $\text{NH}_3$  is generated from the reduction of hydroxylamine coupling with two protons ( $\text{H}_2\text{NOH} + 2\text{H}^+ + 2\text{e}^- \rightarrow \text{NH}_3 + \text{H}_2\text{O}, E^\theta = 0.42 \text{ V vs. SHE}$ ).<sup>201</sup> Equilibrium between  $\text{NH}_3$  and  $\text{NH}_4^+$  will be achieved depending on the pH ( $\text{pK}_a = 9.25$ ) ( $\text{NH}_3 + \text{H}^+ \rightarrow \text{NH}_4^+$ ).<sup>202,203</sup>

## 6. Target products and mechanistic understanding of electrocatalytic C–N coupling reactions

The C–N coupling reaction, as an important strategy for efficiently constructing nitrogen-containing intermediates or miscellaneous compounds, has been widely used in the synthesis of drugs, natural products, ligands, and catalysts.<sup>204–212</sup> Therefore, it is particularly important in the fields of organic synthesis, materials chemistry, and biochemistry. The traditional methods for C–N coupling reactions often require the use of metal reagents or oxidants. However, the addition of metal reagents in the total synthesis of drugs and natural products

often requires multi-step post-treatments to remove the metal residues.<sup>213–216</sup> In this case, although non-metallic methods have been explored to facilitate the formation of C–N bonds,<sup>217</sup> oxidants or equivalent reducing agents are required, which will also produce corresponding by-products.

Organic electrosynthesis, as a new “green synthesis tool” for the preparation of organic compounds, has attracted increasing attention worldwide. Through organic electrosynthesis, many reactive active intermediates (e.g., carbon radicals, nitrogen radicals, and carbocations) can be efficiently generated, and the formed reactive active intermediates can be selectively applied for the construction of C–N bonds and C–C bonds.<sup>7,46,218</sup> Considering the importance of the C–N coupling reaction in the total synthesis of drugs and natural products as well as its application in materials chemistry and biochemistry, it is necessary to develop new, green, and efficient synthesis methods. As a new strategy for the synthesis of organic compounds, organic electrosynthesis utilizes electrons and holes for reduction and oxidation on the cathode and anode, respectively, to reduce or eliminate the use of metal catalysts or equivalent oxidants for conventional organic synthesis, making the electrolysis system cleaner, greener, and cost-effective. In recent years, numerous achievements have been made in organic electrochemistry and various new electrosynthesis strategies have been developed.<sup>7,46</sup> This has greatly enriched the types of electrochemical reactions and electrosynthesis methods have been widely recognized.

The study of electrosynthesis *via* C–N coupling reactions can be divided into two categories, as follows: (1) electrochemical oxidation to construct a C–N bond by directly oxidizing the reactant on the anode or by adding a medium and oxidizing the medium on the anode to generate an active intermediate, which subsequently interacts with the substrate (*i.e.*, indirect oxidation). Consequently, the use of metal reagents or equivalent chemical oxidants can be reduced or eliminated. When the oxidation potential of the substrate is low, C–N coupling can be achieved by direct oxidation. When the oxidation potential of the substrate is high, it is necessary to add a medium to construct C–N coupling through indirect oxidation. (2) Electrochemical reduction to construct the C–N bond by directly reducing the substrate or by adding a medium and reducing the medium on the cathode to generate active intermediates, which subsequently react with the substrate. The construction of C–N coupling through electrochemical reduction can also reduce or eliminate the addition of reducing agents in traditional methods to reduce the wastage of reagents. However, compared to the widely reported anode oxidation strategies, the construction of C–N bonds through electrochemical reduction has been much less discussed.

The electrosynthesis of compounds containing C–N bond(s) from earth-abundant carbon ( $\text{CO}_2$ ) and nitrogen ( $\text{N}_2, \text{NO}_3^-, \text{NO}_2^-, \text{NO}$ , etc.) sources can efficiently decrease the carbon footprint for a more sustainable economy. Combining the renewable-energy-driven  $\text{CO}_2$  and  $\text{N}_2$  activation/conversion with the electrocatalytic C–N coupling reaction is a promising alternative approach to the highly selective synthesis of

C–N-coupled chemical products. As previously reported, electrochemical C–N coupling reactions can produce various compounds containing C–N bond(s), including urea, amide, amine, acetamide, ethylamine, formamide, glycine, and methylamine. Table 3 summarizes various electrocatalysts reported for the electrocatalytic C–N coupling reactions with significant industrial and economic benefits.<sup>31,43,219</sup>

Electrocatalytic C–N coupling reactions can directly convert the abundant CO<sub>2</sub> and nitrogenous small molecules into

various targeted high-value-added organonitrogen compounds, as summarized in Table 1. Although the electrosynthesis C–N coupling reactions based on CO<sub>2</sub>/N<sub>2</sub> and their derivatives present a unique opportunity for the production of high-value-added organonitrogen, it is also highly challenging. Currently, there is still a lack of mechanistic understanding of electrocatalytic C–N coupling reactions. A limiting factor is the complexity of the electrocatalytic C–N coupling, in which multiple reactions occur simultaneously.<sup>30</sup> For example, recent research revealed

**Table 3** Summary of the previously reported state-of-the-art electrocatalysts for the electrocatalytic C–N coupling reactions based on CO<sub>2</sub> as the carbon source and different nitrogenous small molecules as nitrogen sources

Catalyst	N source	C source	Medium	Product	Yield rate	FE (%)	E (V vs. RHE)	Quantification method	Reactor	Ref.
Cu	CO	NH <sub>3</sub>	1.0 M KOH	Acetamide	—	38	−0.68	<sup>1</sup> H NMR	Flow cell	31
Cu	CO <sub>2</sub>	NH <sub>3</sub>	1.0 M KOH	Formamide	—	0.4	−0.58	<sup>1</sup> H NMR	GDE	220
ER-Cu	HCOO <sup>−</sup>	NO <sub>2</sub> <sup>−</sup>	0.5 M NaOH	Formamide	35.1 mmol h <sup>−1</sup> g <sup>−1</sup>	29.7	−0.4	HPLC	H-Cell	221
Boron-doped diamond	CH <sub>3</sub> OH	NH <sub>3</sub>	0.5 M NaHCO <sub>3</sub>	Formamide	461.4 μmol h <sup>−1</sup> cm <sup>−2</sup>	73.2	—	<sup>1</sup> H NMR	H-Cell	222
Te-doped Pd	CO <sub>2</sub>	NO <sub>2</sub> <sup>−</sup>	0.1 M KHCO <sub>3</sub>	Urea	—	2	−1.1	Urease	H-Cell	35
ZnO-V <sub>o</sub>	CO <sub>2</sub>	NO <sub>2</sub> <sup>−</sup>	0.2 M NaHCO <sub>3</sub>	Urea	16.56 μmol h <sup>−1</sup>	23.26	−0.79	HPLC	H-Cell	223
AuCu SANFs	CO <sub>2</sub>	NO <sub>2</sub> <sup>−</sup>	0.5 M KHCO <sub>3</sub>	Urea	3889.6 μg h <sup>−1</sup> mg <sup>−1</sup>	24.7	−1.55 V vs. Urease Ag/AgCl		H-Cell	224
Cu–TiO <sub>2</sub>	CO <sub>2</sub>	NO <sub>2</sub> <sup>−</sup>	0.2 M KHCO <sub>3</sub>	Urea	20.8 μmol h <sup>−1</sup>	43.1	−0.4	Urease	H-Cell	34
Ni-PC	CO <sub>2</sub>	NO <sub>3</sub> <sup>−</sup>	0.2 M KHCO <sub>3</sub>	Urea	—	41	−1.1	Urease	GDE	225
TiO <sub>2</sub> /Nafion	CO <sub>2</sub>	NO <sub>3</sub> <sup>−</sup>	0.1 M KNO <sub>3</sub>	Urea	—	0	−0.5	Urease	H-Cell	226
In(OH) <sub>3</sub> S	CO <sub>2</sub>	NO <sub>3</sub> <sup>−</sup>	0.1 M KNO <sub>3</sub>	Urea	533.1 μg h <sup>−1</sup> mg <sup>−1</sup>	53.4	−0.6	Diacetylmonoxime	H-Cell	36
XC72R-AuPd	CO <sub>2</sub>	NO <sub>3</sub> <sup>−</sup>	0.075 M KHCO <sub>3</sub>	Urea	204.3 μg h <sup>−1</sup> mg <sup>−1</sup>	15.6	−0.5	Diacetylmonoxime	H-Cell	227
BFeNi-DASC	CO <sub>2</sub>	NO <sub>3</sub> <sup>−</sup>	0.075 M KHCO <sub>3</sub>	Urea	20.2 mmol h <sup>−1</sup> g <sup>−1</sup>	17.8	−1.5	Urease	H-Cell	228
V <sub>o</sub> -InOOH	CO <sub>2</sub>	NO <sub>3</sub> <sup>−</sup>	Deionized water	Urea	592.5 μg h <sup>−1</sup> mg <sup>−1</sup>	51	−0.5	UV-vis	H-Cell	229
F-CNT	CO <sub>2</sub>	NO <sub>3</sub> <sup>−</sup>	Deionized water	Urea	6.36 mmol h <sup>−1</sup> g <sup>−1</sup>	18.0	−0.65	UV-vis	H-Cell	230
Cu SACs	CO <sub>2</sub>	NO <sub>3</sub> <sup>−</sup>	0.1 M K <sub>2</sub> SO <sub>4</sub>	Urea	1800 μg h <sup>−1</sup> mg <sup>−1</sup>	28	−0.9	UV-vis	H-Cell	231
Oxide-derived Cu	CO <sub>2</sub>	NO <sub>3</sub> <sup>−</sup>	1.0 M KHCO <sub>3</sub>	Ethylamine	—	0.3	−1.0	Diacetylmonoxime	H-Cell	232
Vo-CeO <sub>2</sub> -750	CO <sub>2</sub>	NO <sub>3</sub> <sup>−</sup>	0.1 M KHCO <sub>3</sub>	Urea	943.6 mg h <sup>−1</sup> g <sup>−1</sup>	—	−1.6	Urease	H-Cell	233
Cu@Zn	CO <sub>2</sub>	NO <sub>3</sub> <sup>−</sup>	0.2 M KHCO <sub>3</sub>	Urea	7.29 μmol cm <sup>−2</sup> h <sup>−1</sup>	9.28	−1.75 V vs. SCE	HPLC	H-Cell	234
CoPC-NH <sub>2</sub> /CNT	CO <sub>2</sub>	NO <sub>3</sub> <sup>−</sup>	0.1 M KHCO <sub>3</sub>	Methylamine	—	13	−0.92	<sup>1</sup> H NMR	H-Cell	235
Pd <sub>1</sub> Cu <sub>1</sub> /TiO <sub>2</sub> -400	CO <sub>2</sub>	N <sub>2</sub>	0.1 M KHCO <sub>3</sub>	Urea	3.36 mmol g <sup>−1</sup> h <sup>−1</sup>	8.92	−0.4	Diacetylmonoxime + <sup>1</sup> H NMR	H-Cell + flow cell	32
Co-PMDA-2-mBiIM	CO <sub>2</sub>	N <sub>2</sub>	0.1 M KHCO <sub>3</sub>	Urea	14.5 μmol g <sup>−1</sup> h <sup>−1</sup>	49	−0.5	Diacetylmonoxime	H-Cell	236
Bi/BiVO <sub>4</sub>	CO <sub>2</sub>	N <sub>2</sub>	0.1 M KHCO <sub>3</sub>	Urea	5.91 mmol g <sup>−1</sup> h <sup>−1</sup>	12.55	0.4	Diacetylmonoxime + <sup>1</sup> H NMR	H-Cell	237
BiFeO <sub>3</sub> /BiVO <sub>4</sub>	CO <sub>2</sub>	N <sub>2</sub>	0.1 M KHCO <sub>3</sub>	Urea	4.94 mmol g <sup>−1</sup> h <sup>−1</sup>	17.18	−0.4	Diacetylmonoxime + <sup>1</sup> H NMR	H-Cell	238
Ni <sub>3</sub> (BO <sub>3</sub> ) <sub>2</sub>	CO <sub>2</sub>	N <sub>2</sub>	0.1 M KHCO <sub>3</sub>	Urea	9.7 mmol g <sup>−1</sup> h <sup>−1</sup>	20.36	−0.5	Diacetylmonoxime	H-Cell	239
InOOH	CO <sub>2</sub>	N <sub>2</sub>	0.1 M KHCO <sub>3</sub>	Urea	6.85 mmol g <sup>−1</sup> h <sup>−1</sup>	21.97	−0.4	Diacetylmonoxime	H-Cell	219
CuPc NTs	CO <sub>2</sub>	N <sub>2</sub>	0.1 M KHCO <sub>3</sub>	Urea	2.39 mmol g <sup>−1</sup> h <sup>−1</sup>	12.99	−0.6	Diacetylmonoxime	H-Cell	240
Zn foil	CO <sub>2</sub>	NO	0.2 M KHCO <sub>3</sub>	Urea	15.13 mmol g <sup>−1</sup> h <sup>−1</sup>	11.26	−0.92	HPLC	H-Cell + flow cell	237
Cu-Hg	Oxalic acid	NO	15 wt% H <sub>2</sub> SO <sub>4</sub>	Glycine	—	3	−1.2	<sup>1</sup> H NMR	H-Cell	241

Note: “—” means that no values were reported for the corresponding parameters in the corresponding references. FE, faradaic efficiency and GDE, gas diffusion electrode.

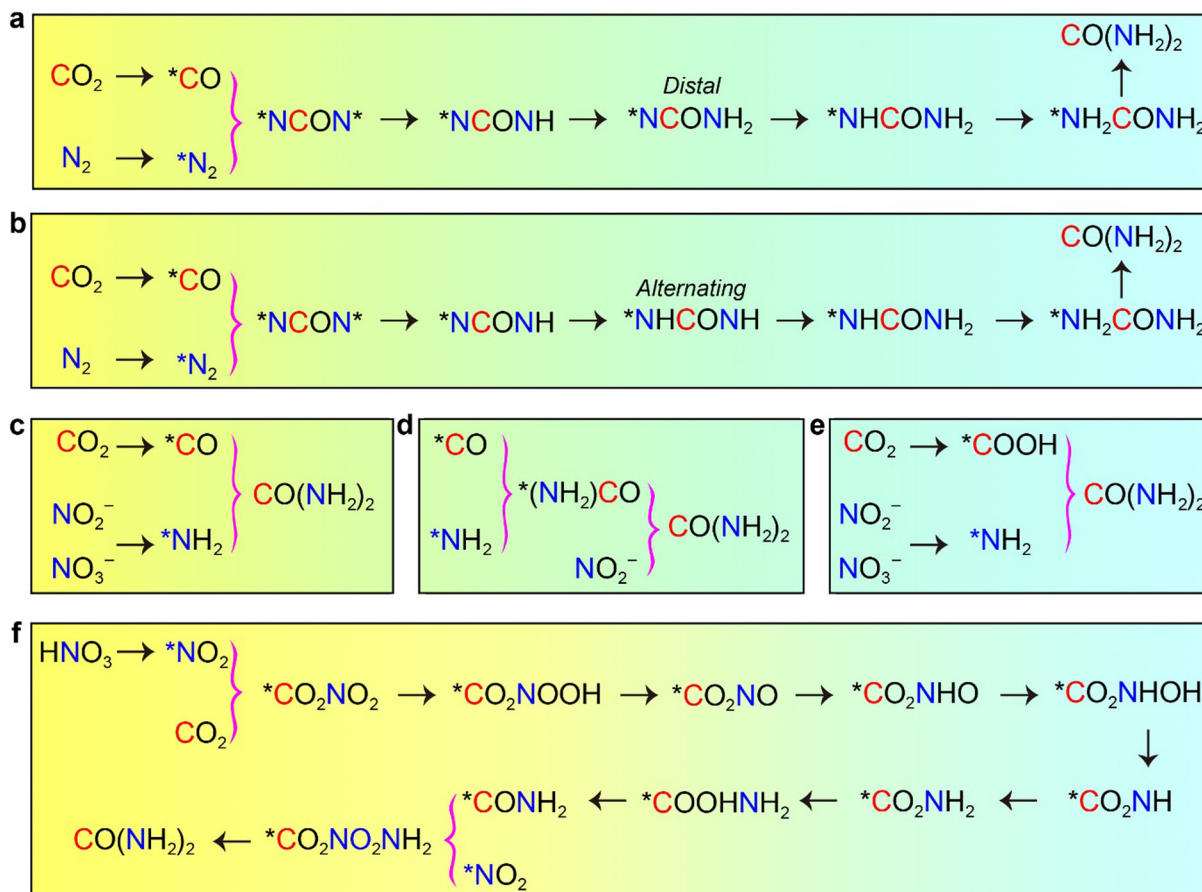


**Fig. 9** Different proposed mechanisms of urea electrosynthesis from  $\text{CO}_2$  and  $\text{N}_2$  and their derivatives: (a and b)  $*\text{CO} + *\text{N}_2$  coupling mechanisms with different hydrogenation routes and RDS.<sup>32,237</sup> (c)  $*\text{CO} + *\text{NH}_2$  coupling mechanism.<sup>243–245</sup> (d) Revised  $*\text{CO} + *\text{NH}_2$  coupling mechanism.<sup>225</sup> (e)  $*\text{COOH} + *\text{NH}_2$  coupling mechanism<sup>223</sup> and (f)  $*\text{CO}_2 + *\text{NO}_2$  coupling mechanism.<sup>36</sup> Purple braces indicate a C–N coupling step and black arrows indicate a reduction step. Reproduced with permission from ref. 30. Copyright 2022, the American Chemical Society.

that the formation of urea through electrocatalytic C–N coupling has many different reaction pathways, as summarized in Fig. 9. Moreover, at a high overpotential, C–N coupling reaction takes a different mechanism competing with the ECRR, ENRR, and HER. This leads to a narrow potential window for the formation of C–N products.<sup>242</sup> Therefore, further research is needed to gain a mechanistic understanding of the electrochemical C–N coupling reaction.

In general, many compounds containing C–N bonds are produced *via* two key intermediates ( $*\text{CO} + *\text{NH}_y$  and  $*\text{CH}_x + *\text{NH}_y$ ), which are introduced to form different chemical bonds and products, including  $\text{C}(=\text{O})-\text{N}$  and  $\text{C}\equiv\text{N}$  bonds.<sup>28</sup> For example, the simplest amide, urea, can be formed *via*  $*\text{CO}$  and  $*\text{NH}_y$  intermediates. Amines and nitriles are important C–N coupling products featuring the  $\text{C}\equiv\text{N}$  bond. In the early exploration of the electrocatalytic C–N coupling reaction, Shibata *et al.* observed that only the electrocatalysts that can promote the reduction of  $\text{CO}_2$  to CO and  $\text{NO}_2^-$  to  $\text{NH}_3$  can generate urea, but the control experiment did not produce urea when  $\text{CO}_2$  was replaced with CO or  $\text{NO}_2^-$  with  $\text{NH}_3$ .<sup>246,247</sup> These results led to the hypothesis that urea is directly formed from  $*\text{NH}_2$  and  $*\text{CO}$  intermediates *via* the reduction of  $\text{NO}_2^-$  and

$\text{CO}_2$ , respectively.<sup>243,244,247</sup> Later, this reaction mechanism was further revised by Shibata *et al.* given the observation that the  $\text{FE}_{\text{urea}}$  has a better linear relationship with  $(\text{FE}_{\text{CO}} \cdot \text{FE}_{\text{NH}_4^+})^{1/2}$  than with  $(\text{FE}_{\text{CO}} \cdot \text{FE}_{\text{NH}_4^+} \cdot \text{FE}_{\text{NH}_4^+})^{1/3}$ , which indicates the formation of  $(*\text{NH}_2)\text{CO}$  from  $*\text{CO}$  and  $*\text{NH}_2$  as the key C–N coupling step.<sup>245</sup> This was also observed by Shao *et al.*<sup>35</sup> and Zhang *et al.* using different electrocatalysts.<sup>223</sup>

Although the aforementioned experimental findings provided the first mechanistic framework for a fundamental understanding of the electrocatalytic C–N coupling reaction, more discussions on the following points are desirable: (1) compared with the +4 valent C in  $\text{CO}_2$  and urea molecule, the C atom in the  $*\text{CO}$  intermediate is in a reduced state, which indicates that  $\text{CO}_2$  is first reduced, and subsequently oxidized during the electrochemical C–N coupling reaction. (2) Under equilibrium conditions, CO and the  $*\text{CO}$  intermediate should coexist and be interconvertible. Using ECRR or by adding CO directly to the electrolyte, the  $*\text{CO}$  intermediate can be generated on the surface of the electrocatalyst,<sup>248,249</sup> which implies that similar  $*\text{CO}$  and  $*\text{NH}_2$  intermediates exist in the co-reduction of  $\text{CO} + \text{NO}_2^-$ . The fact that no urea was formed under this control condition, as verified by various

studies,<sup>35,223,243,246</sup> suggests that \*CO may not be a C–N coupling species. (3) The nucleophilic attack of \*NH<sub>2</sub> may be responsible for the reaction between \*NH<sub>2</sub> and \*CO. In theory, it is more advantageous for CO<sub>2</sub> to couple with a nucleophilic N intermediate due to the greater electrophilic character of CO<sub>2</sub> than CO. Furthermore, due to the charge delocalization and electron donation from the –NH<sub>2</sub> group, the hypothetical intermediate product of \*CONH<sub>2</sub> is less likely to undergo nucleophilic attack by another \*NH<sub>2</sub>.

Given the importance and complexity of the electrochemical C–N coupling reaction, we will discuss its formation mechanism in depth in conjunction with each target product. We focus on the design of the electrocatalyst and the reaction intermediates for the electrochemical C–N coupling reaction. In this section, various high-value-added products from the electrochemical C–N coupling reaction are also discussed with respect to the type of electrocatalyst used. For each type of electrocatalyst, the design strategy, performance, structure–activity relationship, product selectivity, and durability will be discussed through specific examples.

### 6.1. Urea

Among the numerous products from the electrochemical C–N coupling reaction, urea (CO(NH<sub>2</sub>)<sub>2</sub>), as one of the most efficient nitrogen fertilizers, is regarded as one of the most important products and is of great significance in the chemical industry.<sup>250</sup> Industrially, urea is mainly synthesized through two consecutive reaction steps, as follows: (1) reaction of NH<sub>3</sub> and CO<sub>2</sub> to form ammonium carbamate (NH<sub>3</sub> + CO<sub>2</sub> → NH<sub>2</sub>COONH<sub>4</sub>) and (2) decomposition of ammonium carbonate to form urea and water (NH<sub>2</sub>COONH<sub>4</sub> → H<sub>2</sub>O + CO(NH<sub>2</sub>)<sub>2</sub>), operating under harsh reaction conditions (180–210 °C; 150–250 bar), which results in intensive energy consumption.<sup>251–253</sup>

After reacting, the produced urea is evaporated and processed by prilling or granulating to obtain a solid end product (Fig. 10). In this process, NH<sub>3</sub> is manufactured by the energy-intensive Haber–Bosch method (N<sub>2</sub> + H<sub>2</sub> → NH<sub>3</sub>), which needs high energy input with high reaction temperatures (300–550 °C) and pressures (200–350 bar) and large H<sub>2</sub> input, requiring complex equipment and multi-step cycles to improve the conversion efficiency, and generating hundreds of millions of tons of CO<sub>2</sub>.<sup>4,176,254–257</sup>

Given the increasing global energy demand, it is highly desirable to develop green and efficient methods for the synthesis of urea. The ENRR has multiple advantages, including mild reaction conditions, utilization of clean energy, and obtaining protons from water. However, the separation and purification to obtain high-purity gaseous NH<sub>3</sub> for the subsequent synthesis of urea are too complicated to be practical for urea production *via* the sequential synthesis of NH<sub>3</sub> and CO<sub>2</sub>. Compared with the sequential industrial processes, the electrochemical synthesis of urea *via* N<sub>2</sub> + CO<sub>2</sub> + 6H<sup>+</sup> + 6e<sup>−</sup> → CO(NH<sub>2</sub>)<sub>2</sub> + H<sub>2</sub>O provides an appealing alternative under mild conditions.<sup>32</sup> Recently, technology to electrochemically convert N<sub>2</sub> and CO<sub>2</sub> to urea has received extensive attention.<sup>32,237</sup>

For example, Wang and co-workers<sup>32</sup> demonstrated an approach for the electrochemical coupling of CO<sub>2</sub> and N<sub>2</sub> in water to generate urea using an electrocatalyst consisting of PdCu alloy nanoparticles with an average particle size of 2–4 nm on oxygen vacancy-rich TiO<sub>2</sub> nanosheets (Pd<sub>1</sub>Cu<sub>1</sub>/TiO<sub>2</sub>-400) (Fig. 11a and b). Urea was quantitatively analyzed *via* the diacetyl monoxime method,<sup>258</sup> while the NH<sub>3</sub> and N<sub>2</sub>H<sub>4</sub> by-products were quantified by the indophenol blue method<sup>259</sup> and Watt and Chrisp method,<sup>260</sup> respectively. The experimental results showed that the introduction of oxygen vacancies promoted the catalytic activation of N<sub>2</sub> and CO<sub>2</sub>. In a flow cell, the

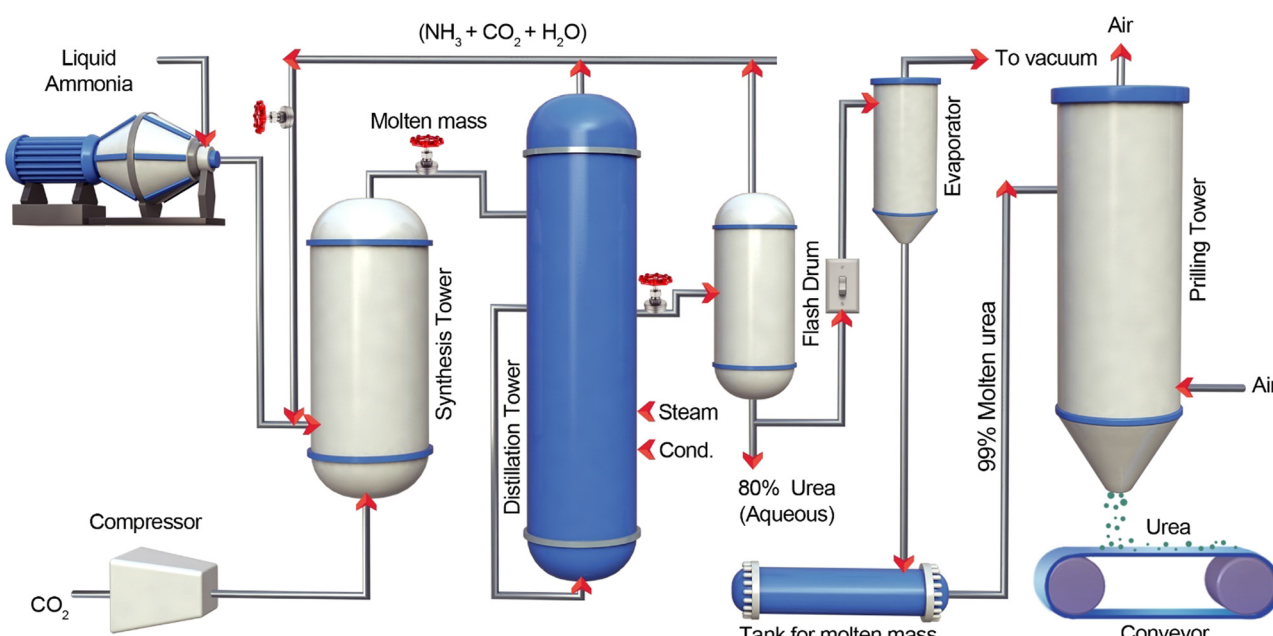
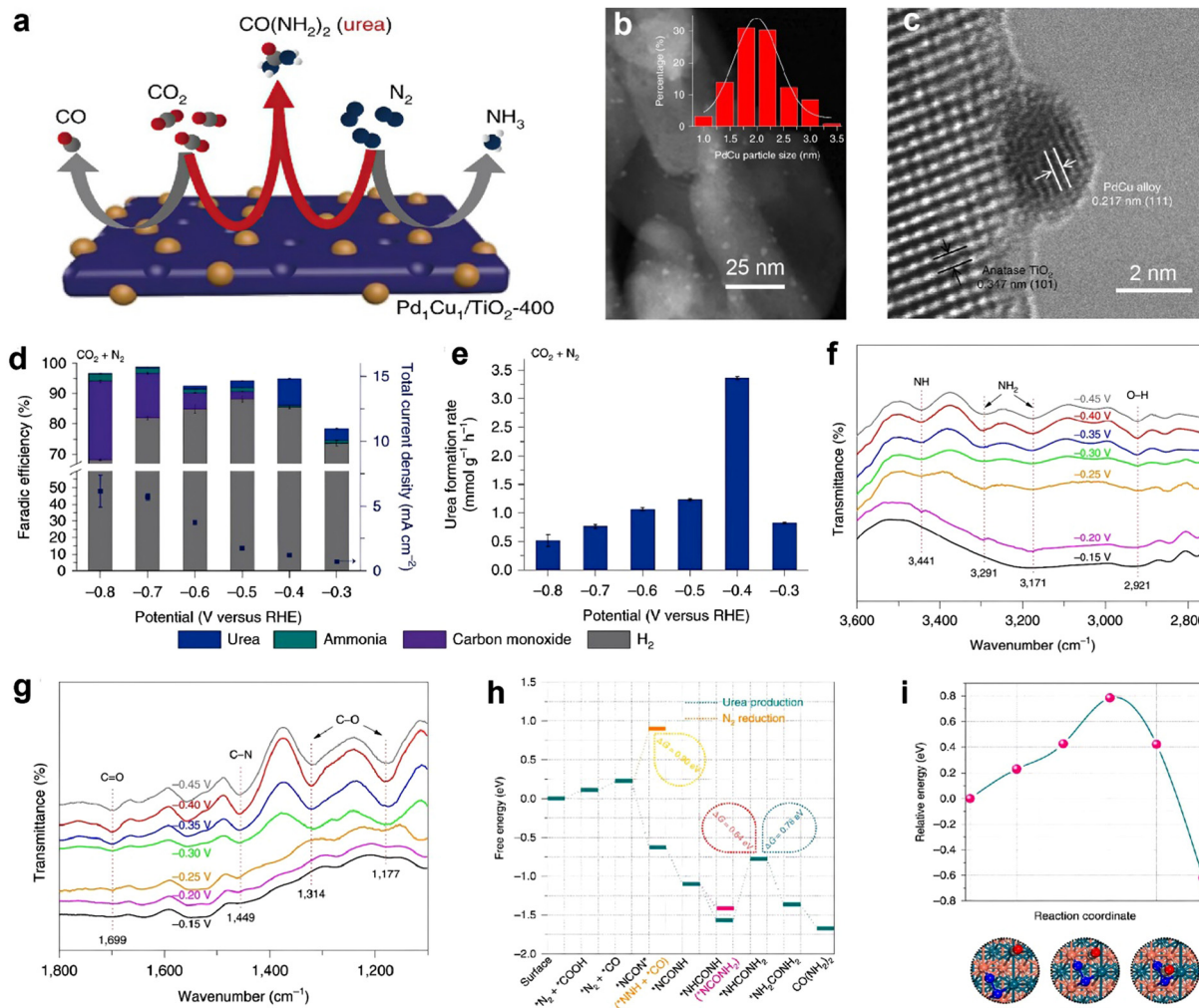


Fig. 10 Industrial process for the manufacture of urea. Reproduced with permission from ref. 255. Copyright 2019 and 2022, John Wiley & Sons, Inc.



**Fig. 11** (a) Schematic diagram for synthesis of urea over the  $\text{Pd}_1\text{Cu}_1/\text{TiO}_2$ -400 catalyst. (b) TEM image of  $\text{Pd}_1\text{Cu}_1/\text{TiO}_2$ -400; the inset shows the distribution of the  $\text{PdCu}$  nanoparticles. (c) High-resolution TEM image of the  $\text{Pd}_1\text{Cu}_1/\text{TiO}_2$ -400 catalyst. (d) FEs and total current densities for all products with  $\text{CO}_2$  and  $\text{N}_2$  as feeding gases. (e) Corresponding urea yield rate. Infrared signal in the range of (f) 2750–3600  $\text{cm}^{-1}$  and (g) 1100–800  $\text{cm}^{-1}$  under various potentials over the  $\text{Pd}_1\text{Cu}_1/\text{TiO}_2$ -400 catalyst during the electrocoupling of  $\text{N}_2$  and  $\text{CO}_2$ . (h) Free energy diagram of urea production. (i) Reaction pathway for the formation of  $^{*}\text{NCON}^{*}$ . Reproduced with permission from ref. 32. Copyright 2020, Springer Nature.

$\text{Pd}_1\text{Cu}_1/\text{TiO}_2$ -400 catalyst exhibited highly efficient urea electro-synthesis with a yield rate of  $3.36 \text{ mmol g}^{-1} \text{ h}^{-1}$  and FE of 8.92% at an applied potential of  $-0.4 \text{ V}$  vs. RHE in  $\text{N}_2$ - and  $\text{CO}_2$ -saturated 0.1 M  $\text{KHCO}_3$  aqueous solution (Fig. 11c and d).

The chemisorption of nitrogen gas is the first step in the electrocatalytic production of urea. In this study, the authors found that the nanocomposites showed an enhanced gas molecule adsorption capacity after hybridizing the  $\text{PdCu}$  alloy nanoparticles with oxygen vacancy-rich  $\text{TiO}_2$  nanosheets, and the adsorption capacity for  $\text{CO}_2$  molecules was also enhanced. More importantly, the shift in the corresponding peaks in the competitive adsorption reaction of  $\text{CO}_2$  and  $\text{N}_2$  was almost negligible, leading to high efficiency for urea electrosynthesis.

The intermediate products from the  $\text{Pd}_1\text{Cu}_1/\text{TiO}_2$ -400 catalyst in the co-reduction of  $\text{CO}_2$  and  $\text{N}_2$  to urea via the electrochemical C–N coupling reaction were determined by the advanced isotope-labeling operando synchrotron-radiation

Fourier transform infrared spectroscopy (SR-FTIR) technology (Fig. 11f and g).<sup>261</sup> As can be seen,  $\text{N}_2$  began to be activated to generate  $^{*}\text{NH}$  and  $^{*}\text{NH}_2$  intermediates at  $-0.2 \text{ V}$  vs. RHE. When the applied potential reached  $-0.25 \text{ V}$  vs. RHE,  $\text{CO}_2$  began to be activated to generate  $^{*}\text{C=O}$  and  $^{*}\text{C-O}$ . With a further increase in the potential to  $-0.3 \text{ V}$  vs. RHE, the C–N infrared vibration peak appeared, indicating that the C–N coupling reaction occurred to produce the target product of urea.

Using density functional theory (DFT) calculations, a detailed reaction mechanism for the formation of urea was comprehensively studied with the most stable geometric structures of the reactants, intermediates, and products (Fig. 11h and i). The analysis results revealed that it is thermodynamically and kinetically feasible for the generation of the  $^{*}\text{NCON}^{*}$  intermediate via the activation of the  $\text{N}_2$  molecule, as the key step for effective urea production. The presence of the  $^{*}\text{N}_2$  intermediate can facilitate  $\text{CO}_2$  reduction, and the reduced CO

can further react with  $*\text{N}_2$  to form urea with ultrahigh activity and selectivity. This coupling reaction occurs through C–N bond formation *via* the thermodynamically spontaneous reaction between  $*\text{N}=\text{N}^*$  and CO.

Although the aforementioned noble metal Pd-based catalysts can realize the electrosynthesis of urea, their electrocatalytic activity still needs to be improved. Besides, the high cost and scarcity of noble metals limit their large-scale applications. Therefore, it is highly desirable to develop earth-abundant

alternatives to further improve the urea electrosynthesis performance. In this regard, Zhang and co-workers proposed a Mott–Schottky heterostructure to improve the electrochemical performance of urea electrosynthesis.<sup>237</sup> As a proof-of-concept catalyst, a non-noble metal Bi–BiVO<sub>4</sub> was prepared *via* the NaBH<sub>4</sub> reduction strategy (Fig. 12a). It was demonstrated that a unique Mott–Schottky heterostructure can be formed by combining metallic Bi and semiconducting BiVO<sub>4</sub> (Fig. 12b) to allow spontaneous electron transfer from BiVO<sub>4</sub> to metallic

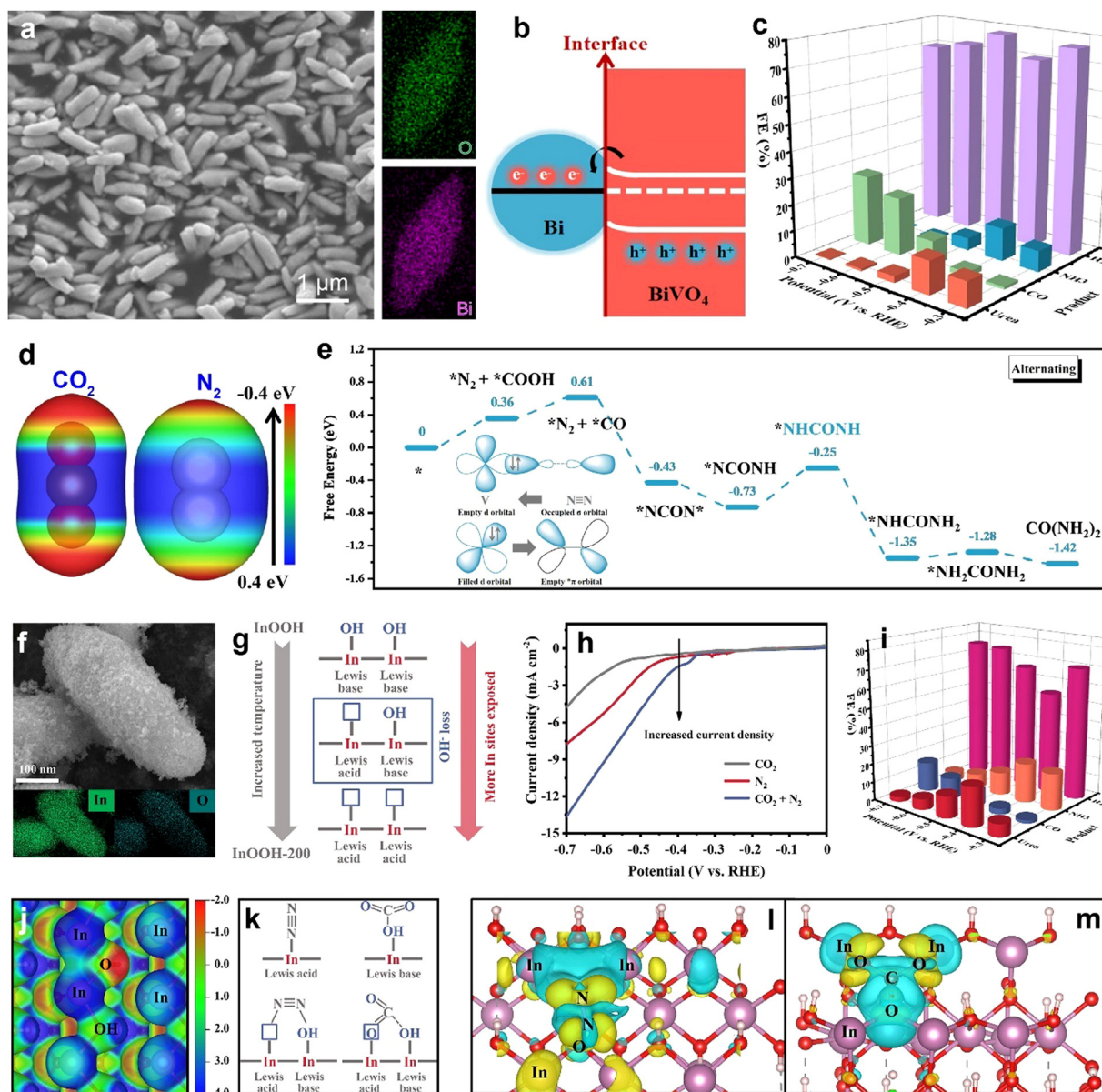


**Fig. 12** (a) SEM image and corresponding element mapping of the Bi–BiVO<sub>4</sub> catalyst. (b) Schematic illustration of the charge transfer process in Bi–BiVO<sub>4</sub>. (c) FEESR of different products with N<sub>2</sub> and CO<sub>2</sub> as the feeding gas at various potentials for Bi–BiVO<sub>4</sub>. (d) Electron density isosurface of CO<sub>2</sub> and N<sub>2</sub>, where the color bar represents the electrostatic potential scale. (e) Electrolytic urea production *via* the alternating mechanism and the inset is a simplified schematic of N<sub>2</sub> bonding to the V center. Reproduced with permission from ref. 237. Copyright 2021, John Wiley & Sons, Inc. (f) SEM image of the InOOH-100 catalyst and the corresponding EDX elemental mapping. (g) Schematic illustration of the formation of FLP sites affected by the calcination temperature. (h) LSV curves of InOOH-100 catalysts in various gas-saturated electrolytes. (i) FEESR of the different products with N<sub>2</sub> and CO<sub>2</sub> as the feeding gas over InOOH-100. (j) Electrostatic potential surface of InOOH (001). (k) Schematic illustration of N<sub>2</sub> and CO<sub>2</sub> adsorbed on various sites. (l and m) Charge density difference of (l) N<sub>2</sub> and (m) CO<sub>2</sub> adsorbed on the site of FLPs. Reproduced with permission from ref. 219. Copyright 2022, Elsevier.

Bi to form a unique space-charge region (Fig. 12b), ensuring the effective electrosynthesis of urea at different active sites.

In  $\text{N}_2$ - and  $\text{CO}_2$ -saturated 0.1 M  $\text{KHCO}_3$  electrolyte, the designed Bi– $\text{BiVO}_4$  catalyst delivered a remarkable urea production rate of  $5.91 \text{ mmol h}^{-1} \text{ g}^{-1}$  with a urea FE of 12.55% at  $-0.4 \text{ V vs. RHE}$  (Fig. 12c).<sup>237</sup> First-principles calculations were carried out to reveal the structure–function relationship. As shown in Fig. 12d, due to the electronic interaction, the electron-rich N atom in  $\text{N}_2$  and electron-deficient C atom in  $\text{CO}_2$  will adsorb on the electrophilic and nucleophilic regions, respectively, in the Bi– $\text{BiVO}_4$  catalyst. In the  $\text{VO}_4$  tetrahedron unit, the empty  $e_g$  orbitals of the V sites first accepted electrons from the occupied s orbitals of  $\text{N}_2$  molecules, and then the filled  $e_g$  orbitals of the V sites donate electrons to the  $\text{N}_2$  empty \* orbitals, effectively activating the  $\text{N}_2$  molecules on the surface of the Bi– $\text{BiVO}_4$  catalyst (Fig. 12d and e). Moreover,  $\text{N}_2$  and  $\text{CO}_2$  molecules were targeted for adsorption and activation on the nearby electrophilic and nucleophilic areas by the space-charge region at the heterointerface, which was caused by the self-driven charge transfer.<sup>262</sup> Besides, the proposed space-charge zone also improved the entire exposure of active sites and the thermodynamically viable electrochemical C–N coupling to form the required \* $\text{NCON}$ \* intermediate, which enhanced the electrocatalytic kinetics. (Fig. 12e).

Recently, Zhang and co-workers also fabricated a  $\text{BiFeO}_3/\text{BiVO}_4$ -based heterojunction and demonstrated a good electrocatalytic urea synthesis performance with a yield rate of  $4.94 \text{ mmol h}^{-1} \text{ g}^{-1}$  and urea FE of 17.18% at  $-0.4 \text{ V vs. RHE}$ .<sup>238</sup> Thus, the targeted adsorption and activation of  $\text{N}_2$  and  $\text{CO}_2$  molecules on the local electrophilic and nucleophilic regions in the  $\text{BiFeO}_3/\text{BiVO}_4$  catalyst were promoted, and this contributed to the observed good performance. The unique ability of the heterojunction structure to accelerate the local charge redistribution was primarily responsible for this.<sup>237,262</sup> This was motivated by the frustrated Lewis pairs (FLPs) composed of a Lewis acid (LA) and Lewis base (LB) for chemisorbing and reacting with various gas molecules.<sup>263–265</sup>

Zhang and co-workers<sup>219</sup> further developed FLPs in  $\text{InOOH-100}$  samples (Fig. 12f). In this catalyst, the unsaturated In sites and the neighboring surface-OH groups served as the LA and LB sites, respectively, which could be sterically prevented from bond formation and readily generate the artificial FLPs (Fig. 12g). The electrochemical tests showed that the current density in a mixed  $\text{CO}_2 + \text{N}_2$ -saturated electrolyte was significantly enhanced compared to the same electrolyte saturated with  $\text{CO}_2$  or  $\text{N}_2$  alone, suggesting the formation of urea (Fig. 12h). The products in the electrolyte after the chronoamperometry measurements were detected by ultraviolet-visible (UV-Vis) absorption spectroscopy. As shown in Fig. 12i, the  $\text{InOOH-100}$  catalyst delivered an excellent electrosynthesis performance for the production of urea. At the applied potential of  $-0.4 \text{ V vs. RHE}$ , the maximum yield rate of  $6.85 \text{ mmol h}^{-1} \text{ g}^{-1}$  and FE of 20.97% for the formation of urea were obtained. The electrostatic potential surface and Bader charge analysis showed that the Lewis acidic In sites ( $+0.93e$ ) and Lewis basic -OH group ( $-1.07e$ ) in the FLPs exhibited a positive and

negative electrostatic potential, respectively (Fig. 12j). Consequently, it was possible to readily selectively chemisorb the electron-rich N atom in  $\text{N}_2$  and the electron-deficient C atom in  $\text{CO}_2$  on the interfacial LB and LA sites, respectively. By taking advantage of the cooperative activation mechanism between sterically hindered hydroxyls and unsaturated In sites (Fig. 12k), the  $\text{InOOH-100}$  catalyst with enhanced artificial FLPs sites could readily adsorb  $\text{N}_2$  and  $\text{CO}_2$  molecules. Subsequently, the orbital-matched \* $\text{N}=\text{N}^*$  and \* $\text{CO}$  intermediates preferred to undergo the desired electrocatalytic C–N coupling reaction, benefiting from the synergistic activation effect of the FLPs *via* the unique donation–acceptance process (Fig. 12l and m). This research opens up a new way to investigate FLP-coupled electrocatalysts for  $\text{CO}_2$  and  $\text{N}_2$  fixation, in addition to highlighting the crucial role of artificial FLPs in the ambient electrosynthesis of urea.

In another study, Mukherjee *et al.* reported that electrocatalysts based on copper phthalocyanine nanotubes (CuPc NTs) with multiple active sites (such as metal center, pyridinic-N<sub>1</sub>, pyrrolic-N<sub>2</sub>, and pyrrolic-N<sub>3</sub>) exhibited a high urea yield of  $143.47 \mu\text{g h}^{-1} \text{ g}_{\text{cat}}^{-1}$  with a urea FE of 12.99% at  $-0.6 \text{ V vs. RHE}$  *via* co-reduction of  $\text{N}_2$  and  $\text{CO}_2$ .<sup>240</sup> Theoretical calculations suggested that the pyridinic-N<sub>1</sub> and center Cu sites were responsible for the formation of C–N bonds during the electrosynthesis of urea through the reduction of  $\text{N}_2$  to  $\text{NN}^*$  and  $\text{CO}_2$  to \* $\text{CO}$ , respectively.

Currently,  $\text{N}_2$  is mainly adopted as the N source for electrochemical C–N coupling reactions and great progress has been achieved. However, its inherent chemical inertia seriously limits its practical application. As described in the Introduction, the direct electrocatalytic C–N coupling *via*  $\text{CO}_2$  with  $\text{NO}$ ,  $\text{NO}_2^-$ ,  $\text{NO}_3^-$ , or  $\text{NH}_3$  into high-value organonitrogen compounds is a promising strategy from the standpoint of “turn waste into treasure” by driving it with renewable energy.

In 2017, Yoneyama *et al.* developed a  $\text{TiO}_2$ –Nafion nanocomposite for the electrochemical co-conversion of  $\text{CO}_2$  and  $\text{NO}_3^-$  to urea, probably formed by  $\text{CO}^*$  and  $\text{NH}_2^*$  intermediates generated *in situ*, respectively.<sup>226</sup> Recently, Yan and co-workers<sup>36</sup> realized highly selective urea production by electrochemically coupling  $\text{NO}_3^-$  with  $\text{CO}_2$  on  $\text{In(OH)}_3$  with well-defined single {100} facets ( $\text{In(OH)}_3$ -S) (Fig. 13a). The  $\text{In(OH)}_3$ -S catalyst exhibited a cube-like nanocrystal morphology with particle sizes of 100–200 nm (inset in Fig. 13b), which was synthesized *via* a facile solvothermal method.<sup>266</sup> For the electrosynthesis of urea, 0.1 M  $\text{KNO}_3$  saturated with  $\text{CO}_2$  was used as the electrolyte. As shown in the LSV curves (Fig. 13b),  $\text{CO}_2$  significantly suppressed the HER to promote the  $\text{NO}_3^-$  reduction reaction (Fig. 13b). The amount of urea produced was quantitatively determined by the diacetyl monoxime method.<sup>258</sup> As expected, a urea yield rate of  $533.1 \mu\text{g h}^{-1} \text{ mg}_{\text{cat}}^{-1}$  at  $-0.6 \text{ V vs. RHE}$  with a urea FE of 53.4% was achieved for the  $\text{In(OH)}_3$ -S catalyst (Fig. 13c). The catalytic chemistry depends strongly on the type of the semiconductor catalyst used.<sup>267</sup> As shown in Fig. 13d, the  $\text{CO}_2$ -induced hole accumulation can shift the  $\text{In(OH)}_3$ -S semiconductor from n-type to

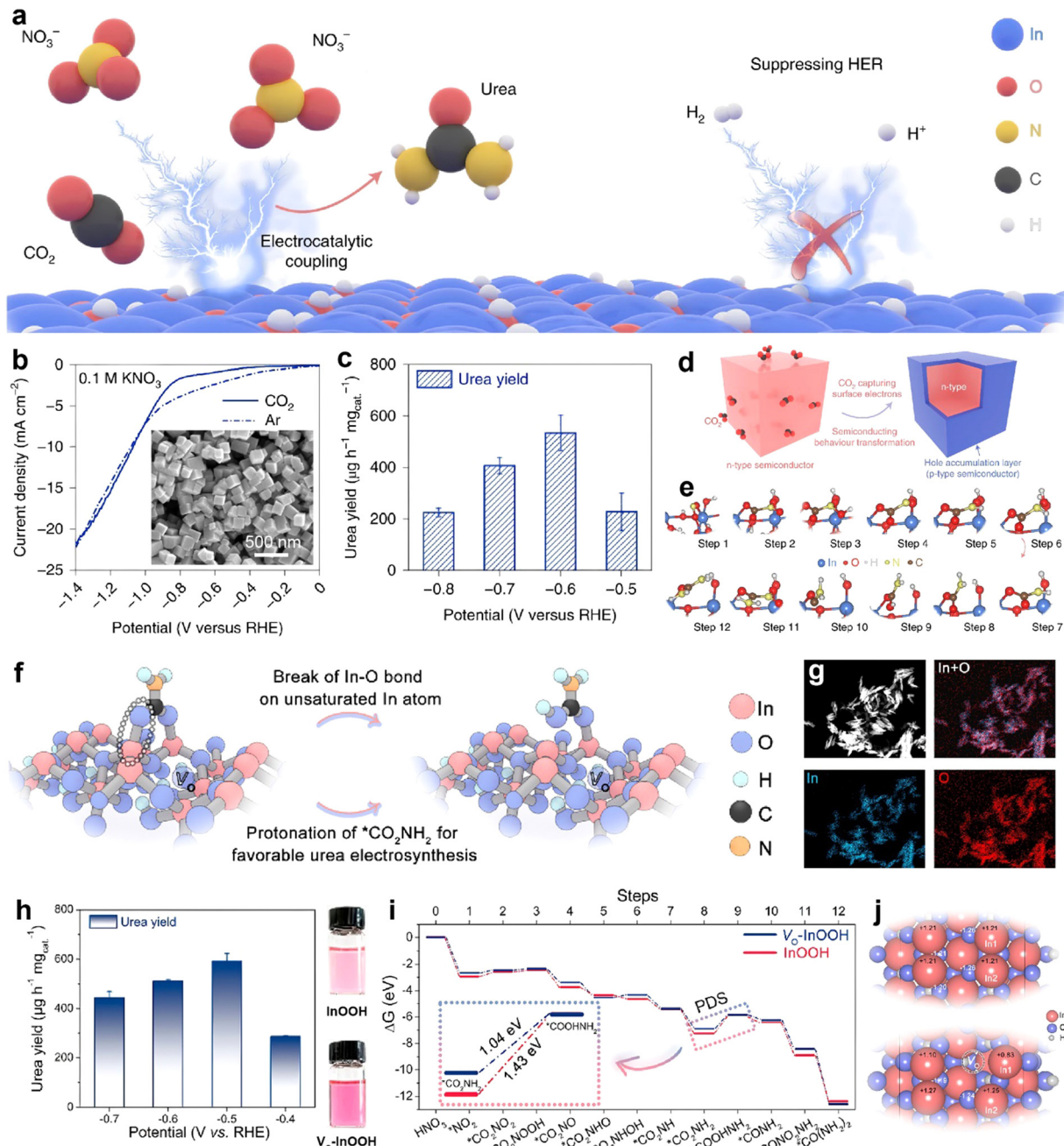


**Fig. 13** (a) Illustration of urea synthesis process on the surface of In(OH)<sub>3</sub>-S. (b) LSV curves in 0.1 M KNO<sub>3</sub> electrolyte with Ar or CO<sub>2</sub> feeding gas and SEM image of In(OH)<sub>3</sub>-S. (c) Urea yields at different potentials over In(OH)<sub>3</sub>-S in 0.1 M KNO<sub>3</sub> electrolyte with CO<sub>2</sub> feeding gas. (d) Schematic illustration of the n-p transformation process. (e) Atomic configurations for each step of urea production on In(OH)<sub>3</sub>-S. Reproduced with permission from ref. 36. Copyright 2021, Springer Nature. (f) Illustration of the preparation of V<sub>0</sub>-InOOH and urea electrosynthesis processes. (g) HAADF-STEM image and the corresponding EDX elemental mapping. (h) Urea yields over V<sub>0</sub>-InOOH at various applied potentials, and the urea comparison between V<sub>0</sub>-InOOH and InOOH at -0.5 V vs. RHE. (i) Free-energy diagrams for urea production at 0 V versus RHE. (j) Bader charge analysis on various catalysts. Reproduced with permission from ref. 229. Copyright 2022, the American Chemical Society.

p-type to repel protons from approaching In(OH)<sub>3</sub>-S, hence impeding the occurrence of the HER. The capture of surface electrons will be difficult for bicarbonate due to its electro-negative nature, leading to lower FEs for urea production in the electrolyte without feeding CO<sub>2</sub> gas. Moreover, theoretical calculations revealed that the {100} facets in In(OH)<sub>3</sub>-S can

favor direct C–N coupling *via* the reaction between the \*NO<sub>2</sub> and \*CO<sub>2</sub> intermediates. The early direct coupling of the \*NO<sub>2</sub> and \*CO<sub>2</sub> intermediates favors the {100} facets over the {110} facets (Fig. 13e), which results in the facet-dependent activity of In(OH)<sub>3</sub>. The higher selectivity of the direct coupling of \*NO<sub>2</sub> and \*CO<sub>2</sub> was possible due to the reduced energy barrier, which

is in contrast with the protonation of each gas individually (Fig. 13e).

Similarly, Yan *et al.* (Fig. 13f) developed a highly-efficient catalyst for the electrosynthesis of urea using  $\text{CO}_2$  and  $\text{NO}_3^-$  as sources using defect-engineered InOOH with oxygen vacancies ( $\text{V}_{\text{O}}\text{-InOOH}$ ).<sup>229</sup> The prepared  $\text{V}_{\text{O}}\text{-InOOH}$  had a rod-like nanosstructure with a length of  $\sim 100$  nm and width of  $\sim 20$  nm (Fig. 13g). The obtained  $\text{V}_{\text{O}}\text{-InOOH}$  exhibited a urea yield rate of up to  $592.5 \mu\text{g h}^{-1} \text{mg}_{\text{cat.}}^{-1}$  with a urea FE of 51.0% (Fig. 13h), surpassing that of the pristine InOOH catalyst. Combining operando synchrotron radiation-Fourier transform infrared spectroscopy and theoretical calculations, it was revealed that the potential-determining step for the electrosynthesis of urea was  $^*\text{CO}_2\text{NH}_2$  protonation (Fig. 13i). The oxygen vacancy reconfigured the surface electronic structure of the In active sites, and thus high catalytic activity by lowering the electro-positivity of In1 and energy barrier for the conversion of  $^*\text{CO}_2\text{NH}_2$  into  $^*\text{COOHNH}_2$  (Fig. 13j).<sup>268,269</sup>

Recently, Wang and co-workers also reported the electrosynthesis of urea by coupling  $\text{CO}_2$  with  $\text{NO}_3^-$ .<sup>228,233</sup> For instance, they developed oxygen vacancy-enriched  $\text{CeO}_2$  nanorods with an average length of 100 nm ( $\text{V}_{\text{O}}\text{-CeO}_2\text{-750}$ ) for electrosynthesis of urea under ambient conditions (Fig. 14a).<sup>233</sup> As shown in Fig. 14b, the electrochemical tests demonstrated that the production of urea over the resultant catalyst was directly related to the oxygen vacancy concentration with a maximum yield rate of  $943.6 \text{ mg h}^{-1} \text{ g}^{-1}$  at  $-1.6 \text{ V vs. RHE}$ , which was much higher than that for the oxygen-vacancy-deficient  $\text{CeO}_2$ . Combined *in situ* sum frequency generation (SFG) spectroscopy and DFT calculations revealed that the oxygen vacancy in the  $\text{CeO}_2$  nanorods could form coordination unsaturated sites to enhance the adsorption of the reaction species and stabilize the intermediate species (*i.e.*,  $^*\text{OCNO}$ ), which can serve as the descriptor to describe the oxygen vacancy-mediated selective coupling mechanism (Fig. 14e and d). Specifically, the energy barriers for four C–N coupling modes ( $^*\text{ON-CO}$ ,  $^*\text{NH}_2\text{-CO}$ ,  $^*\text{NH-CO}$ , and  $^*\text{N-CO}$ ) on the surface of  $\text{CeO}_2$  rich with oxygen vacancies and deficient in oxygen vacancies were first calculated. Compared with the protonation energy barriers of the four N-containing intermediates ( $^*\text{NO}$ ,  $^*\text{NH}_2$ ,  $^*\text{NH}$ , and  $^*\text{N}$ ), it was proposed that the C–N coupling reaction was more likely to occur on the surface of the oxygen vacancy-rich  $\text{CeO}_2$  through the formation of the  $^*\text{ONCO}$  intermediate. However, the selectivity for the C–N coupling or protonation reaction was relatively poor on both surfaces of  $\text{CeO}_2$  and  $\text{CeO}_2$  deficient in oxygen vacancies. The use of the  $^*\text{OCNO}$  intermediate species as a descriptor to identify the selective coupling mechanism mediated by oxygen vacancies was supported by *in situ* SFG spectroscopy, which confirmed that the oxygen vacancies promoted the  $^*\text{NO}$  intermediate species to form the key intermediate  $^*\text{OCNO}$  species for the efficient electrosynthesis of urea (Fig. 14e and d).

Moreover, Wang *et al.* also reported the preparation of a diatomic electrocatalyst with bonded Fe–Ni pairs (B-FeNi-DASC), which could significantly improve the performance of urea electrosynthesis *via* coordinated adsorption and activation

of multiple reactants (Fig. 14f and g).<sup>228</sup> By contrast, the selective adsorption and activation of  $\text{CO}_2$  or  $\text{NO}_3^-$  unilaterally were not constrained in the diatomic Fe–Ni (I-FeNi-DASC) electrocatalyst. Numerous C- and N-species were activated by the isolated Fe–N<sub>4</sub> and Ni–N<sub>4</sub> sites in I-FeNi-DASC, which also boosted the probability of connecting these intermediates to produce the vital C–N bonds. Moreover, the bridge sites of the Fe–Ni pairs (FeNi–N<sub>6</sub>) in B-FeNi-DASC were most effective for urea formation due to the intrinsically thermodynamic and kinetic favorable C–N coupling process, leading to a high urea yield rate of  $20.2 \text{ mmol h}^{-1} \text{ g}^{-1}$  and maximum urea FE of 17.8% (Fig. 14h). Based on operando synchrotron-radiation Fourier transform infrared spectroscopy (SR-FTIR) measurements (Fig. 14i) and first-principles calculations (Fig. 14j and k), it was concluded that the electrochemical production of urea on the B-FeNi-DASC catalyst mainly originated from the coupling of  $^*\text{NH}$  with  $^*\text{CO}$  intermediates to form the first C–N bond and the subsequent C–N coupling between the newly-formed  $^*\text{NHCO}$  and  $^*\text{NO}$  intermediates to form the second C–N bond, which was thermodynamic spontaneous and highly kinetically feasible on the bonded Fe–Ni pair sites with low energy barriers of 0.21 and 0.09 eV, respectively. These results present new insights into identifying and tailoring activation sites for the enhanced selective C–N coupling process *via* intermediate stabilization and mechanistic understanding of the electrocatalytic urea synthesis. This greatly promotes the green synthesis of urea *via* the electrochemical C–N coupling reaction under ambient conditions.

The electrosynthesis of urea *via* the co-reduction of  $\text{CO}_2$  and  $\text{NO}_2^-$  was first reported by Shibata *et al.* in 1995.<sup>243</sup> By applying a gas-diffusion electrode, urea was generated over a Cu-based catalyst with an FE of 37% at an applied potential of  $-0.75 \text{ V vs. SHE}$  in  $0.02 \text{ M KNO}_2$  aqueous solution. Recently, Huang and co-workers<sup>35</sup> enriched the electrochemical synthesis strategy of urea by co-reducing  $\text{CO}_2$  and  $\text{NO}_2^-$  (Fig. 15a) on a Te-doped Pd nanocrystal (Te-Pd NCs) catalyst with an average diameter of 20 nm (Fig. 15b). The nanocrystal exhibited a high urea FE of about 12.2% for the formation of urea in  $\text{CO}_2$ -saturated  $0.1 \text{ M KHCO}_3 + 0.01 \text{ M KNO}_2$  solution as the electrolyte in an H-cell (Fig. 15c), which was much higher than that for the pristine Pd nanocrystal. The mechanism studies showed that the doping of the Te atom not only optimizes  $\text{CO}_2/\text{CO}$  adsorption but also promotes  $\text{NH}_3$  production for the formation of urea. It has been demonstrated that  $\text{CO}_2$  and  $\text{NO}_2^-$  can be first reduced into  $^*\text{CO}$  and  $^*\text{NH}_2$  intermediates, respectively, and then further converted into urea (Fig. 15d), as confirmed by the calculated energy barriers for  $^*\text{CONH}_2$  formation (Te-Pd(111):  $-0.49 \text{ eV}$  and Pd:  $0.61 \text{ eV}$ ) (Fig. 15e) and also supported by another study.<sup>270</sup>

The synergistic effect of Te and Pd species in the Te-Pd NCs significantly promoted the electrocatalytic conversion of  $\text{CO}_2$  to  $^*\text{CO}$  and  $\text{NO}_2^-$  to  $^*\text{NH}_2$  for the subsequent formation of urea *via* a C–N coupling reaction. More importantly, on the Te-Pd NC catalyst, the competitive reaction (*i.e.*, the formation of  $\text{N}_2$  through the electroreduction of  $\text{NO}_2^-$  over the Pd NCs) was effectively inhibited. Therefore, the FE and conversion

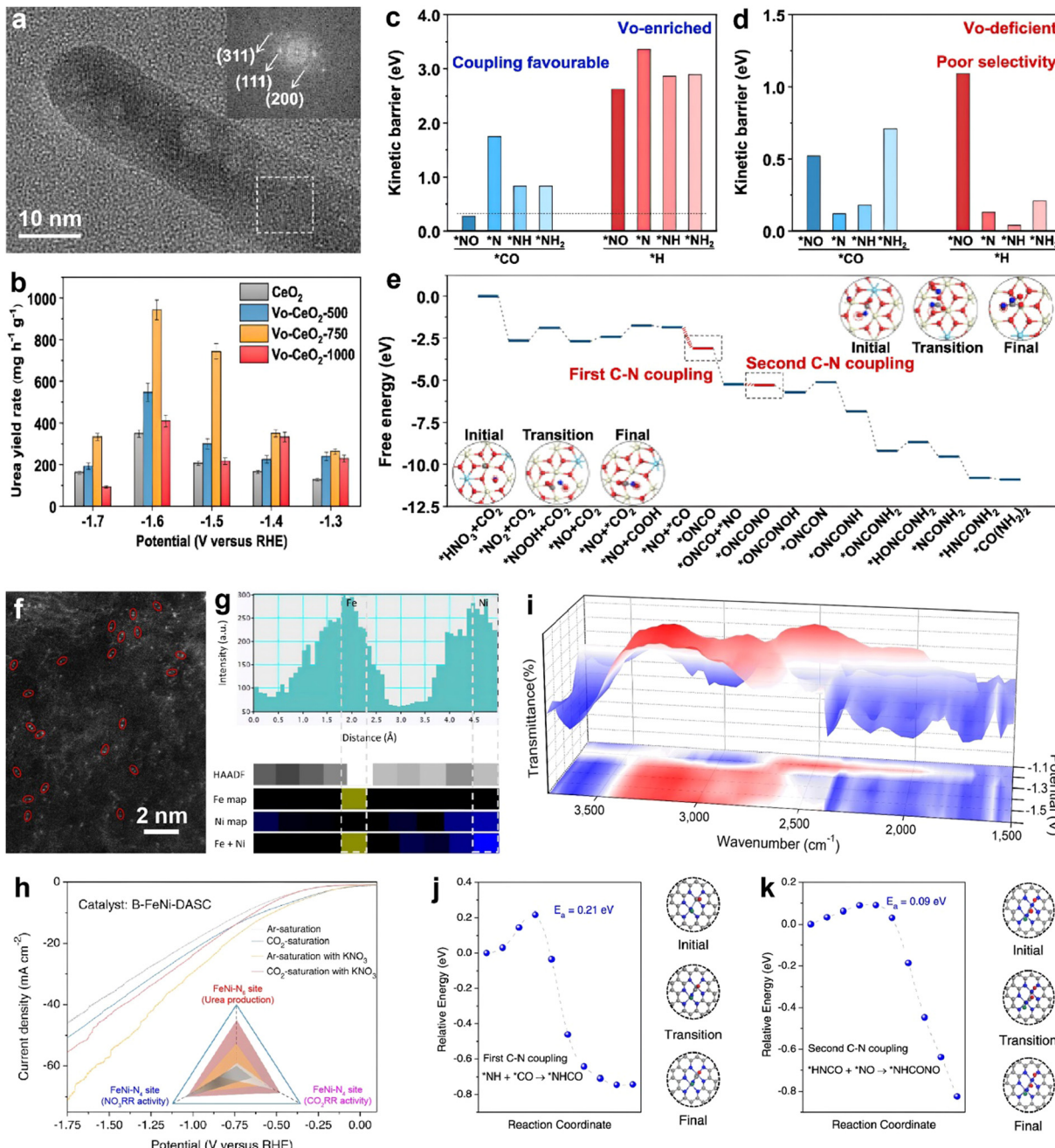


**Fig. 14** (a) TEM image of the Vo-CeO<sub>2</sub>-500 catalyst, and the inset is the corresponding selected area electron diffraction pattern. (b) Urea yield rates of the catalysts at various applied potentials. Comparison of the coupling energy barriers of the \*NO, \*N, \*NH, and \*NH<sub>2</sub> intermediates with \*CO and protonation on (c) Vo-enriched CeO<sub>2</sub> and (d) Vo-deficient CeO<sub>2</sub> catalysts. (e) Free energy diagram of electroynthesis of urea on the Vo-enriched CeO<sub>2</sub> catalyst. Reproduced with permission from ref. 233. Copyright 2022, the American Chemical Society. (f) Aberration-corrected HAADF-STEM image of the B-FeNi-DASC catalyst. (g) Acquired HAADF-STEM image intensity profile accompanied by atomic-resolution EELS mapping of the Fe–Ni pair. (h) LSV curves over the BFeNi-DASC catalyst, and the inset is the illustrated correlation between CO<sub>2</sub>RR activity, NO<sub>3</sub>RR activity, and urea production over various site configurations. (i) 3D operando SR-FTIR spectra. Reaction pathway of (j) first and (k) second C–N coupling reaction for the formation of \*NHCO and \*NHCONO intermediates, respectively. The structures of the initial, transition and final states together with the formation of \*NHCO and \*NHCONO as insets, respectively. Reproduced with permission from ref. 228. Copyright 2022, Springer Nature.

efficiency of the N atom to urea on the Te–Pd NCs were much higher than that on the pure Pd NCs.

Furthermore, Zhang's group<sup>223</sup> also prepared a self-supported ZnO porous nanosheet with abundant oxygen

vacancies (ZnO-V) on carbon cloth for the electroynthesis of urea by co-reducing CO<sub>2</sub> and NO<sub>3</sub><sup>−</sup> (Fig. 15f–h). In 0.2 M NaHCO<sub>3</sub> + 0.1 M NaNO<sub>2</sub> electrolyte, the formation of urea over the ZnO-V catalyst was detected at −0.49 V vs. RHE.

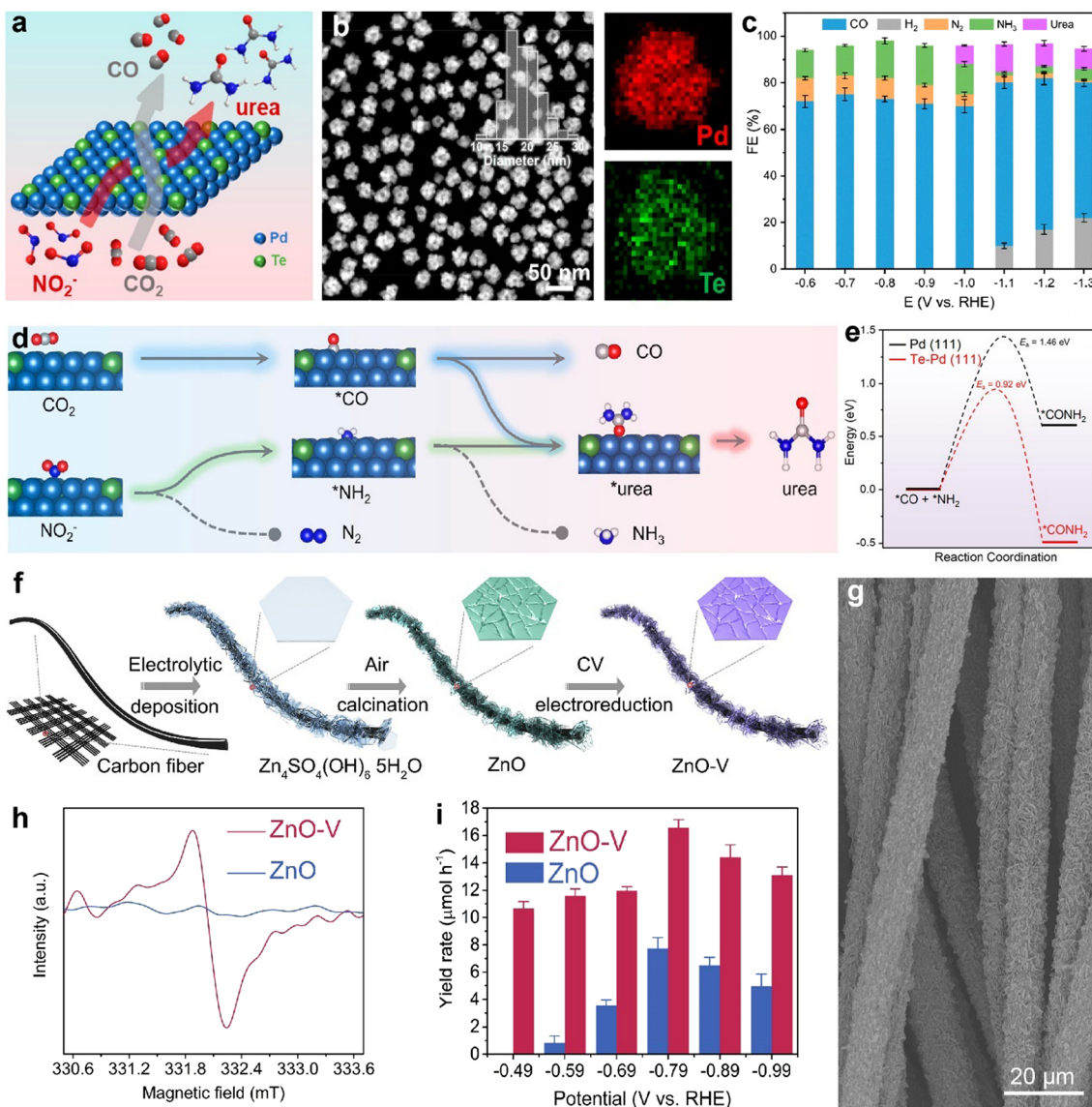


**Fig. 15** (a) Schematic depicting the formation of urea from the simultaneous electroreduction of  $\text{CO}_2$  and  $\text{NO}_2^-$ . (b) HAADF-STEM image, corresponding diameter histogram, and EDX elemental mappings of the Te–Pd NCs. (c) FE versus the applied potential for the electrosynthesis of urea over the Te–Pd NC catalyst. (d) Scheme of the synthesis of urea from  $\text{CO}_2$  and  $\text{NO}_2^-$  on Te–Pd NCs. (e) Free-energy diagram and activation barriers for the formation of \*CONH<sub>2</sub> on the surface of different catalysts. Reproduced with permission from ref. 35. Copyright 2021, the American Chemical Society. (f) Schematic illustration of the synthesis of ZnO–V porous nanosheets. (g) SEM image of ZnO–V. (h) EPR of ZnO and ZnO–V porous nanosheets. (i) Urea yield rates under various potentials over ZnO–V. Reproduced with permission from ref. 223. Copyright 2021, Elsevier.

Simultaneously, the FE of urea over the ZnO–V catalyst increased with a decrease in the potential from  $-0.49$  to  $-0.79$  V vs. RHE and reached the maximum of  $23.26\%$  (Fig. 15i), which was much higher than the maximum of the pristine ZnO ( $8.10\%$ ). By decreasing the applied potential, the FE of urea decreased mainly due to the enhanced formation of by-products (e.g.,  $\text{H}_2$ ,  $\text{CO}$ , and  $\text{NO}$ ). The maximum production rate of urea for ZnO–V reached  $16.56 \text{ mmol h}^{-1}$  at the applied potential of  $-0.79$  V (Fig. 15i), which is remarkably higher than that of the pristine ZnO ( $7.72 \text{ mmol h}^{-1}$ ). A possible coupling pathway for the  $\text{NH}_2^*$  and  $\text{COOH}^*$  intermediates for the formation of urea was revealed by the analysis of the results of

*in situ* diffuse reflectance infrared Fourier transform spectroscopy and online differential electrochemical mass spectrometry (DEMS).

For the electrosynthesis of urea using  $\text{CO}_2$  and  $\text{NO}_2^-$  as carbon and nitrogen sources, respectively, Wang's group presented an ultrathin AuCu nanowire with a Boerdijk–Coxeter structure of (111)-dominant facets (Fig. 16a–c).<sup>224</sup> The bimetallic AuCu alloy composition, coupled with the rich structural defects, provided a large number of highly catalytically active sites (Fig. 16a). Consequently, the resultant electrocatalyst displayed an excellent urea synthesis performance in  $\text{CO}_2$ -saturated  $0.5 \text{ M } \text{KHCO}_3 + 0.01 \text{ M } \text{KNO}_2$  solution with a yield

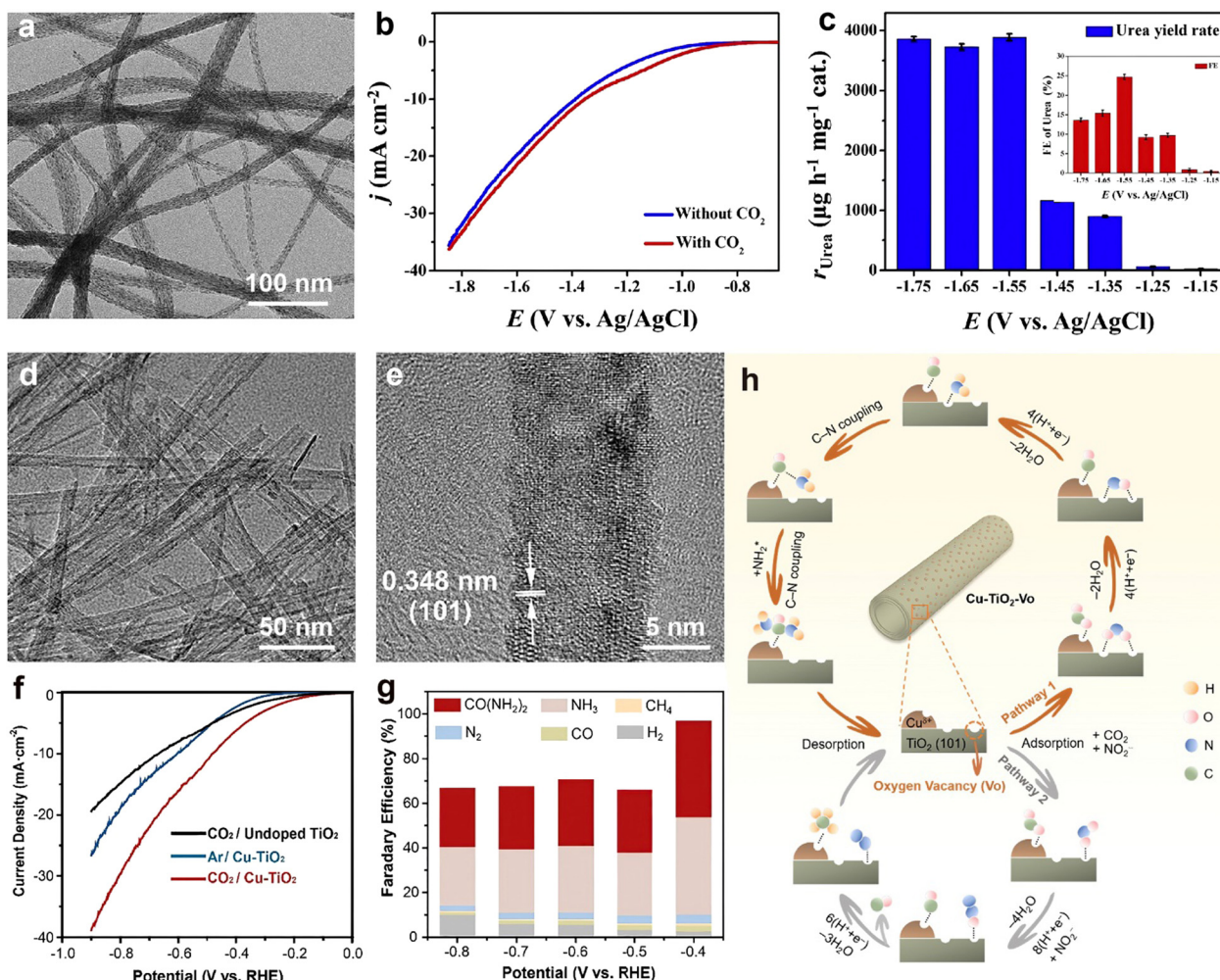


**Fig. 16** (a) TEM image of the AuCu SANF catalyst. (b) LSV curves of the AuCu SANF catalyst in 0.5 M KHCO<sub>3</sub> electrolyte containing 0.01 M KNO<sub>3</sub> saturated with or without CO<sub>2</sub>. (c) Urea yield rate over the AuCu SANF catalyst at various potentials, and the inset is the corresponding FEs. Reproduced with permission from ref. 224. Copyright 2022, Elsevier. TEM image of (d) TiO<sub>2</sub> and (e) Cu-TiO<sub>2</sub>. (f) LSV curves of the catalysts in 0.2 M KHCO<sub>3</sub> + 0.02 M KNO<sub>3</sub> aqueous solution saturated with CO<sub>2</sub> or Ar. (g) FEs of the products over the Cu-TiO<sub>2</sub> catalyst. (h) Possible mechanisms for the synthesis of urea and other by-products for the co-reduction of CO<sub>2</sub> and NO<sub>2</sub> over the Cu-TiO<sub>2</sub> catalyst. Reproduced with permission from ref. 34. Copyright 2020, Elsevier.

rate as high as 3889.6  $\mu\text{g h}^{-1} \text{mg}_{\text{cat}}^{-1}$  and FE of 24.7% at  $-1.55$  V vs. Ag/AgCl (Fig. 16b and c). The excellent urea synthesis activity and stability observed for the AuCu alloy nanowires are attributed to the unique combination of the fibrous 1D nanowire structure and the AuCu bimetallic composition.

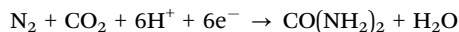
In addition, Ranjendran *et al.* reported the use of Fe-doped TiO<sub>2</sub> electrodes for the electrocatalytic synthesis of urea in CO<sub>2</sub>-saturated NaHCO<sub>3</sub> and KNO<sub>3</sub> solutions but did not quantify the urea yield.<sup>271</sup> Zheng *et al.* demonstrated that Cu-TiO<sub>2</sub> with high oxygen vacancies could produce urea at an exceptional rate of 20.8  $\mu\text{mol h}^{-1}$  and FE of 43.1% at the applied potential of  $-0.4$  V vs. RHE for Cu-TiO<sub>2</sub> rich with oxygen vacancies (Fig. 16d-h), which are substantially superior to the pristine TiO<sub>2</sub>.<sup>34</sup> First-principles calculations showed that the low-valence Cu dopants induced rich oxygen vacancies due to their distinct d-electron properties, which are beneficial for exposing

the bi-Ti<sup>3+</sup> active sites. The efficient electrocatalytic activity resulted from the synergistic effect of the bi-Ti<sup>3+</sup> pairs and poorly coordinated Cu ions. Urea was produced from CO<sub>2</sub> and NO<sub>2</sub> by the electrochemical C-N coupling reaction between the CO\* species produced by the ECRR on the undercoordinated Cu sites and the NH<sub>2</sub>\* precursor produced by the electrochemical NO<sub>2</sub><sup>-</sup> reduction reaction on the bi-Ti<sup>3+</sup> active sites (Fig. 16h).

Using NO as a nitrogen source, Zhang's group prepared Zn nanobelts (Zn NBs) *via* the *in situ* electrochemical reduction of the ZnO nanosheet precursor for the electroreduction of NO.<sup>272</sup> Over the Zn NBs catalyst, the yield rate and FE of urea reached up to 15.13 mmol g $^{-1}$  h $^{-1}$  and 11.26%, respectively, at a current density of 40 mA cm $^{-2}$  in a flow cell electrolyzer. Combined *in situ* experiments and theoretical calculations revealed that urea was formed through a ten-step cascade reaction process, in which the C-N bonds were formed through the step-by-step coupling of \*CO with \*NH<sub>2</sub> intermediates.

Compared with the huge energy consumption industrial processes, urea electrosynthesis driven by renewable electricity provides an appealing route due to its mild conditions. As summarized in this section, various nitrogen sources have been explored as green and sustainable strategies for the electro-synthesis of urea by coupling CO<sub>2</sub>. Among them, the electro-synthesis of urea from the co-activation of N<sub>2</sub> and CO<sub>2</sub> has emerged as an attractive energy-saving route due to the abundance of N<sub>2</sub>. Nonetheless, the electrosynthesis of urea utilizing N<sub>2</sub> as an N source still suffers from extremely low selectivity and reactivity as a result of the intrinsic chemical inertness and the low solubility of N<sub>2</sub> as well as the high dissociation energy of the N≡N triple bond. Therefore, electrocatalytic urea synthesis by adopting reactive nitrogen contaminants as a nitrogen source to couple with CO<sub>2</sub> is a win-win strategy from the perspectives of saving energy and protecting the environment.

Although CO<sub>2</sub> and oxynitride (NO<sub>2</sub><sup>-</sup>, NO<sub>3</sub><sup>-</sup>, NO, etc.) as sources of C and C–N coupling reactions for the electrosynthesis of urea have significant advantages over N<sub>2</sub>, they also have some disadvantages. For example, due to the fact that NO<sub>2</sub><sup>-</sup> is easier to reduce than NO<sub>3</sub><sup>-</sup>, it has mostly been used as the N source for electrochemical C–N coupling reactions. From an application standpoint, the electrocatalytic coupling of NO<sub>3</sub><sup>-</sup> with CO<sub>2</sub> to produce the value-added urea is appealing given that NO<sub>2</sub><sup>-</sup> is unstable and inclined to form NO<sub>3</sub><sup>-</sup> in aqueous solution.<sup>30,31,273,274</sup> Additionally, the electrocatalytic synthesis of urea involves multistep electrochemical processes (proton-coupling electron-transfer) and chemical steps (C–N coupling), in which the whole reaction to form urea from N<sub>2</sub> requires more electrons and protons than that of oxynitride (NO<sub>2</sub><sup>-</sup>, NO<sub>3</sub><sup>-</sup>, NO, etc.) as follows:



The multiphoton-coupled multielectron-transfer process reduces the thermodynamics and kinetics of the electrochemical C–N coupling reaction, and thus the selective hydrogenation of the intermediate species to by-products rather than the occurrence of C–N coupling hinders the efficient electrosynthesis of urea. In any case, urea electrosynthesis technology *via* the electrochemical C–N coupling reaction still suffers from low selectivity and low reactivity. To date, the key to this technique is the design and exploration of low-cost, high-efficient, and stable electrocatalysts.

## 6.2. Acetamide

Acetamide (CH<sub>3</sub>CONH<sub>2</sub>) is the simplest amide derived from acetic acid. It is a colorless and transparent needle-like crystal, with the scent of mouse secretions and is easy to deliquesce, which is mainly used as an analytical reagent, industrial

solvent, stabilizer, and plasticizer as well as in organic synthesis, the pharmaceutical sector, and dye industry. Acetamide can be viewed as an intermediate between acetone with two methyls (-CH<sub>3</sub>) on either side of the carbonyl (-CO) and urea with two amide (-NH<sub>2</sub>) groups at these positions. Acetamide is synthesized by the reaction of glacial acetic acid and liquid ammonia to generate ammonium acetate (CH<sub>3</sub>COONH<sub>4</sub>), followed by pyrolysis dehydration (CH<sub>3</sub>COONH<sub>4</sub> → CH<sub>3</sub>CONH<sub>2</sub> + H<sub>2</sub>O), crystallization, and separation. It can also be produced by the hydration of acetonitrile (CH<sub>3</sub>CN + H<sub>2</sub>O → CH<sub>3</sub>CONH<sub>2</sub>) as a by-product of acrylonitrile production.

In an early study, Jiao and co-workers creatively introduced NH<sub>3</sub> as a nitrogen source to realize the C–N coupling reaction,<sup>31</sup> demonstrating the construction of carbon–heteroatom bonds in CO<sub>2</sub>/CO electrolysis. Over highly crystalline metallic Cu NPs with an average particle size of 50 ± 20 nm and a small fraction of Cu oxides (Fig. 17a), the C–N bonds could be formed through the co-electrolysis of CO and NH<sub>3</sub> with an acetamide selectivity of nearly 40% in KOH aqueous solution in a three-compartment continuous flow cell. It was shown that \*(HO)C=COH was also hydrolyzed to \*C=C=O, which in turn reacted with NH<sub>3</sub> to form certain intermediates that proceed to form acetamide, while suppressing the formation of other C<sub>2+</sub> products. Moreover, this work extended the range of C–N-containing products to include *N*-methylacetamide (C<sub>3</sub>H<sub>7</sub>NO), *N*-ethylacetamide (C<sub>4</sub>H<sub>9</sub>NO), *N,N*-dimethylacetamide (C<sub>4</sub>H<sub>9</sub>NO), and acetic monoethanolamide (C<sub>4</sub>H<sub>9</sub>NO<sub>2</sub>).

In a typical experiment, galvanostatic electrolysis was performed in 1.0 M KOH solution to test the electroreduction activity of CO. When pure CO gas was introduced in the reaction vessel, a nearly exponential polarization response was observed, and C<sub>2+</sub> products accounted for up to 80% of the total products. The main C<sub>2+</sub> products from the CO electro-reduction were identified to be ethylene, ethanol, acetate, and *n*-propanol.

Depending on the CO electrolysis activity, an NH<sub>3</sub> and CO mixture gas in a molar ratio of 1 : 2 was fed into the flow cell. In the presence of NH<sub>3</sub>, the potential required to reach the same current density increased by ~30 mV compared with that for pure CO, which is probably due to the reduced CO partial pressure in the test system.<sup>275,276</sup> Remarkably, the presence of NH<sub>3</sub> led to the considerable production of acetamide with a high FE of 38% and a partial current density of 114 mA cm<sup>-2</sup> at -0.68 V *vs.* RHE (Fig. 17b and c). The catalytic selectivity switched toward the pure CO reduction products as the proportion of CO in the gas input increased, while the selectivity for acetamide was unaffected by increasing the ratio of NH<sub>3</sub> beyond 2 : 1.

Full-solvent quantum mechanical calculations were applied to study the mechanism of electrocatalytic production of acetamide in the presence of NH<sub>3</sub> (Fig. 17d). By using \*(HO)C=COH as the starting state, it was found that the free energy barrier for the formation of the \*C=C=O intermediate *via* the water-mediated pathway was 0.57 eV. As reported, \*C=C=O was proposed as an intermediate in the pathway for the formation of C<sub>2</sub>H<sub>4</sub>.<sup>277</sup> However, later full-solvent

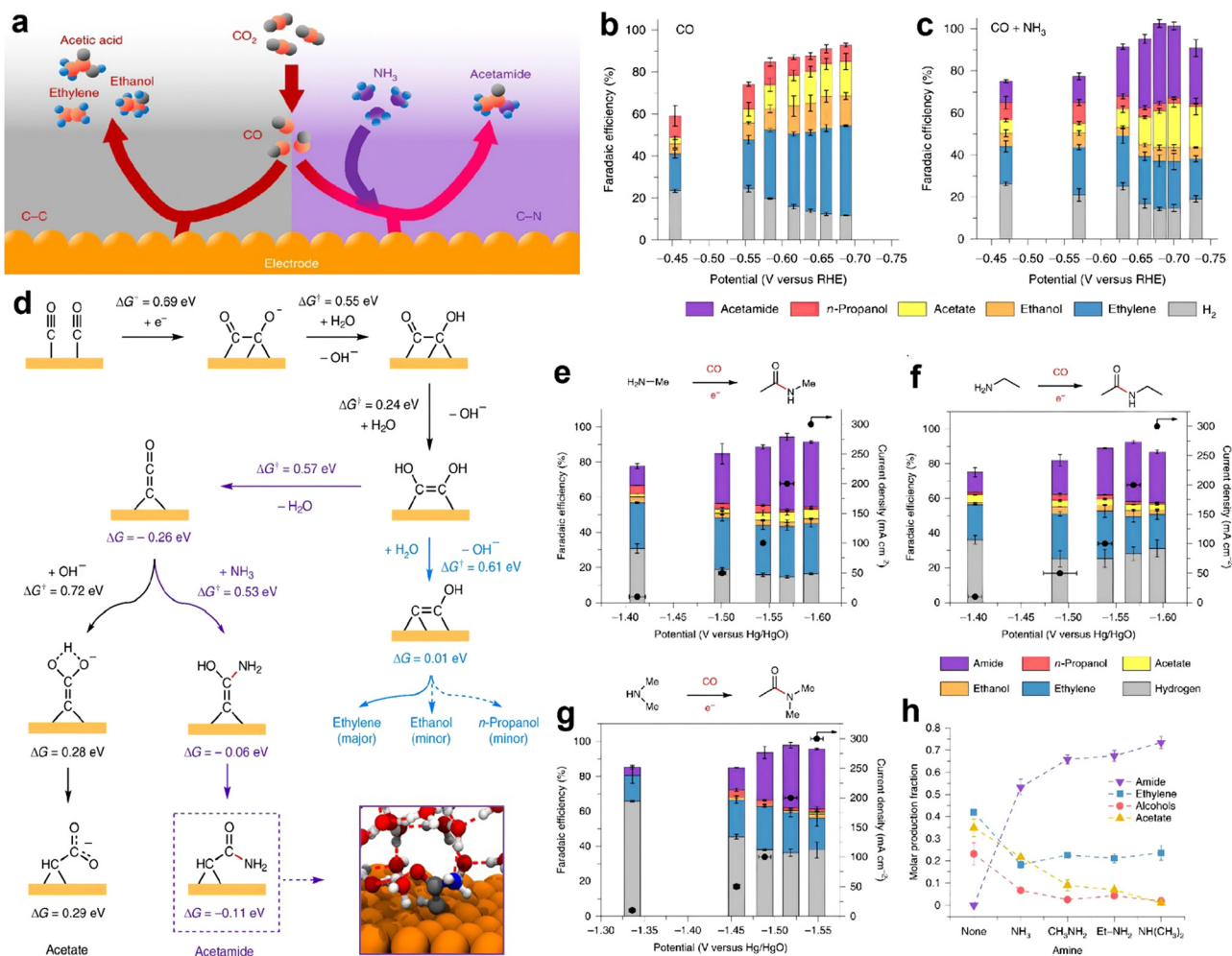


Fig. 17 (a) Schematic depicting NH<sub>3</sub> inducing C–N bond formation from CO electrolysis. (b and c) FE versus the applied potential for CO (b) and CO + NH<sub>3</sub> (c). (d) Mechanism for CO reduction on Cu, where one pathway features \*C=COH for the production of ethylene, ethanol, and n-propanol, whereas the other pathway features \*C=C=O for the production of acetamide and acetate. Total current density and Fes for CO electrolysis in 1.0 M KCl solution with various nitrogen-containing reactants (5.0 M): (e) methylamine, (f) ethylamine, and (g) dimethylamine. (h) Molar production fraction for different C<sub>2+</sub> products at 200 mA cm<sup>-2</sup>. Reproduced with permission from ref. 31. Copyright 2019, Springer Nature.

quantum mechanics research revealed that the formation of C<sub>2</sub>H<sub>4</sub> originated from \*C=COH and that \*C=C=O came from the dehydration of \*(HO)C=COH. Therefore, the intermediate \*C=C=O tended to form at high pH and low potential in competition with the intermediate \*C=COH from the proton-coupled electron transfer. Then, the C–N bond was formed from the reaction of NH<sub>3</sub> with \*C=C=O, and the formation of \*C=C(OH)NH<sub>2</sub> was completed through a water-mediated reaction pathway. Subsequently, \*C=C(OH)NH<sub>2</sub> was isomerized to \*CH-C(=O)NH<sub>2</sub> through the keto-enol tautomer, followed by coupling steps involving two proton-coupled electron transfer steps to ultimately yield the acetamide product. In brief, acetamide is formed through the nucleophilic addition of NH<sub>3</sub> to a surface-bound ketene intermediate, a step that competes with OH<sup>-</sup> addition, leading to the formation of the acetate product.

Similar results were also obtained using a mixture of NH<sub>4</sub>OH + KOH/KCl as the catholyte and using CO as the feed gas

(Fig. 17e–h), demonstrating that acetamide can be produced from both gas- and liquid-phase NH<sub>3</sub> with a noticeable FE. The ratio of ethylene to alcohol products was greatly reduced at moderate to high overpotentials, while the selectivity to acetate products was largely unchanged. Continuous electrolysis tests at a total current density of 100 mA cm<sup>-2</sup> for 8 h were carried out to assess the stability of Cu-catalyzed CO electrolysis in the presence of gas NH<sub>3</sub>, and it was discovered that acetamide could be generated steadily. The authors also verified the origin of oxygen in acetamide by C<sup>18</sup>O isotopic labeling and found that <sup>18</sup>O-labeled acetamide was the main product.

This work demonstrates a new pathway for the production of various amide products via CO electrolysis under ambient conditions. These products are commonly used in the polymer and pharmaceutical industries. Although the NH<sub>3</sub> employed in this work was made from methanol and methane, renewable NH<sub>3</sub> synthesis is now a topic of interest. More importantly, the nucleophilic attack of amines on ketene intermediates enables

the reaction to generate a wider variety of chemistries containing carbon–heteroatom bonds. Previously, these chemicals could not be produced by conventional CO electrolysis. This progress is expected to facilitate CO<sub>2</sub>/CO electrolysis technology for commercial applications.

### 6.3. Methylamine

Methylamine (CH<sub>3</sub>NH<sub>2</sub>) with one of the hydrogen atoms in the NH<sub>3</sub> molecule replaced by a methyl group is a colorless gas or liquid with an ammonia odor at room temperature. It is soluble in water, ethanol or ether, flammable, and explosive when its vapor is mixed with air. Depending on the number of methyl substitutions, monomethyl amine (CH<sub>3</sub>NH<sub>2</sub>, MMA), dimethylamine ((CH<sub>3</sub>)NH, DMA), and trimethylamine ((CH<sub>3</sub>)<sub>3</sub>N, TMA) can be formed. Methylamine is an important fine chemical raw material, which is widely used in various industries and mainly produced by the gas-phase catalytic reaction of methanol and ammonia in the current industry. Under high temperature (350–450 °C) and high pressure (0.5–4.1 MPa), methanol and ammonia are reacted under the action of a catalyst to produce crude methylamine *via* a dehydration or disproportionation reaction, and then separated by distillation to get monomethyl amine, dimethylamine, and trimethylamine with an equilibrium composition of 23 : 27 : 50, respectively.

Electrosynthesis affords a greener process to produce methylamine. Currently, the electrochemical C–N coupling reaction usually has a low efficiency, which is mainly caused by the repulsive dipole–dipole interaction between the adjacent coupling precursors. Thus, to address this problem theoretically, Jiao *et al.* reported the use of N-heterocyclic carbene to alter the unaltered catalyst surface as a simple strategy to weaken the repulsive dipole–dipole interaction. Owing to its excellent conductivity, high surface area, and tunable surface functionalities effective for the ECRR and ENRR,<sup>279,280</sup> Mo<sub>2</sub>NO<sub>2</sub> with O vacancy (Cu<sub>2</sub>@v-Mo<sub>2</sub>NO<sub>2</sub>) and two anchored Cu atoms was chosen as the model catalyst for the C–N coupling reaction from CO and NO. Specifically, the surface carbene-functionalized Cu<sub>2</sub>@v-Mo<sub>2</sub>NO<sub>2</sub> was found to well promote the formation of methylamine from CO and NO by reducing the repulsive dipole–dipole interactions between the adsorbed coupling precursors. The electronic configuration analysis showed that the carbene functionalization played an important role in C–N bond formation by perturbing the electronic configuration between the Cu pairs to induce charge redistribution for the adsorbed intermediates. In particular, the fully overlapping d states significantly split after ligating carbene (Fig. 18a and b). The N atom became negatively charged after the functionalization of the surface of carbene, whereas the C atom maintained its positive charge. Consequently, the electrostatic relationship between the N and C atoms switched from repulsion to attraction, and the C\*CO–N\*NO distance also decreased from 3.7 to 2.8 (Fig. 18c and d), further confirming the weakened dipole–dipole repulsion. Furthermore, the attenuation of the dipole–dipole repulsion between the adjacent carbonaceous and nitrogenous intermediates was demonstrated to be beneficial for C–N bond coupling, which was identified to be the most stable

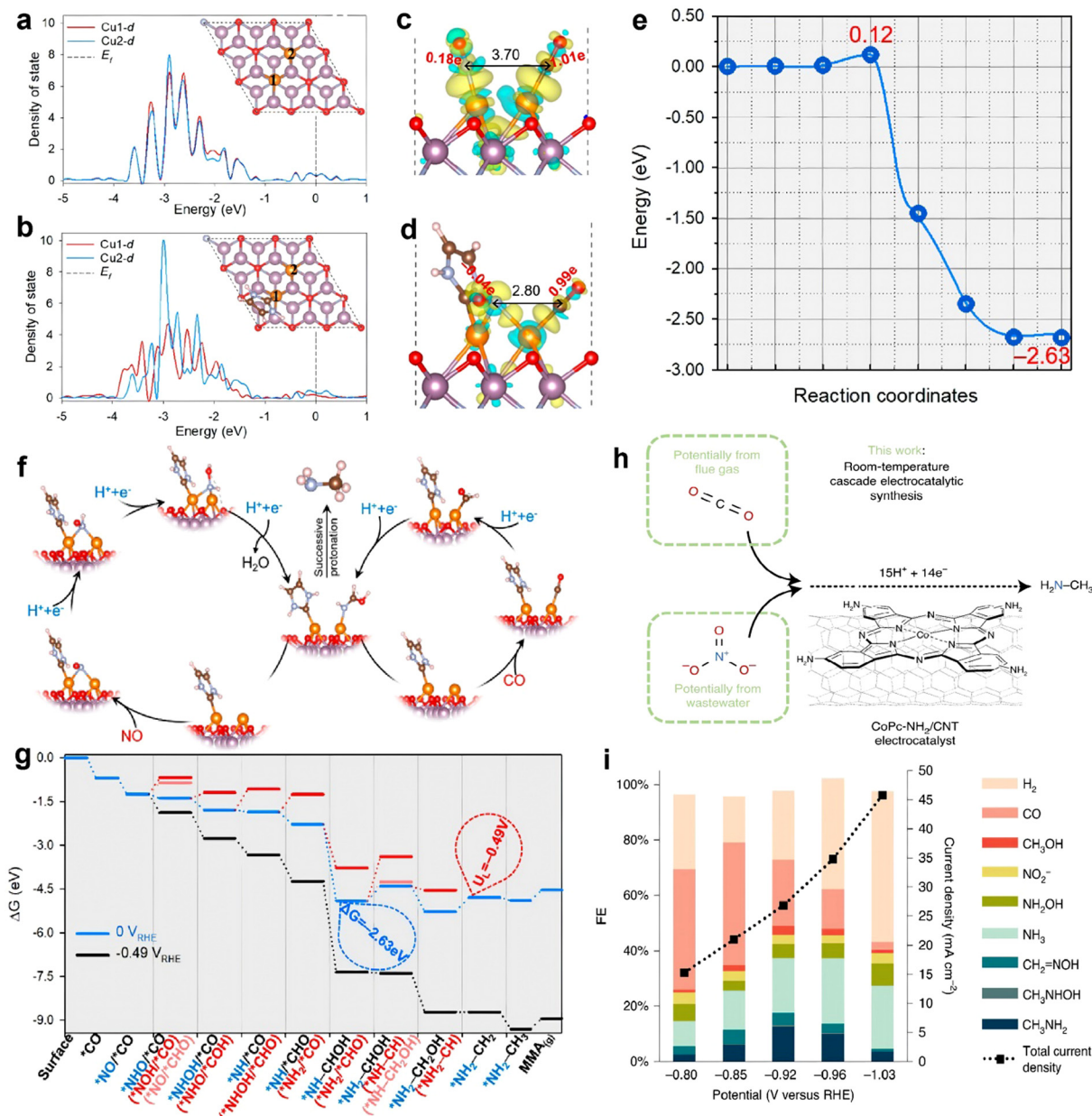
intermediate toward the formation of methylamine over the designed catalyst. Although the \*CO intermediate was protonated to \*CHOH in this reaction route, the \*NO intermediate was reduced to \*NH. Following structural optimization, it was discovered that the \*NH intermediate went toward the nearby Cu site on its own and linked with the \*CHOH intermediate to produce \*NH-CHOH. This electrochemical C–N coupling step exhibited a low kinetic barrier of 0.12 eV and a highly thermodynamically exothermic of 2.63 eV (Fig. 18e), indicating the minimization of the dipole–dipole repulsion by surface carbene functionalization to significantly boost the C–N coupling reaction.

Fig. 18f shows the overall mechanism for the formation of methylamine *via* C–N coupling from NO and CO over the carbene-functionalized Cu<sub>2</sub>@v-Mo<sub>2</sub>NO<sub>2</sub> electrocatalyst. Further evidence that the proposed electrocatalyst possesses activity and selectivity was provided by the low kinetic barrier for C–N coupling (0.12 eV at 0 V *vs.* RHE) and low limiting voltage (0.49 V *vs.* RHE) (Fig. 18g).<sup>221</sup> Additionally, this method to increase bond coupling by surface carbene functionalization can be expanded to include C–C and N–N coupling for the sustainable synthesis of various multi-carbon/nitrogen chemicals because small-molecule precursors (\*CO, \*CHO, \*NO, \*NH, *etc.*) are typically dipole–dipole repulsive. Overall, this theoretical work can aid experimentalists in comprehending the dipole–dipole repulsion as a constraint on couplings and offers novel and practical strategies to issues associated with the dipole–dipole repulsion without being limited by the commonly employed heteroatom anchoring or vacancy engineering.

In the experimental frontier, Wang and co-workers first electrochemically converted CO<sub>2</sub> and NO<sub>3</sub><sup>−</sup> into CH<sub>3</sub>NH<sub>2</sub> in aqueous media under ambient conditions catalyzed by a cobalt β-tetraaminophthalocyanine molecular catalyst supported on carbon nanotubes,<sup>235</sup> as shown in Fig. 18h. Under ambient conditions, the newly developed Co-based catalyst exhibited an overall FE of 13% for the generation of CH<sub>3</sub>NH<sub>2</sub> (Fig. 18i) without any performance decay for at least 16 h of continuous operation with a total turnover number of higher than 5,500. The entire reaction was an eight-step catalytic cascade process, which was made possible by the coupling of two reactive intermediates close to the catalyst surface. This coupling allowed the transfer of 14 e<sup>−</sup> and 15 H<sup>+</sup> to produce each methylamine (CH<sub>3</sub>NH<sub>2</sub>) molecule. The spontaneous condensation of hydroxylamine (NH<sub>2</sub>OH) in NO<sub>3</sub><sup>−</sup> reduction to formaldehyde (HCHO) in the CO<sub>2</sub> reduction to formaldehyde oxime is a key step in the electrochemical C–N coupling reaction, which will further serve as a key intermediate for the formation of CH<sub>3</sub>NH<sub>2</sub>.

### 6.4. Formamide

Formamide (HCONH<sub>2</sub>), the simplest amide compound derived from formic acid, is a transparent oily liquid with a slight ammonia odor, hygroscopic and flammable nature. It is a raw material for synthetic medicines, dyes, herbicides, pesticides, softeners, *etc.* It can also be used as a solvent for spinning



**Fig. 18** PDOS for d-state of Cu atoms in the model (a) without and (b) with surface carbene functionalization. The side view of \*NO and \*CO co-adsorption on  $\text{Cu}_2@\text{v-Mo}_2\text{NO}_2$  (c) without and (d) with surface carbene functionalization, with a charge density difference and Bader charge analysis. The yellow and cyan area represent the accumulation and depletion of charge with a  $0.005 \text{ e A}^{-3}$  isosurface. (e) Minimum energy pathway of C–N coupling between \*NH and \*CHOH on surface carbene-functionalized  $\text{Cu}_2@\text{v-Mo}_2\text{NO}_2$ . (f) Proposed mechanism for the electrosynthesis of methylamine from CO and NO. (g) Free-energy diagram for the information of methylamine over the surface of carbene-functionalized  $\text{Cu}_2@\text{v-Mo}_2\text{NO}_2$ . Reproduced with permission from ref. 278. Copyright 2022, the American Chemical Society. (h) One-pot electrosynthesis of methylamine via C–N coupling reaction from  $\text{CO}_2$  and  $\text{NO}_3^-$  over the  $\text{CoPc-NH}_2/\text{CNT}$  catalyst. (i) FE and total current density for various products over the  $\text{CoPc-NH}_2/\text{CNT}$  catalyst. Reproduced with permission from ref. 235. Copyright 2021, Springer Nature.

synthetic fibers, plastic processing, and the production of lignocaine inks. There are many industrial methods for the synthesis of formamide,<sup>281–284</sup> as follows: (1) the first step is to generate methyl formate ( $\text{HCOOCH}_3$ ) from CO and methanol under the action of sodium methoxide.<sup>285</sup> In the second step, methyl formate is re-ammonolysis to form formamide at 80–100 °C and 0.2–0.6 MPa. (2) Formic acid is first esterified with methanol to form methyl formate,<sup>286</sup> which is then

decomposed by ethyl carbamate to form formamide. Then, the methanol and impurities are separated by distillation to obtain the finished product. This method has become obsolete due to its high cost. (3) Formamide is directly synthesized from CO and ammonia under the catalysis of sodium methoxide at high pressure (10–30 MPa) and temperature of 80–100 °C ( $\text{CO} + \text{NH}_3 \rightarrow \text{HCONH}_2$ ).<sup>287</sup> Currently, this is the main industrial process for the production of formamide. (4) Formamide is

synthesized by ammonia water and formic acid,<sup>286</sup> in which ammonia water and formic acid first generate ammonium formate ( $\text{HCOOH} + \text{NH}_3 \rightarrow \text{HCOO}^- \text{NH}_4^+$ ). Subsequent heating ( $\text{HCOO}^- \text{NH}_4^+ \rightarrow \text{HCONH}_2 + \text{H}_2\text{O}$ ) generates formamide.<sup>(5)</sup> Formamide is also generated by the aminolysis of ethyl formate ( $\text{HCOOCH}_2\text{CH}_3 + \text{NH}_3 \rightarrow \text{HCONH}_2 + \text{CH}_3\text{CH}_2\text{OH}$ ).<sup>288</sup> However, these traditional thermochemical synthesis processes require high temperatures and high pressures, resulting in huge energy consumption and  $\text{CO}_2$  emissions.

Instead of using the traditional reaction of fossil-fuel-derived CO and  $\text{NH}_3$  under harsh conditions to produce formamide, Zhang's group reported a sustainable electrosynthesis approach to upgrade  $\text{CO}_2$ -derived formate ( $\text{HCOOH}$ ) into formamide.<sup>221</sup> The precursor formate can be specially prepared through the electroreduction of  $\text{CO}_2$  at an industrial current density of  $500 \text{ mA cm}^{-2}$ .<sup>289–291</sup> It is of great significance to explore economical and green methods to upgrade  $\text{CO}_2$ -derived formic acid into formamide, particularly considering that the annual global demand for formate is only  $\sim 1$  million tons, which is much lower than the current scale of  $\text{CO}_2$  emissions.<sup>292,293</sup>

Theoretical predictions demonstrated that a Cu catalyst is a promising catalyst for the C–N coupling reaction by using formate and nitrite as C and N sources (Fig. 19a and b), respectively. The LSV curves showed the possible appearance of co-reduction over low-coordinated Cu nanocubes (ER–Cu) with an increased reduction current in the coexistence of formate and nitrite (Fig. 19b). Over the ER–Cu catalyst, 90.0% selectivity from  $\text{HCOOH}$  to formamide and a relatively high FE of 29.7% for the formation of formamide were obtained at  $-0.4 \text{ V vs. RHE}$  in a mixed solution of  $0.5 \text{ M NaOH} + 0.2 \text{ M HCOOH} + 0.02 \text{ M NaNO}_2$  (Fig. 19c), as confirmed by  $^1\text{H}$  NMR spectroscopy (Fig. 19d). Also, the FE of 16.4% for the generation of acetamide over the ER–Cu catalyst was obtained (Fig. 19e).

Furthermore, a series of *in situ* controlled experiments was conducted to reveal the formation mechanism for the key C–N bonds *via* coupling  $^*\text{CHO}$  and  $^*\text{NH}_2$  intermediates (Fig. 19f–i). As shown in Fig. 19f, both  $^*\text{CHO}$  ( $1720 \text{ cm}^{-1}$ ) and  $^*\text{NH}_2$  ( $1155 \text{ cm}^{-1}$ ) intermediates were detected using formic acid and nitrite as raw materials by *in situ* attenuated total reflection surface-enhanced infrared absorption spectroscopy (ATR–SEIRAS).<sup>294–298</sup> The control tests with formic acid or nitrite confirmed that the  $^*\text{CHO}$  and  $^*\text{NH}_2$  species originated from formic acid and nitrite reduction (Fig. 19h and i), respectively. Isotope-labeling *in situ* ATR–SEIRAS spectroscopy was carried out using  $^{15}\text{NO}_2^-$  as an N-source, where the C– $^{15}\text{N}$  bond and  $^*\text{NH}_2$  shifted to the lower wavenumber region (1410 and  $1120 \text{ cm}^{-1}$ ) due to the isotope effect (Fig. 19g). The results confirmed that the formation of formamide originated from the C–N coupling reaction from  $\text{HCOOH}$  and  $\text{NO}_2^-$  catalyzed by the ER–Cu catalyst. The reaction energy barriers of the coupled process were compared with that of the single reduction process (Fig. 19j).<sup>221</sup> Notably, the conversion of formic acid to the  $^*\text{CHO}$  intermediate was identified as a potential-determining step (PDS) with an energy barrier ( $\Delta G_{\text{PDS}}$ ) of 1.19 eV on the ER–Cu catalyst.

Meanwhile, the coupling of the  $^*\text{CHO}$  and  $^*\text{NH}_2$  intermediates to form the critical C–N bond on the ER–Cu catalyst surface was thermodynamically favorable ( $-1.120 \text{ eV}$ ). In addition, by further analyzing the important competing reactions in the electrochemical system, namely, the hydrogenation reaction of  $^*\text{CHO}$  and  $^*\text{NH}_2$ , the calculation showed that the energy barrier of the coupling step was much lower than that of hydrogenation alone on ER–Cu (the hydrogenation barriers for  $^*\text{NH}_2$  and  $^*\text{CHO}$  are  $-0.478$  and  $-0.08 \text{ eV}$ , respectively). The above-mentioned results demonstrate that  $^*\text{CHO}$  and  $^*\text{NH}_2$  can be spontaneously coupled to the low-coordination Cu sites, thus enabling the electrosynthesis process to produce formamide at a high yield. By converting  $\text{NO}_2^-$  to  $\text{NO}_3^-$  and using  $\text{CO}_2$ -derived ethanoic acid as the C source, this electrochemical method can be extended to the synthesis of acetamide.

In another study, Zhang *et al.* reported a strategy for the direct synthesis of formamide *via* the electrooxidation of  $\text{CH}_3\text{OH}$  and  $\text{NH}_3$  over a commercial boron-doped diamond (BDD) catalyst with a formamide FE of 41.2% at a high current density of  $120 \text{ mA cm}^{-2}$ .<sup>222</sup> Compared to the traditional high-temperature and high-pressure reaction conditions (Fig. 20a and b), renewable energy-driven electrosynthesis has attracted increasing interest for a carbon-neutral future. It has been found that the formation of the C–N bond in the formamide electrosynthesis originates from the nucleophilic attack of the aldehyde-like intermediate by  $\text{NH}_3$ . For a pilot-scale test in an 8 L electrolytic cell on a BDD electrode, the FE of formamide could still reach 33.5% at  $120 \text{ mA cm}^{-2}$  and the yield of formamide achieved was  $36.9 \text{ g h}^{-1}$ , confirming that this technique has broad prospects in the large-scale electrosynthesis of formamide. Using commercial BDD as the anode material and  $0.5 \text{ M NaHCO}_3$  as an electrolyte, the products and raw materials were identified and quantified by  $^1\text{H}$  NMR, ion chromatography (IC), and colorimetry. Simultaneously, the products were further confirmed by liquid chromatography–electrospray mass spectrometry (LC–MS). To improve the formamide electrosynthesis performance, the molar ratio of  $\text{CH}_3\text{OH}$  to  $\text{NH}_3$  was first optimized. When the molar ratio of  $\text{CH}_3\text{OH}$  to  $\text{NH}_3$  was 5 : 1 and in  $0.5 \text{ M NaHCO}_3$  electrolyte, the FE of formamide was the highest, reaching 41.2% at  $120 \text{ mA cm}^{-2}$ . Notably, the generation of formamide was completely inhibited in a strong alkaline electrolyte ( $0.5 \text{ M NaOH}$ ) (Fig. 20c and d), probably due to the rapid self-decomposition of formaldehyde-like intermediates into  $\text{HCOOH}$  and  $\text{CH}_3\text{OH}$ .

According to the thermocatalytic analysis, there are two possible paths for the formation of formamide (Fig. 20e), as follows: (1) the intermediate aldehyde obtained by the electrochemical oxidation reaction of  $\text{CH}_3\text{OH}$  reacts with  $\text{NH}_3$  to form aldimine, which is further oxidized to nitrile, and the nitrile is hydrolyzed to generate formamide (Pathway 1).<sup>299–301</sup> (2) The formaldehyde produced by  $\text{CH}_3\text{OH}$  dehydrogenation/dehydration reacts with  $\text{NH}_3$  to form hemiamine, which is subsequently dehydrogenated/dehydrated to form formamide (Pathway 2).<sup>302–304</sup> The catholyte and anolyte were the same (2 : 1 molar ratio of  $\text{CH}_3\text{OH}$  to  $\text{NH}_3$  in  $0.5 \text{ M NaHCO}_3$ ) in an H-type cell separated by a membrane. A series of control experiments was

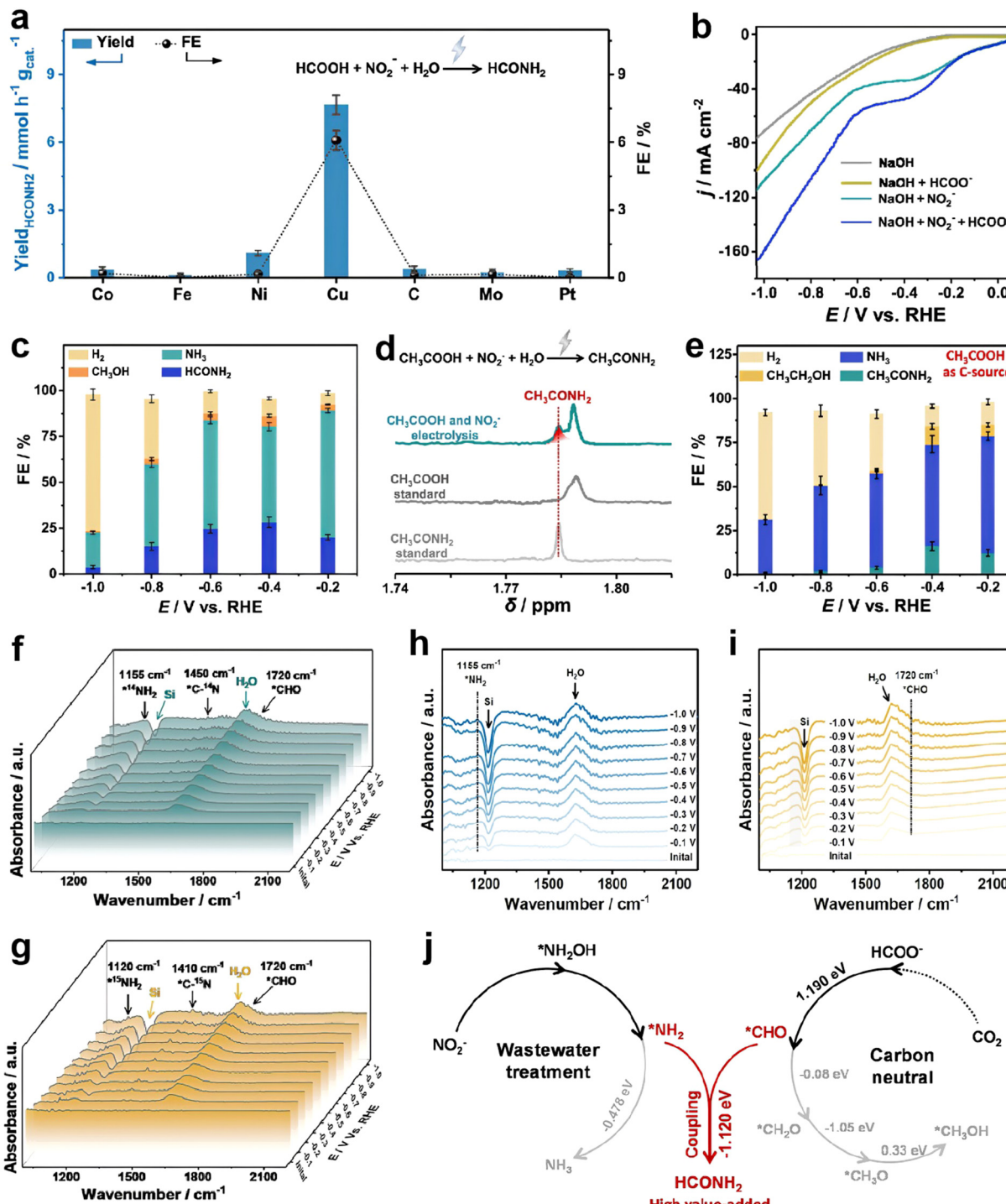


**Fig. 19** (a) Catalyst screening for the electrosynthesis of  $\text{HCONH}_2$  via C–N coupling reaction using  $\text{HCOO}^-$  and  $\text{NO}_2^-$  as C and N sources, respectively. (b) LSV curves of Cu-based catalyst in various electrolytes. (c) FEs for different reduction products. (d)  $^1\text{H}$  NMR spectroscopy. (e) FEs of different products using  $\text{CO}_2$ -derived ethanoic acid as a C-source. Potential-dependent *in situ* ATR-SEIRAS spectra using formic acid as the C source and (f)  $^{14}\text{NO}_2^-$  and (g)  $^{15}\text{NO}_2^-$  as the N source. (h) Potential-dependent *in situ* ATR-SEIRAS with the addition of only  $\text{NO}_2^-$ . (i) Potential-dependent *in situ* ATR-SEIRAS with the addition of only  $\text{HCOO}^-$ . (j) Schematic illustration of the generation pathway of  $\text{HCONH}_2$ . Reproduced with permission from ref. 221. Copyright 2022, the American Chemical Society.

performed to determine the reaction pathway (Fig. 20f and g). Firstly, various possible oxidized derivatives of  $\text{NH}_3$ , such as  $\text{NO}_3^-$ ,  $\text{NO}_2^-$ ,  $\text{NH}_2\text{OH}$ , and  $\text{N}_2\text{H}_4$ , were mixed with  $\text{CH}_3\text{OH}$  for

electrolysis. However, none of the products containing formamide were obtained, indicating that  $\text{NH}_3$  played a key role in the formation of C–N bonds. When  $\text{CH}_3\text{OH}$  was replaced with

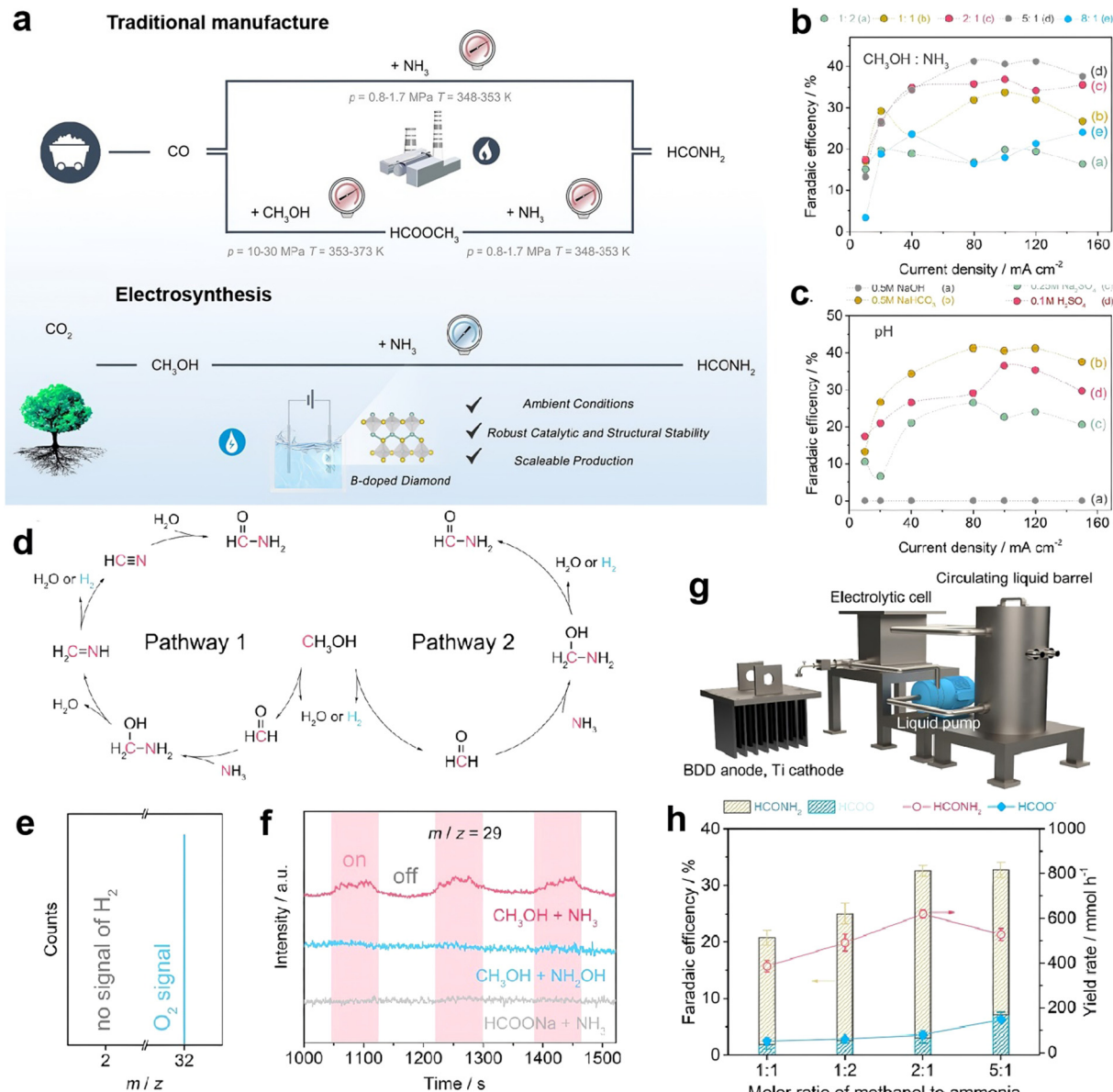


**Fig. 20** (a) Synthesis of formamide by the industrial thermochemical pathway and electrosynthesis technology. Current density-dependent FE over BDD under different (b) feeding ratios of  $\text{CH}_3\text{OH}$  to  $\text{NH}_3$  and (c) pH. (d) Possible reaction pathways for the coupling of  $\text{CH}_3\text{OH}$  and  $\text{NH}_3$  to formamide via electrooxidation over BDD. (e) GC-MS analysis of  $\text{H}_2$  after electrolysis. (f) Online DEMS measurements over BDD with different electrolytes in 0.5 M  $\text{NaHCO}_3$  under 10  $\text{mA cm}^{-2}$ . (g) Scheme of the scaled-up electrolysis device. (h) Optimization of  $\text{CH}_3\text{OH}$  to  $\text{NH}_3$  molar ratio for the synthesis of formamide at 100  $\text{mA cm}^{-2}$ . Reproduced with permission from ref. 222. Copyright 2022, John Wiley & Sons, Inc.

$\text{HCHO}$  or  $\text{HCOO}^-$ , the carboxamide product could be detected only in the mixture of  $\text{HCHO}$  and  $\text{NH}_3$ , demonstrating the critical role of  $\text{HCOH}$  in the formation of the C–N bonds.<sup>305</sup> After the reaction, no  $\text{H}_2$  by-product could be detected in the anode compartment, indicating that no dehydrogenation reaction occurred. These results indicated that  $\text{H}_2\text{C}=\text{NH}$  was the key intermediate in the generation of formamide, and pathway 1 may be the optimal pathway for the generation of formamide.

Harnessing renewable energy, especially solar- and wind-power, has important implications for sustainable electrosynthesis. Thus, to explore the application potential of the large-scale electrosynthesis of formamide on BDD, a series of performance

optimization experiments was carried out at different current densities in an 8 L amplified single-cell electrolysis device (electrode area 2200  $\text{cm}^2$ ) driven by an external renewable power source (Fig. 20h). The results showed that when the molar ratio of  $\text{CH}_3\text{OH}$  to  $\text{NH}_3$  was 2:1 at 120  $\text{mA cm}^{-2}$ , the yield and FE reached up to 0.82  $\text{mol h}^{-1}$  and 33.5%, respectively (Fig. 20i).

### 6.5. Ethylamine

Ethylamine ( $\text{C}_2\text{H}_5\text{NH}_2$ ) is a colorless gas with a strong ammonia odor, which will condense into a liquid miscible with almost all solvents below room temperature.  $\text{C}_2\text{H}_5\text{NH}_2$  has been widely

used in dye synthesis, extractants, emulsifiers, pharmaceutical raw materials, and reagents for organic synthesis in the chemical industry. Ethylamine can be produced on an industrial scale *via* two common methods, as follows: (1) ethanol ammoniation method: ethanol and ammonia are fed in a ratio of 4:1, and  $\text{Al}_2\text{O}_3$  is used as a catalyst to carry out the ammoniation reaction ( $\text{C}_2\text{H}_5\text{OH} + \text{NH}_3 \rightarrow \text{C}_2\text{H}_5\text{NH}_2 + \text{H}_2\text{O}$ ) at a temperature of 350–400 °C and pressure of 2.45–2.94 MPa, followed by fractional distillation to obtain ethylamine.<sup>306,307</sup> (2) Acetaldehyde and hydrogen ammoniation: ethylamine can be prepared by reacting acetaldehyde, hydrogen, and ammonia as raw materials by using nickel as a catalyst ( $\text{CH}_3\text{CHO} + \text{NH}_3 + \text{H}_2 \rightarrow \text{C}_2\text{H}_5\text{NH}_2 + \text{H}_2\text{O}$ ).<sup>308,309</sup> Besides, ethylamine can be also prepared by several other methods (*e.g.*,  $\text{C}_2\text{H}_4 + \text{NH}_3 \rightarrow \text{C}_2\text{H}_5\text{NH}_2$ ,  $\text{C}_2\text{H}_5\text{Cl} + \text{NH}_3 + \text{KOH} \rightarrow \text{C}_2\text{H}_5\text{NH}_2 + \text{KCl} + \text{H}_2\text{O}$ ),<sup>310,311</sup> but they are not economical.

Recently, Wang's group reported the first electrochemical conversion of  $\text{CO}_2$  and  $\text{NO}_3^-$  to ethylamine *via* a multi-electron-proton reduction process on oxide-derived Cu NPs in a near-neutral aqueous electrolyte (Fig. 21a),<sup>232</sup> confirming the possibility for the electrosynthesis of  $\text{C}_{2+}$  organonitrogen compounds from cheap and abundant inorganic feedstocks. As shown in Fig. 21b, the Cu nanoparticles were active for both  $\text{CO}_2$  and  $\text{NO}_3^-$  electroreduction. Specifically,  $\text{C}_2\text{H}_4$  (FE = 36.3%) and  $\text{C}_2\text{H}_5\text{OH}$  (FE = 14.3%) were obtained as the main hydrocarbon products in 1.0 M  $\text{KHCO}_3$  electrolyte. Ammonia with an FE of 73.5% and a partial current density of 40.2 mA cm<sup>-2</sup> was formed in Ar-saturated 1.0 M  $\text{KHCO}_3$  containing 0.1 M  $\text{KNO}_3$  aqueous solution, while no C–N bond-containing compound was produced. However, by replacing Ar with high-purity  $\text{CO}_2$  in 1.0 M  $\text{KHCO}_3 + 0.1 \text{ M KNO}_3$  electrolyte, acetaldoxime ( $\text{C}_2\text{H}_5\text{NO}$ ) with a relatively small FE of 0.36% was detected by <sup>1</sup>H NMR spectroscopy after a continuous 1 h reduction reaction test (Fig. 21c). Interestingly, ethylamine was also formed in the electrochemical co-reduction process. As shown in Fig. 21d and e, the mechanistic analyses demonstrated that acetaldoxime was the key intermediate to ethylamine, which resulted from the condensation reaction between acetaldehyde and  $\text{NH}_2\text{OH}$ . The further reduction of the key intermediate of acetaldoxime led to the formation of the final ethylamine. These results indicated that the overall yield of ethylamine was limited by the competing reduction of  $\text{CH}_3\text{CHO}$  to  $\text{C}_2\text{H}_5\text{OH}$  and  $\text{NH}_2\text{OH}$  to  $\text{NH}_3$ .

In summary, the electrochemical C–N coupling reaction involves the isolated reduction of the carbon precursor and nitrogen precursor to the respective intermediates. Considering that the various reactants (including,  $\text{CO}_2$ ,  $\text{N}_2$ ,  $\text{NO}$ ,  $\text{NO}_2^-$ ,  $\text{NO}_3^-$ , and  $\text{NH}_3$ ) differ in their chemical makeup, it is necessary and desirable to rationally design electrocatalysts possessing multiple active sites with the appropriate distance to effectively couple these intermediates.

Thus far, different strategies have been applied to design high-efficiency electrocatalysts, including hetero-structured hybrids,<sup>219,312</sup> Mott–Schottky heterostructures,<sup>237</sup> oxygen-vacancy defect engineering,<sup>34,223,229,233</sup> nano-alloying,<sup>227</sup> facet engineering,<sup>36</sup> core–shell hierarchical structure,<sup>234</sup> and doping

with heteroatoms,<sup>35,230</sup> single-atoms,<sup>231</sup> and dual-atoms.<sup>228,313</sup> To achieve high activity and high productivity in the design of electrocatalysts for C–N coupling reactions, the following points should be systematically considered: (1) a higher specific surface area with easier adsorption of the reactants and facile desorption of the product are necessary. (2) The catalyst needs to possess multiple active sites for the co-activation and co-reduction of the reactants in similar potential ranges. (3) The electrocatalyst must have specificity and selectivity toward the simultaneous reduction of carbon and nitrogen sources. (4) For the suppression of competing reactions (*e.g.*, HER), the choice of electrolyte and catalyst is crucial. In this regard, an electrocatalyst should have multiple active sites and selectivity toward both the ECRR and ENRR under a similar potential window, which may be effective for enhancing the electrochemical C–N coupling reaction from  $\text{CO}_2$  and nitrogenous small molecules.

## 7. Perspectives and outlook

In this review, we provided an updated comprehensive summary of the recent research development on the electrosynthesis of high-value-added organonitrogen compounds from the abundant  $\text{CO}_2$  and nitrogenous small molecules ( $\text{N}_2$ ,  $\text{NO}$ ,  $\text{NO}_2^-$ ,  $\text{NO}_3^-$ ,  $\text{NH}_3$ , *etc.*) *via* the electrochemical C–N coupling reaction. Initially, the basic concepts, classification, reaction characteristics, and key evaluation indices for the electrosynthesis and electrocatalytic reactor (H-type cell, flow cell, and MEA cell) were introduced. Next, the two key reactions (*i.e.*, ECRR and ENRR) involved in the C–N coupling reaction were described in detail. Furthermore, the design and reaction mechanism of electrocatalysts for the formation of various target products from the electrocatalytic C–N coupling reaction and the effects of different C and N sources on each of the target products were discussed in depth.

As is known, carbon and nitrogen constitute our colorful world due to their abundant reserves and complex bonding configurations in a large variety of chemical compounds. Thus, the research on electrochemical C–N coupling reactions is significant. In nature, plants convert  $\text{CO}_2$  and  $\text{N}_2$  into organic matter through photosynthesis to keep our planet blue and vibrant. Our goal is to realize an artificial carbon and nitrogen cycle, in which the  $\text{CO}_2$  and  $\text{N}_2$  molecules in the atmosphere are directly converted into energy substances. In the electrocatalytic C–N coupling reaction,  $\text{CO}_2$  and nitrogenous small molecules ( $\text{N}_2$ ,  $\text{NO}$ ,  $\text{NO}_2^-$ ,  $\text{NO}_3^-$ ,  $\text{NH}_3$ , *etc.*) are first activated to become intermediates for further conversion to other useful species. However, our current understanding of the adsorption and desorption of these key intermediates on the electrocatalyst surface, the electrocatalytic bond cleavage, and formation between C, N, O, and H, and their interactions with the electrocatalyst surface is still in its infancy. Therefore, the exploration of scientific problems in this field is still a broad blue ocean.

In recent years, a series of breakthroughs has been made in the electrocatalytic C–N coupling reaction to gradually enhance

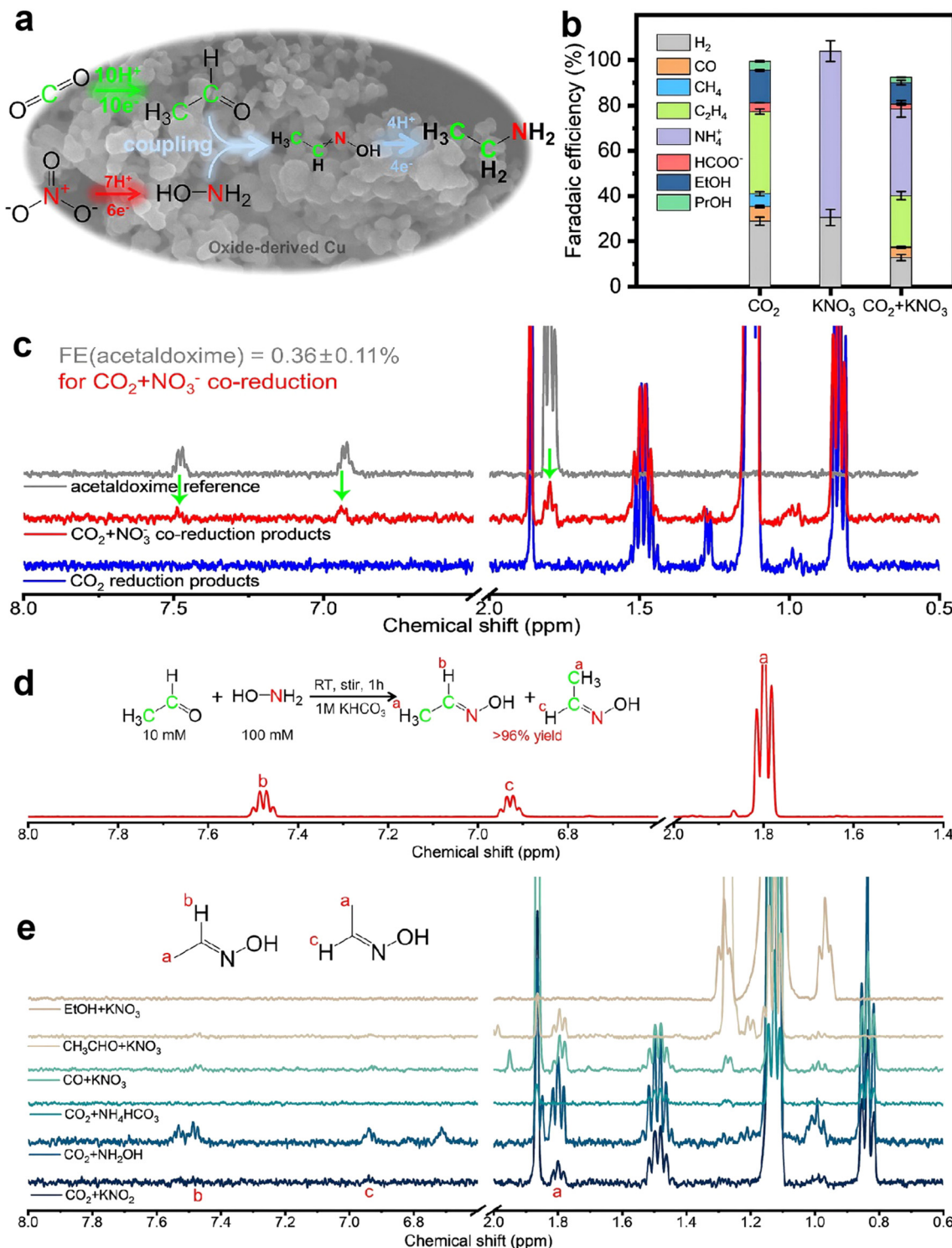


**Fig. 21** (a) Schematic illustration of the electrochemical reduction of CO<sub>2</sub> via coupling with NO<sub>3</sub><sup>-</sup> into acetaldoxime and ethylamine over oxide-derived Cu nanoparticles. (b) FEs for different electrochemical reductions on the catalyst, including pure CO<sub>2</sub> reduction, pure NO<sub>3</sub><sup>-</sup> reduction, and CO<sub>2</sub> + NO<sub>3</sub><sup>-</sup> coupling reaction. (c) <sup>1</sup>H NMR spectra of the post-electrolysis solutions corresponding to (b). (d) <sup>1</sup>H NMR spectrum of the product solution after mixing acetaldehyde and NH<sub>2</sub>OH. (e) <sup>1</sup>H NMR spectra of the post-electrolysis solutions after performing potentiostatic electrolyses with different C and N sources. Reproduced with permission from ref. 232. Copyright 2021, Elsevier.

the selectivity, yield, and stability. However, the yield and selectivity of the electrocatalytic C–N coupling reaction are still much lower than that for traditional synthetic methods. The

construction of efficient, economical, and green catalytic systems to realize the large-scale electrosynthesis of organonitrogen compounds *via* C–N coupling reactions under mild

conditions is still a key issue that needs to be the focus in the future. Although great progress in the rational design and development of efficient electrocatalysts for the C–N coupling reaction has been achieved in recent years, there are still many challenges that need to be further explored and solved before its industrial application can be realized.

Firstly, the mass transfer process severely limits the efficient progress of the C–N coupling reaction due to the low solubility of CO<sub>2</sub> and N<sub>2</sub> molecules in water. Therefore, the engineering problems faced in the electrochemical C–N coupling reaction must be solved to realize its large-scale production. In this case, the appropriate design of the electrochemical reactor is crucial for achieving high energy efficiency and low cost toward the C–N coupling reaction. An ideal electrolyzer should have advantageous properties to facilitate electron transfer, ion transport, and controllable gas diffusion. At the macro-scale, commercially relevant current densities have been achieved in GDE-based reactors by eliminating the mass transport limitations. MEA with zero-gap function excels in long-term stability and selectivity. However, some challenges, such as industrial-scale manufacturing and operational stability of GDEs, hydration management, and CO<sub>2</sub>/N<sub>2</sub> crossover, still need to be addressed. On the microscopic side, a well-designed reaction interface (electrode–reactant–electrolyte) and local microenvironment will be beneficial for controlling CO<sub>2</sub> electrolysis and optimizing the performance. Attempts to further optimize the C–N coupled reaction system in terms of three-dimensional freestanding integrated catalyst electrodes, novel electrolytes, high-performance membranes, and powerful electrochemical reactors are attractive for electrical synthesis at commercially relevant current densities, where the introduction of innovative concepts and devices by following the chemical engineering principles is strongly recommended.

Secondly, the rational design of electrocatalysts is the key to C–N coupling reactions. In this context, the targeted design of high-performance catalytically active sites is required. High-throughput material calculation and screening are needed for digital research and the development of new materials, including advanced electrocatalysts with high activity, selectivity, and stability for the C–N coupling reaction. Combined experimental and computer simulation methods should be employed to study the structure–property/performance relationship. The deep integration of new technologies, such as high-throughput computing, high-throughput preparation, and high-throughput characterization, will enable the faster and more accurate acquisition of the composition–structure–process–performance relationship. This enables the design prediction of advanced new catalysts and processes, enabling the required catalysts to be obtained more quickly.

Thirdly, an in-depth mechanistic understanding of electrocatalysts for C–N coupling reactions is still lacking. For instance, the specific mechanism of how the active site affects the catalytic activity and selectivity is still unclear. Currently, the design and development of highly efficient electrocatalysts still rely on trial and error. Thus, advanced characterization techniques need to be developed and applied to establish the

structure–activity relationship of electrocatalysts (especially heterogeneous catalysts) for C–N coupling reactions. The mechanism study of the catalytic process by *in situ* spectroscopy will provide useful references for catalyst design and the establishment of efficient catalytic systems. Therefore, using modern catalyst characterization methods and theoretical calculation methods to develop efficient, economical, and industrialized C–N coupling reaction systems will be the future direction of development.

Fourthly, the exploration of the real/operational reaction mechanism is another key point for the research and development of electrochemical C–N coupling reactions. However, the complexity of the electrocatalytic reaction environment and the limited experimental methods make the exploration of the reaction mechanism under operational conditions very difficult, if not impossible. Most of the current mechanistic studies rely on first-principles calculations. In fact, the electrocatalytic C–N coupling reaction in an aqueous solution is a complex reaction process involving the gas–liquid–solid three-phase interface, and it is difficult for theoretical models to fully fit this real reaction process/environment. It is particularly critical to provide direct evidence for the confirmation of the reaction mechanism and intermediates through experimental methods. Therefore, “good tools are essential things”. Besides the conventional *ex situ* characterization and detection methods, *in situ* structural characterization techniques, such as *in situ* transmission electron microscopy, *in situ* Raman spectroscopy, *in situ* Fourier transform infrared spectroscopy, and *in situ* synchrotron radiation spectroscopy, need to be explored in depth to capture the reaction intermediates. It is necessary to establish the precise structure–property relationship on the atomic scale, explain the reaction mechanism, and provide guidance for the optimization of the catalyst structure.

In conclusion, electrochemical synthesis *via* the C–N coupling reaction has both challenges and opportunities. Thus, with further research and development in this field and continued worldwide effort, this will surely become a very important and promising R&D area in the 21st century and make greater contributions to the progress of mankind.

## Conflicts of interest

There are no conflicts to declare.

## Acknowledgements

This work was supported by the National Natural Science Foundation of China (U22A20432, 22278364, 22211530045, 22178308), National Key Research and Development Program of China (2022YFB4002100), the Development Project of Zhejiang Province’s “Jianbing” and “Lingyan” (2023C01226), the Fundamental Research Funds for the Central Universities (226-2022-00044, 226-2022-00055), the Startup Foundation for Hundred-Talent Program of Zhejiang University, the Research Funds of Institute of Zhejiang University-Qzhou

(IZQ2021RCZX026), the Science and Technology Program of Zhejiang University-Qzhou (IZQ2021KJ2008), and the Australian Research Council (ARC, DP 190103881 and FL 190100126).

## Notes and references

- 1 S. Chu and A. Majumdar, *Nature*, 2012, **488**, 294–303.
- 2 V. R. Stamenkovic, D. Strmcnik, P. P. Lopes and N. M. Markovic, *Nat. Mater.*, 2017, **16**, 57–69.
- 3 Y. Jia, K. Jiang, H. Wang and X. Yao, *Chem.*, 2019, **5**, 1371–1397.
- 4 R. F. Service, *Science*, 2014, **345**, 610.
- 5 C. Kingston, M. D. Palkowitz, Y. Takahira, J. C. Vantourout, B. K. Peters, Y. Kawamata and P. S. Baran, *Acc. Chem. Res.*, 2020, **53**, 72–83.
- 6 F. Marken, A. J. Cresswell and S. D. Bull, *Chem. Rev.*, 2021, **21**, 2585–2600.
- 7 M. A. Bajada, J. Sanjose-Orduna, G. Di Liberto, S. Tosoni, G. Pacchioni, T. Noel and G. Vile, *Chem. Soc. Rev.*, 2022, **51**, 3898–3925.
- 8 G. Soloveichik, *Nat. Catal.*, 2019, **2**, 377–380.
- 9 C. Kingston, M. D. Palkowitz, Y. Takahira, J. C. Vantourout, B. K. Peters, Y. Kawamata and P. S. Baran, *Acc. Chem. Res.*, 2020, **53**, 72–83.
- 10 X. Sun, H. Chen, Y. Yin, M. T. Curnan, J. W. Han, Y. Chen and Z. Ma, *Small*, 2021, **17**, e2005383.
- 11 Z. Pu, I. Saana Amiinu, F. Gao, Z. Xu, C. Zhang, W. Li, G. Li and S. Mu, *J. Power Sources*, 2018, **401**, 238–244.
- 12 X. Cui, R. Huang and D. Deng, *EnergyChem*, 2021, **3**, 100050.
- 13 H. Yin, Y. Dou, S. Chen, Z. Zhu, P. Liu and H. Zhao, *Adv. Mater.*, 2020, **32**, 1904870.
- 14 R. Francke, B. Schille and M. Roemelt, *Chem. Rev.*, 2018, **118**, 4631–4701.
- 15 S. Nitopi, E. Bertheussen, S. B. Scott, X. Liu, A. K. Engstfeld, S. Horch, B. Seger, I. E. L. Stephens, K. Chan, C. Hahn, J. K. Norskov, T. F. Jaramillo and I. Chorkendorff, *Chem. Rev.*, 2019, **119**, 7610–7672.
- 16 R. I. Masel, Z. Liu, H. Yang, J. J. Kaczur, D. Carrillo, S. Ren, D. Salvatore and C. P. Berlinguette, *Nat. Nanotechnol.*, 2021, **16**, 118–128.
- 17 J. Y. T. Kim, P. Zhu, F.-Y. Chen, Z.-Y. Wu, D. A. Cullen and H. Wang, *Nat. Catal.*, 2022, **5**, 288–299.
- 18 X. Liu, J. Xiao, H. Peng, X. Hong, K. Chan and J. K. Norskov, *Nat. Commun.*, 2017, **8**, 15438.
- 19 J. E. Huang, F. Li, A. Ozden, A. Sedighian Rasouli, F. P. García de Arquer, S. Liu, S. Zhang, M. Luo, X. Wang, Y. Lum, Y. Xu, K. Bertens, R. K. Miao, C.-T. Dinh, D. Sinton and E. H. Sargent, *Science*, 2021, **372**, 1074–1078.
- 20 Z. Sun, T. Ma, H. Tao, Q. Fan and B. Han, *Chem.*, 2017, **3**, 560–587.
- 21 J. Wu, T. Sharifi, Y. Gao, T. Zhang and P. M. Ajayan, *Adv. Mater.*, 2019, **31**, 1804257.
- 22 W. Ma, X. He, W. Wang, S. Xie, Q. Zhang and Y. Wang, *Chem. Soc. Rev.*, 2021, **50**, 12897–12914.
- 23 T. Burdyny and W. A. Smith, *Energy Environ. Sci.*, 2019, **12**, 1442–1453.
- 24 X. She, Y. Wang, H. Xu, S. C. E. Tsang and S. P. Lau, *Angew. Chem., Int. Ed.*, 2022, **61**, e202211396.
- 25 F. Pan, X. Yang, T. O'Carroll, H. Li, K. J. Chen and G. Wu, *Angew. Chem., Int. Ed.*, 2022, **12**, 2200586.
- 26 X. Song, S. Jia, L. Xu, J. Feng, L. He, X. Sun and B. Han, *Mater. Today Sustain.*, 2022, **19**, 100179.
- 27 S. Bhunia, G. G. Pawar, S. V. Kumar, Y. Jiang and D. Ma, *Angew. Chem., Int. Ed.*, 2017, **56**, 16136–16179.
- 28 C. Tang, Y. Zheng, M. Jaroniec and S.-Z. Qiao, *Angew. Chem., Int. Ed.*, 2021, **60**, 19572–19590.
- 29 J. Li, Y. Zhang, K. Kuruvinashetti and N. Kornienko, *Nat. Rev. Chem.*, 2022, **6**, 303–319.
- 30 Z. Tao, C. L. Rooney, Y. Liang and H. Wang, *J. Am. Chem. Soc.*, 2021, **143**, 19630–19642.
- 31 M. Jouny, J. J. Lv, T. Cheng, B. H. Ko, J. J. Zhu, W. A. Goddard, 3rd and F. Jiao, *Nat. Chem.*, 2019, **11**, 846–851.
- 32 C. Chen, X. Zhu, X. Wen, Y. Zhou, L. Zhou, H. Li, L. Tao, Q. Li, S. Du, T. Liu, D. Yan, C. Xie, Y. Zou, Y. Wang, R. Chen, J. Huo, Y. Li, J. Cheng, H. Su, X. Zhao, W. Cheng, Q. Liu, H. Lin, J. Luo, J. Chen, M. Dong, K. Cheng, C. Li and S. Wang, *Nat. Chem.*, 2020, **12**, 717–724.
- 33 P. G. de Gennes and L. Leger, *Annu. Rev. Phys. Chem.*, 1982, **33**, 49–61.
- 34 N. Cao, Y. Quan, A. Guan, C. Yang, Y. Ji, L. Zhang and G. Zheng, *J. Colloid Interface Sci.*, 2020, **577**, 109–114.
- 35 Y. Feng, H. Yang, Y. Zhang, X. Huang, L. Li, T. Cheng and Q. Shao, *Nano Lett.*, 2020, **20**, 8282–8289.
- 36 C. Lv, L. Zhong, H. Liu, Z. Fang, C. Yan, M. Chen, Y. Kong, C. Lee, D. Liu, S. Li, J. Liu, L. Song, G. Chen, Q. Yan and G. Yu, *Nat. Sustain.*, 2021, **4**, 868–876.
- 37 L. Li, C. Tang, H. Jin, K. Davey and S.-Z. Qiao, *Chem.*, 2021, **7**, 3232–3255.
- 38 T. Ren, K. Ren, M. Wang, M. Liu, Z. Wang, H. Wang, X. Li, L. Wang and Y. Xu, *Chem. Eng. J.*, 2021, **426**, 130759.
- 39 S. L. Fischer and C. P. Koshland, *Environ. Sci. Technol.*, 2007, **41**, 3121–3126.
- 40 Z. Sabeti, K. Ansarin, E. Seyedrezazadeh, M. A. Jafarabadi, V. Safari, S. Dastgiri, M. Shakerkhatabi, A. Gholampour, Z. Khamnian, M. Sepehri, M. Dahim, J. Sharbafi and D. Hakimi, *Environ. Pollut.*, 2021, **288**, 117797.
- 41 Y. Zhong, H. Xiong, J. Low, R. Long and Y. Xiong, *eScience*, 2022, DOI: [10.1016/j.esci.2022.11.002](https://doi.org/10.1016/j.esci.2022.11.002).
- 42 S. Liu, M. Wang, Q. Cheng, Y. He, J. Ni, J. Liu, C. Yan and T. Qian, *ACS Nano*, 2022, **16**, 17911–17930.
- 43 J. Fu, Y. Yang and J.-S. Hu, *ACS Mater. Lett.*, 2021, **3**, 1468–1476.
- 44 C. Chen, N. He and S. Wang, *Small Sci.*, 2021, **1**, 2100070.
- 45 J. C. Siu, N. Fu and S. Lin, *Acc. Chem. Res.*, 2020, **53**, 547–560.
- 46 R. Francke and R. D. Little, *Chem. Soc. Rev.*, 2014, **43**, 2492–2521.
- 47 D. Pletcher, R. A. Green and R. C. D. Brown, *Chem. Rev.*, 2018, **118**, 4573–4591.

- 48 D. M. Heard and A. J. J. Lennox, *Angew. Chem., Int. Ed.*, 2020, **59**, 18866–18884.
- 49 R. Francke, *Chimia*, 2020, **74**, 49–56.
- 50 B. A. Frontana-Uribe, R. D. Little, J. G. Ibanez, A. Palma and R. Vasquez-Medrano, *Green Chem.*, 2010, **12**, 2099.
- 51 A. Wiebe, T. Gieshoff, S. Möhle, E. Rodrigo, M. Zirbes and S. R. Waldvogel, *Angew. Chem., Int. Ed.*, 2018, **57**, 5594–5619.
- 52 I. Sires, E. Brilllas, M. A. Oturan, M. A. Rodrigo and M. Panizza, *Environ. Sci. Pollut. Res.*, 2014, **21**, 8336–8367.
- 53 W. Ju, A. Bagger, G. P. Hao, A. S. Varela, I. Sinev, V. Bon, B. Roldan Cuenya, S. Kaskel, J. Rossmeisl and P. Strasser, *Nat. Commun.*, 2017, **8**, 944.
- 54 K. Jiang, R. B. Sandberg, A. J. Akey, X. Liu, D. C. Bell, J. K. Nørskov, K. Chan and H. Wang, *Nat. Catal.*, 2018, **1**, 111–119.
- 55 D. Gao, I. T. McCrum, S. Deo, Y.-W. Choi, F. Scholten, W. Wan, J. G. Chen, M. J. Janik and B. Roldan Cuenya, *ACS Catal.*, 2018, **8**, 10012–10020.
- 56 L. Lu, X. Sun, J. Ma, D. Yang, H. Wu, B. Zhang, J. Zhang and B. Han, *Angew. Chem., Int. Ed.*, 2018, **57**, 14149–14153.
- 57 T. Cheng, H. Xiao and W. A. Goddard, 3rd, *Proc. Natl. Acad. Sci. U. S. A.*, 2017, **114**, 1795–1800.
- 58 H. Xiao, W. A. Goddard, 3rd, T. Cheng and Y. Liu, *Proc. Natl. Acad. Sci. U. S. A.*, 2017, **114**, 6685–6688.
- 59 A. M. Limaye, J. S. Zeng, A. P. Willard and K. Manthiram, *Nat. Commun.*, 2021, **12**, 703.
- 60 H. Xiao, T. Cheng and W. A. Goddard, *J. Am. Chem. Soc.*, 2016, **139**, 130–136.
- 61 Y.-H. Fang and Z.-P. Liu, *ACS Catal.*, 2014, **4**, 4364–4376.
- 62 T. Shinagawa, A. T. Garcia-Esparza and K. Takanabe, *Sci. Rep.*, 2015, **5**, 13801.
- 63 A. T. Marshall and L. Vaisson-Béthune, *Electrochem. Commun.*, 2015, **61**, 23–26.
- 64 Y. Zhao, M. Luo, S. Chu, M. Peng, B. Liu, Q. Wu, P. Liu, F. M. F. de Groot and Y. Tan, *Nano Energy*, 2019, **59**, 146–153.
- 65 Q. Lu, J. Rosen, Y. Zhou, G. S. Hutchings, Y. C. Kimmel, J. G. Chen and F. Jiao, *Nat. Commun.*, 2014, **5**, 3242.
- 66 M. Boudart, *Chem. Rev.*, 1995, **95**, 661–666.
- 67 C. Costentin, S. Drouet, M. Robert and J. M. Saveant, *J. Am. Chem. Soc.*, 2012, **134**, 11235–11242.
- 68 C. Zhao, X. Dai, T. Yao, W. Chen, X. Wang, J. Wang, J. Yang, S. Wei, Y. Wu and Y. Li, *J. Am. Chem. Soc.*, 2017, **139**, 8078–8081.
- 69 Y. Pan, R. Lin, Y. Chen, S. Liu, W. Zhu, X. Cao, W. Chen, K. Wu, W. C. Cheong, Y. Wang, L. Zheng, J. Luo, Y. Lin, Y. Liu, C. Liu, J. Li, Q. Lu, X. Chen, D. Wang, Q. Peng, C. Chen and Y. Li, *J. Am. Chem. Soc.*, 2018, **140**, 4218–4221.
- 70 H. B. Yang, S.-F. Hung, S. Liu, K. Yuan, S. Miao, L. Zhang, X. Huang, H.-Y. Wang, W. Cai, R. Chen, J. Gao, X. Yang, W. Chen, Y. Huang, H. M. Chen, C. M. Li, T. Zhang and B. Liu, *Nat. Energy*, 2018, **3**, 140–147.
- 71 R. Wang, X. Wang, W. Weng, Y. Yao, P. Kidkhunthod, C. Wang, Y. Hou and J. Guo, *Angew. Chem., Int. Ed.*, 2022, **61**, 202115503.
- 72 D. Voiry, H. Yamaguchi, J. Li, R. Silva, D. C. Alves, T. Fujita, M. Chen, T. Asefa, V. B. Shenoy, G. Eda and M. Chhowalla, *Nat. Mater.*, 2013, **12**, 850–855.
- 73 J. Kibsgaard, T. F. Jaramillo and F. Besenbacher, *Nat. Chem.*, 2014, **6**, 248–253.
- 74 H. Li, C. Tsai, A. L. Koh, L. Cai, A. W. Contryman, A. H. Fragapane, J. Zhao, H. S. Han, H. C. Manoharan, F. Abild-Pedersen, J. K. Norskov and X. Zheng, *Nat. Mater.*, 2016, **15**, 364.
- 75 Y. Yan, X. Ge, Z. Liu, J. Y. Wang, J. M. Lee and X. Wang, *Nanoscale*, 2013, **5**, 7768–7771.
- 76 D. Mukherjee, P. M. Austeria and S. Sampath, *ACS Energy Lett.*, 2016, **1**, 367–372.
- 77 X. Kang, Q. Zhu, X. Sun, J. Hu, J. Zhang, Z. Liu and B. Han, *Chem. Sci.*, 2016, **7**, 266–273.
- 78 S. Ma, M. Sadakiyo, R. Luo, M. Heima, M. Yamauchi and P. J. A. Kenis, *J. Power Sources*, 2016, **301**, 219–228.
- 79 M. B. Ross, P. De Luna, Y. Li, C.-T. Dinh, D. Kim, P. Yang and E. H. Sargent, *Nat. Catal.*, 2019, **2**, 648–658.
- 80 G. Wang, J. Chen, Y. Ding, P. Cai, L. Yi, Y. Li, C. Tu, Y. Hou, Z. Wen and L. Dai, *Chem. Soc. Rev.*, 2021, **50**, 4993–5061.
- 81 X. Lu, Y. Wu, X. Yuan, L. Huang, Z. Wu, J. Xuan, Y. Wang and H. Wang, *ACS Energy Lett.*, 2018, **3**, 2527–2532.
- 82 J. J. Lv, M. Jouny, W. Luc, W. Zhu, J. J. Zhu and F. Jiao, *Adv. Mater.*, 2018, **30**, 1803111.
- 83 Z. Z. Niu, F. Y. Gao, X. L. Zhang, P. P. Yang, R. Liu, L. P. Chi, Z. Z. Wu, S. Qin, X. Yu and M. R. Gao, *J. Am. Chem. Soc.*, 2021, **143**, 8011–8021.
- 84 S. Ren, D. Joulié, D. Salvatore, K. Torbensen, M. Wang, M. Robert and C. P. Berlinguet, *Science*, 2019, **365**, 367–369.
- 85 Z.-Z. Niu, L.-P. Chi, R. Liu, Z. Chen and M.-R. Gao, *Energy Environ. Sci.*, 2021, **14**, 4169–4176.
- 86 K. Liu, W. A. Smith and T. Burdyny, *ACS Energy Lett.*, 2019, **4**, 639–643.
- 87 B. Hasa, M. Jouny, B. H. Ko, B. Xu and F. Jiao, *Angew. Chem., Int. Ed.*, 2021, **60**, 3277–3282.
- 88 M. Lorin, *Chem. News J. Phys. Sci.*, 1864, **IX**, 291.
- 89 D. S. Ripatti, T. R. Veltman and M. W. Kanan, *Joule*, 2019, **3**, 240–256.
- 90 Q. Gong, P. Ding, M. Xu, X. Zhu, M. Wang, J. Deng, Q. Ma, N. Han, Y. Zhu, J. Lu, Z. Feng, Y. Li, W. Zhou and Y. Li, *Nat. Commun.*, 2019, **10**, 2807.
- 91 E. Jeng and F. Jiao, *React. Chem. Eng.*, 2020, **5**, 1768–1775.
- 92 Y. Luo, K. Zhang, Y. Li and Y. Wang, *InfoMat*, 2021, **3**, 1313–1332.
- 93 T. N. Nguyen and C. T. Dinh, *Chem. Soc. Rev.*, 2020, **49**, 7488–7504.
- 94 F. Xiao, Y. C. Wang, Z. P. Wu, G. Chen, F. Yang, S. Zhu, K. Siddharth, Z. Kong, A. Lu, J. C. Li, C. J. Zhong, Z. Y. Zhou and M. Shao, *Adv. Mater.*, 2021, **33**, 2006292.
- 95 Y. He, S. Liu, C. Priest, Q. Shi and G. Wu, *Chem. Soc. Rev.*, 2020, **49**, 3484–3524.
- 96 M. Uchida, Y. Aoyama, N. Eda and A. Ohta, *J. Electrochem. Soc.*, 1995, **142**, 463–468.
- 97 L.-C. Weng, A. T. Bell and A. Z. Weber, *Energy Environ. Sci.*, 2019, **12**, 1950–1968.

- 98 D. Kim, W. Choi, H. W. Lee, S. Y. Lee, Y. Choi, D. K. Lee, W. Kim, J. Na, U. Lee, Y. J. Hwang and D. H. Won, *ACS Energy Lett.*, 2021, **6**, 3488–3495.
- 99 T. Lazaridis, B. M. Stühmeier, H. A. Gasteiger and H. A. El-Sayed, *Nat. Catal.*, 2022, **5**, 363–373.
- 100 C.-T. Dinh, T. Burdyny, M. G. Kibria, A. Seifitokaldani, C. M. Gabardo, F. P. García de Arquer, A. Kiani, J. P. Edwards, P. De Luna, O. S. Bushuyev, C. Zou, R. Quintero-Bermudez, Y. Pang, D. Sinton and E. H. Sargent, *Science*, 2018, **360**, 783.
- 101 S. Verma, X. Lu, S. Ma, R. I. Masel and P. J. Kenis, *Phys. Chem. Chem. Phys.*, 2016, **18**, 7075–7084.
- 102 L. Ge, H. Rabiee, M. Li, S. Subramanian, Y. Zheng, J. H. Lee, T. Burdyny and H. Wang, *Chem.*, 2022, **8**, 663–692.
- 103 L. F. Greenlee, J. N. Renner and S. L. Foster, *ACS Catal.*, 2018, **8**, 7820–7827.
- 104 L. Zhou and C. E. Boyd, *Aquaculture*, 2016, **450**, 187–193.
- 105 X. Peng, Y. Mi, H. Bao, Y. Liu, D. Qi, Y. Qiu, L. Zhuo, S. Zhao, J. Sun, X. Tang, J. Luo and X. Liu, *Nano Energy*, 2020, **78**, 105321.
- 106 I. K. Phelps and C. D. Deming, *Chem. News J. Phys. Sci.*, 1908, **97**, 86–87.
- 107 J. Long, S. Chen, Y. Zhang, C. Guo, X. Fu, D. Deng and J. Xiao, *Angew. Chem., Int. Ed.*, 2020, **59**, 9711–9718.
- 108 H. Wang, L. Wang, Q. Wang, S. Ye, W. Sun, Y. Shao, Z. Jiang, Q. Qiao, Y. Zhu, P. Song, D. Li, L. He, X. Zhang, J. Yuan, T. Wu and G. A. Ozin, *Angew. Chem., Int. Ed.*, 2018, **57**, 12360–12364.
- 109 Z. Geng, Y. Liu, X. Kong, P. Li, K. Li, Z. Liu, J. Du, M. Shu, R. Si and J. Zeng, *Adv. Mater.*, 2018, **30**, e1803498.
- 110 H. Tao, C. Choi, L.-X. Ding, Z. Jiang, Z. Han, M. Jia, Q. Fan, Y. Gao, H. Wang, A. W. Robertson, S. Hong, Y. Jung, S. Liu and Z. Sun, *Chem.*, 2019, **5**, 204–214.
- 111 C. Tsounis, R. Kuriki, K. Shibata, J. J. M. Vequizo, D. Lu, A. Yamakata, O. Ishitani, R. Amal and K. Maeda, *ACS Sustainable Chem. Eng.*, 2018, **6**, 15333–15340.
- 112 B. H. R. Suryanto, H.-L. Du, D. Wang, J. Chen, A. N. Simonov and D. R. MacFarlane, *Nat. Catal.*, 2019, **2**, 290–296.
- 113 S. Z. Andersen, V. Čolić, S. Yang, J. A. Schwalbe, A. C. Nielander, J. M. McEnaney, K. Enemark-Rasmussen, J. G. Baker, A. R. Singh, B. A. Rohr, M. J. Statt, S. J. Blair, S. Mezzavilla, J. Kibsgaard, P. C. K. Vesborg, M. Cargnello, S. F. Bent, T. F. Jaramillo, I. E. L. Stephens, J. K. Nørskov and I. Chorkendorff, *Nature*, 2019, **570**, 504–508.
- 114 R. Francke, B. Schille and M. Roemelt, *Chem. Rev.*, 2018, **118**, 4631–4701.
- 115 J. Wu, Y. Huang, W. Ye and Y. Li, *Adv. Sci.*, 2017, **4**, 1700194.
- 116 A. M. Appel, J. E. Bercaw, A. B. Bocarsly, H. Dobbek, D. L. DuBois, M. Dupuis, J. G. Ferry, E. Fujita, R. Hille, P. J. Kenis, C. A. Kerfeld, R. H. Morris, C. H. Peden, A. R. Portis, S. W. Ragsdale, T. B. Rauchfuss, J. N. Reek, L. C. Seefeldt, R. K. Thauer and G. L. Waldrop, *Chem. Rev.*, 2013, **113**, 6621–6658.
- 117 W. Wang, S. Wang, X. Ma and J. Gong, *Chem. Soc. Rev.*, 2011, **40**, 3703–3727.
- 118 K. P. Kuhl, E. R. Cave, D. N. Abram and T. F. Jaramillo, *Energy Environ. Sci.*, 2012, **5**, 7050–7059.
- 119 X. Chang, T. Wang and J. Gong, *Energy Environ. Sci.*, 2016, **9**, 2177–2196.
- 120 T. Wang, X. Sang, W. Zheng, B. Yang, S. Yao, C. Lei, Z. Li, Q. He, J. Lu, L. Lei, L. Dai and Y. Hou, *Adv. Mater.*, 2020, **32**, 2002430.
- 121 X. Wang, Y. Wang, X. Sang, W. Zheng, S. Zhang, L. Shuai, B. Yang, Z. Li, J. Chen, L. Lei, N. M. Adli, M. K. H. Leung, M. Qiu, G. Wu and Y. Hou, *Angew. Chem., Int. Ed.*, 2021, **60**, 4192–4198.
- 122 J. Chen, Z. Li, X. Wang, X. Sang, S. Zheng, S. Liu, B. Yang, Q. Zhang, L. Lei, L. Dai and Y. Hou, *Angew. Chem., Int. Ed.*, 2022, **61**, 202111683.
- 123 L. Wang, Z. Li, K. Wang, Q. Dai, C. Lei, B. Yang, Q. Zhang, L. Lei, M. K. H. Leung and Y. Hou, *Nano Energy*, 2020, **74**, 104850.
- 124 W. Zheng, F. Chen, Q. Zeng, Z. Li, B. Yang, L. Lei, Q. Zhang, F. He, X. Wu and Y. Hou, *Nano-Micro Lett.*, 2020, **12**, 108.
- 125 Y. Ye, H. Yang, J. Qian, H. Su, K. J. Lee, T. Cheng, H. Xiao, J. Yano, W. A. Goddard, 3rd and E. J. Crumlin, *Nat. Commun.*, 2019, **10**, 1875.
- 126 A. Alvarez, M. Borges, J. J. Corral-Perez, J. G. Olcina, L. Hu, D. Cornu, R. Huang, D. Stoian and A. Urakawa, *ChemPhysChem*, 2017, **18**, 3135–3141.
- 127 H. A. E. Omr, M. W. Horn and H. Lee, *Catalysts*, 2021, **11**, 418.
- 128 L. Zhang, Z. J. Zhao and J. Gong, *Angew. Chem., Int. Ed.*, 2017, **56**, 11326–11353.
- 129 G. Wen, B. Ren, Y. Zheng, M. Li, C. Silva, S. Song, Z. Zhang, H. Dou, L. Zhao, D. Luo, A. Yu and Z. Chen, *Adv. Energy Mater.*, 2021, **12**, 2103289.
- 130 Q. Fan, M. Zhang, M. Jia, S. Liu, J. Qiu and Z. Sun, *Mater. Today Energy*, 2018, **10**, 280–301.
- 131 Q. Wang, Y. Lei, D. Wang and Y. Li, *Energy Environ. Sci.*, 2019, **12**, 1730–1750.
- 132 S. Jin, Z. Hao, K. Zhang, Z. Yan and J. Chen, *Angew. Chem., Int. Ed.*, 2021, **60**, 20627–20648.
- 133 D. D. Zhu, J. L. Liu and S. Z. Qiao, *Adv. Mater.*, 2016, **28**, 3423–3452.
- 134 R. Kortlever, J. Shen, K. J. Schouten, F. Calle-Vallejo and M. T. Koper, *J. Phys. Chem. Lett.*, 2015, **6**, 4073–4082.
- 135 X. Zheng, P. De Luna, F. P. García de Arquer, B. Zhang, N. Becknell, M. B. Ross, Y. Li, M. N. Banis, Y. Li, M. Liu, O. Voznyy, C. T. Dinh, T. Zhuang, P. Stadler, Y. Cui, X. Du, P. Yang and E. H. Sargent, *Joule*, 2017, **1**, 794–805.
- 136 I. V. Chernyshova, P. Somasundaran and S. Ponnurangam, *Proc. Natl. Acad. Sci. U. S. A.*, 2018, **115**, E9261–E9270.
- 137 Z. Li, A. Cao, Q. Zheng, Y. Fu, T. Wang, K. T. Arul, J. L. Chen, B. Yang, N. M. Adli, L. Lei, C. L. Dong, J. Xiao, G. Wu and Y. Hou, *Adv. Mater.*, 2021, **33**, 2005113.
- 138 T. Wang, X. Sang, W. Zheng, B. Yang, S. Yao, C. Lei, Z. Li, Q. He, J. Lu, L. Lei, L. Dai and Y. Hou, *Adv. Mater.*, 2020, **32**, 2002430.

- 139 J. Chen, T. Wang, X. Wang, B. Yang, X. Sang, S. Zheng, S. Yao, Z. Li, Q. Zhang, L. Lei, J. Xu, L. Dai and Y. Hou, *Adv. Funct. Mater.*, 2022, **32**, 2110174.
- 140 X. Wang, S. Feng, W. Lu, Y. Zhao, S. Zheng, W. Zheng, X. Sang, L. Zheng, Y. Xie, Z. Li, B. Yang, L. Lei, S. Wang and Y. Hou, *Adv. Funct. Mater.*, 2021, **31**, 2104243.
- 141 Y. Zhang, X. Wang, S. Zheng, B. Yang, Z. Li, J. Lu, Q. Zhang, N. M. Adli, L. Lei, G. Wu and Y. Hou, *Adv. Funct. Mater.*, 2021, **31**, 2104377.
- 142 W. Zheng, Y. Wang, L. Shuai, X. Wang, F. He, C. Lei, Z. Li, B. Yang, L. Lei, C. Yuan, M. Qiu, Y. Hou and X. Feng, *Adv. Funct. Mater.*, 2021, **31**, 2008146.
- 143 A. E. Shilov, *Russ. Chem. Bull.*, 2003, **52**, 2555–2562.
- 144 X. Cui, C. Tang and Q. Zhang, *Adv. Energy Mater.*, 2018, **8**, 1800369.
- 145 C.-G. Zhan, J. A. Nichols and D. A. Dixon, *J. Phys. Chem. A*, 2003, **107**, 4184–4195.
- 146 A. R. Singh, B. A. Rohr, J. A. Schwalbe, M. Cargnello, K. Chan, T. F. Jaramillo, I. Chorkendorff and J. K. Nørskov, *ACS Catal.*, 2017, **7**, 706–709.
- 147 C. J. M. van der Ham, M. T. M. Koper and D. G. H. Hetterscheid, *Chem. Soc. Rev.*, 2014, **43**, 5183–5191.
- 148 L. Shi, Y. Yin, S. Wang and H. Sun, *ACS Catal.*, 2020, **10**, 6870–6899.
- 149 Y. Kong, Y. Li, X. Sang, B. Yang, Z. Li, S. Zheng, Q. Zhang, S. Yao, X. Yang, L. Lei, S. Zhou, G. Wu and Y. Hou, *Adv. Mater.*, 2022, **34**, 2103548.
- 150 Y. Li, Y. Ji, Y. Zhao, J. Chen, S. Zheng, X. Sang, B. Yang, Z. Li, L. Lei, Z. Wen, X. Feng and Y. Hou, *Adv. Mater.*, 2022, **34**, 2202240.
- 151 Y. Kong, L. Wu, X. Yang, Y. Li, S. Zheng, B. Yang, Z. Li, Q. Zhang, S. Zhou, L. Lei, G. Wu and Y. Hou, *Adv. Funct. Mater.*, 2022, **n/a**, 2205409.
- 152 Y. Li, J. Li, J. Huang, J. Chen, Y. Kong, B. Yang, Z. Li, L. Lei, G. Chai, Z. Wen, L. Dai and Y. Hou, *Angew. Chem., Int. Ed.*, 2021, **60**, 9078–9085.
- 153 H. Wang, Z. Li, Y. Li, B. Yang, J. Chen, L. Lei, S. Wang and Y. Hou, *Nano Energy*, 2021, **81**, 105613.
- 154 Y. Tanabe and Y. Nishibayashi, *Coord. Chem. Rev.*, 2013, **257**, 2551–2564.
- 155 Y. Ren, C. Yu, X. Tan, Q. Wei, Z. Wang, L. Ni, L. Wang and J. Qiu, *Energy Environ. Sci.*, 2022, **15**, 2776–2805.
- 156 Z. Han, P. Wu, M. He, X. Zhuang, H. Lin and S. Han, *J. Energy Storage*, 2022, **55**, 105684.
- 157 L. Zhang, G.-F. Chen, L.-X. Ding and H. Wang, *Chem. – Eur. J.*, 2019, **25**, 12464–12485.
- 158 H. Shen, C. Choi, J. Masa, X. Li, J. Qiu, Y. Jung and Z. Sun, *Chem.*, 2021, **7**, 1708–1754.
- 159 F. Jiao and B. Xu, *Adv. Mater.*, 2019, **31**, 1805173.
- 160 L. Li, C. Tang, D. Yao, Y. Zheng and S. Z. Qiao, *ACS Energy Lett.*, 2019, **4**, 2111–2116.
- 161 X. Liu, Y. Jiao, Y. Zheng, M. Jaroniec and S. Z. Qiao, *J. Am. Chem. Soc.*, 2019, **141**, 9664–9672.
- 162 Y. Huang, D. D. Babu, Z. Peng and Y. Wang, *Adv. Sci.*, 2020, **7**, 1902390.
- 163 S. B. Patil and D. Y. Wang, *Small*, 2020, **16**, 2002885.
- 164 Q. Wang, Y. Lei, D. Wang and Y. Li, *Energy Environ. Sci.*, 2019, **12**, 1730–1750.
- 165 G. Ertl, *Angew. Chem., Int. Ed.*, 2008, **47**, 3524–3535.
- 166 H.-P. Jia and E. A. Quadrelli, *Chem. Soc. Rev.*, 2014, **43**, 547–564.
- 167 T. H. Rod, A. Logadottir and J. K. Nørskov, *J. Chem. Phys.*, 2000, **112**, 5343–5347.
- 168 L. Wang, M. Xia, H. Wang, K. Huang, C. Qian, C. T. Maravelias and G. A. Ozin, *Joule*, 2018, **2**, 1055–1074.
- 169 J. Deng, J. A. Igínez and C. Liu, *Joule*, 2018, **2**, 846–856.
- 170 G. Jones, T. Bligaard, F. Abild-Pedersen and J. K. Nørskov, *J. Phys.: Condens. Matter*, 2008, **20**, 064239.
- 171 A. J. Gottle and M. T. M. Koper, *Chem. Sci.*, 2017, **8**, 458–465.
- 172 C. V. S. Kumar and V. Subramanian, *Phys. Chem. Chem. Phys.*, 2017, **19**, 15377–15387.
- 173 Y. Wan, J. Xu and R. Lv, *Mater. Today*, 2019, **27**, 69–90.
- 174 S. L. Foster, S. I. P. Bakovic, R. D. Duda, S. Maheshwari, R. D. Milton, S. D. Minteer, M. J. Janik, J. N. Renner and L. F. Greenlee, *Nat. Catal.*, 2018, **1**, 490–500.
- 175 A. L. Garden and E. Skúlason, *J. Phys. Chem. C*, 2015, **119**, 26554–26559.
- 176 M. A. Shipman and M. D. Symes, *Catal. Today*, 2017, **286**, 57–68.
- 177 S. Hand and R. D. Cusick, *Environ. Sci.: Water Res. Technol.*, 2020, **6**, 925–934.
- 178 H. I. Uzun and E. Debik, *Sep. Purif. Technol.*, 2019, **209**, 776–781.
- 179 S. Garcia-Segura, M. Lanzarini-Lopes, K. Hristovski and P. Westerhoff, *Appl. Catal., B*, 2018, **236**, 546–568.
- 180 H. O. Tugaoen, S. Garcia-Segura, K. Hristovski and P. Westerhoff, *Sci. Total Environ.*, 2017, **599–600**, 1524–1551.
- 181 A. R. Cook, N. Dimitrijevic, B. W. Dreyfus, D. Meisel, L. A. Curtiss and D. M. Camaioni, *J. Phys. Chem. A*, 2001, **105**, 3658–3666.
- 182 V. N. Montesinos, N. Quici, H. Destaillats and M. I. Litter, *RSC Adv.*, 2015, **5**, 85319–85322.
- 183 M. T. de Groot and M. T. M. Koper, *J. Electroanal. Chem.*, 2004, **562**, 81–94.
- 184 K. J. Vetter, *Zeitschrift für Elektrochemie, Berichte der Bunsengesellschaft für physikalische Chemie*, 1959, **63**, 1189–1191.
- 185 G. Schmid, *Zeitschrift für Elektrochemie, Berichte der Bunsengesellschaft für physikalische Chemie*, 1961, **65**, 531–534.
- 186 G. Schmid, *Zeitschrift für Elektrochemie, Berichte der Bunsengesellschaft für physikalische Chemie*, 1959, **63**, 1183–1188.
- 187 K. Y. Lee, D. J. Kuchynka and J. K. Kochi, *Inorg. Chem.*, 1990, **29**, 4196–4204.
- 188 O. W. J. S. Rutten, A. V. Sandwijk and G. V. Weert, *J. Appl. Electrochem.*, 1999, **29**, 87–92.
- 189 M. Dortsiou and G. Kyriacou, *J. Electroanal. Chem.*, 2009, **630**, 69–74.
- 190 F. Balbaud, G. Sanchez, G. Santarini and G. Picard, *Eur. J. Inorg. Chem.*, 1999, 277–285.

- 191 J. Zheng, T. Lu, T. M. Cotton and G. Chumanov, *J. Phys. Chem. B*, 1999, **103**, 6567–6572.
- 192 S. Goldstein, D. Behar, T. Rajh and J. Rabani, *J. Phys. Chem. A*, 2016, **120**, 2307–2312.
- 193 J. F. Su, I. Ruzybayev, I. Shah and C. P. Huang, *Appl. Catal., B*, 2016, **180**, 199–209.
- 194 T. Yoshioka, K. Iwase, S. Nakanishi, K. Hashimoto and K. Kamiya, *J. Phys. Chem. C*, 2016, **120**, 15729–15734.
- 195 A. S. Dutton, J. M. Fukuto and K. N. Houk, *Inorg. Chem.*, 2005, **44**, 4024–4028.
- 196 A. C. A. de Vooys, G. L. Beltramo, B. van Riet, J. A. R. van Veen and M. T. M. Koper, *Electrochim. Acta*, 2004, **49**, 1307–1314.
- 197 J. A. Colucci, M. J. Foral and S. H. Langer, *Electrochim. Acta*, 1985, **30**, 521–528.
- 198 A. Clayborne, H.-J. Chun, R. B. Rankin and J. Greeley, *Angew. Chem., Int. Ed.*, 2015, **54**, 8255–8258.
- 199 A. C. A. de Vooys, M. T. M. Koper, R. A. van Santen and J. A. R. van Veen, *J. Catal.*, 2001, **202**, 387–394.
- 200 I. Katsounaras and G. Kyriacou, *Electrochim. Acta*, 2008, **53**, 5477–5484.
- 201 E. Lacasa, P. Cañizares, J. Llanos and M. A. Rodrigo, *J. Hazard. Mater.*, 2012, **213–214**, 478–484.
- 202 J. F. E. Gootzen, P. G. J. M. Peeters, J. M. B. Dukers, L. Lefferts, W. Visscher and J. A. R. van Veen, *J. Electroanal. Chem.*, 1997, **434**, 171–183.
- 203 H. O’Neal Tugaoen, S. Garcia-Segura, K. Hristovski and P. Westerhoff, *Sci. Total Environ.*, 2018, **613–614**, 1331–1338.
- 204 G. Reginato, P. Sadler and R. D. Wilkes, *Org. Process Res. Dev.*, 2011, **15**, 1396–1405.
- 205 J. S. Carey, D. Laffan, C. Thomson and M. T. Williams, *Org. Biomol. Chem.*, 2006, **4**, 2337–2347.
- 206 S. D. Roughley and A. M. Jordan, *J. Med. Chem.*, 2011, **54**, 3451–3479.
- 207 S. H. Cho, J. Y. Kim, J. Kwak and S. Chang, *Chem. Soc. Rev.*, 2011, **40**, 5068–5083.
- 208 J. Bariwal and E. Van der Eycken, *Chem. Soc. Rev.*, 2013, **42**, 9283–9303.
- 209 J. Magano and J. R. Dunetz, *Chem. Rev.*, 2011, **111**, 2177–2250.
- 210 T. W. Cooper, I. B. Campbell and S. J. Macdonald, *Angew. Chem., Int. Ed.*, 2010, **49**, 8082–8091.
- 211 S. L. Buchwald, C. Mauger, G. Mignani and U. Scholz, *Adv. Synth. Catal.*, 2006, **348**, 23–39.
- 212 R. Hili and A. K. Yudin, *Nat. Chem. Biol.*, 2006, **2**, 284–287.
- 213 P. Ruiz-Castillo and S. L. Buchwald, *Chem. Rev.*, 2016, **116**, 12564–12649.
- 214 C. Sambiagio, S. P. Marsden, A. J. Blacker and P. C. McGowan, *Chem. Soc. Rev.*, 2014, **43**, 3525–3550.
- 215 Q. Shen, S. Shekhar, J. P. Stambuli and J. F. Hartwig, *Angew. Chem., Int. Ed.*, 2005, **44**, 1371–1375.
- 216 B. Gutmann, D. Cantillo and C. O. Kappe, *Angew. Chem., Int. Ed.*, 2015, **54**, 6688–6728.
- 217 N. Galaffu, S. P. Man, R. D. Wilkes and J. R. H. Wilson, *Org. Process Res. Dev.*, 2007, **11**, 406–413.
- 218 M. C. Leech and K. Lam, *Nat. Rev. Chem.*, 2022, **6**, 275–286.
- 219 M. Yuan, H. Zhang, Y. Xu, R. Liu, R. Wang, T. Zhao, J. Zhang, Z. Liu, H. He, C. Yang, S. Zhang and G. Zhang, *Chem. Catal.*, 2022, **2**, 309–320.
- 220 J. Li and N. Kornienko, *Chem. Sci.*, 2022, **13**, 3957–3964.
- 221 C. Guo, W. Zhou, X. Lan, Y. Wang, T. Li, S. Han, Y. Yu and B. Zhang, *J. Am. Chem. Soc.*, 2022, **144**, 16006–16011.
- 222 J. Shao, N. Meng, Y. Wang, B. Zhang, K. Yang, C. Liu, Y. Yu and B. Zhang, *Angew. Chem., Int. Ed.*, 2022, **61**, e202213009.
- 223 N. Meng, Y. Huang, Y. Liu, Y. Yu and B. Zhang, *Cell Rep. Phys. Sci.*, 2021, **2**, 100378.
- 224 S. Liu, S. Yin, Z. Wang, Y. Xu, X. Li, L. Wang and H. Wang, *Cell Rep. Phys. Sci.*, 2022, **3**, 100869.
- 225 M. Shibata and N. Furuya, *J. Electroanal. Chem.*, 2001, **507**, 177–184.
- 226 D. Saravananumar, J. Song, S. Lee, N. H. Hur and W. Shin, *ChemSusChem*, 2017, **10**, 3999–4003.
- 227 H. Wang, Y. Jiang, S. Li, F. Gou, X. Liu, Y. Jiang, W. Luo, W. Shen, R. He and M. Li, *Appl. Catal., B*, 2022, **318**, 121819.
- 228 X. Zhang, X. Zhu, S. Bo, C. Chen, M. Qiu, X. Wei, N. He, C. Xie, W. Chen, J. Zheng, P. Chen, S. P. Jiang, Y. Li, Q. Liu and S. Wang, *Nat. Commun.*, 2022, **13**, 5337.
- 229 C. Lv, C. Lee, L. Zhong, H. Liu, J. Liu, L. Yang, C. Yan, W. Yu, H. H. Hng, Z. Qi, L. Song, S. Li, K. P. Loh, Q. Yan and G. Yu, *ACS Nano*, 2022, **16**, 8213–8222.
- 230 X. Liu, P. V. Kumar, Q. Chen, L. Zhao, F. Ye, X. Ma, D. Liu, X. Chen, L. Dai and C. Hu, *Appl. Catal., B*, 2022, **316**, 121618.
- 231 J. Leverett, T. Tran-Phu, J. A. Yuwono, P. Kumar, C. Kim, Q. Zhai, C. Han, J. Qu, J. Cairney, A. N. Simonov, R. K. Hocking, L. Dai, R. Daiyan and R. Amal, *Adv. Energy Mater.*, 2022, **12**, 2201500.
- 232 Z. Tao, Y. Wu, Z. Wu, B. Shang, C. Rooney and H. Wang, *J. Energy Chem.*, 2022, **65**, 367–370.
- 233 X. Wei, X. Wen, Y. Liu, C. Chen, C. Xie, D. Wang, M. Qiu, N. He, P. Zhou, W. Chen, J. Cheng, H. Lin, J. Jia, X. Z. Fu and S. Wang, *J. Am. Chem. Soc.*, 2022, **144**, 11530–11535.
- 234 N. Meng, X. Ma, C. Wang, Y. Wang, R. Yang, J. Shao, Y. Huang, Y. Xu, B. Zhang and Y. Yu, *ACS Nano*, 2022, **16**, 9095–9104.
- 235 Y. Wu, Z. Jiang, Z. Lin, Y. Liang and H. Wang, *Nat. Sustain.*, 2021, **4**, 725–730.
- 236 M. Yuan, J. Chen, H. Zhang, Q. Li, L. Zhou, C. Yang, R. Liu, Z. Liu, S. Zhang and G. Zhang, *Energy Environ. Sci.*, 2022, **15**, 2084–2095.
- 237 M. Yuan, J. Chen, Y. Bai, Z. Liu, J. Zhang, T. Zhao, Q. Wang, S. Li, H. He and G. Zhang, *Angew. Chem., Int. Ed.*, 2021, **60**, 10910–10918.
- 238 M. Yuan, J. Chen, Y. Bai, Z. Liu, J. Zhang, T. Zhao, Q. Shi, S. Li, X. Wang and G. Zhang, *Chem. Sci.*, 2021, **12**, 6048–6058.
- 239 M. Yuan, J. Chen, Y. Xu, R. Liu, T. Zhao, J. Zhang, Z. Ren, Z. Liu, C. Streb, H. He, C. Yang, S. Zhang and G. Zhang, *Energy Environ. Sci.*, 2021, **14**, 6605–6615.
- 240 J. Meessen, *Chem. Ing. Tech.*, 2014, **86**, 2180–2189.

- 241 J. E. Kim, J. H. Jang, K. M. Lee, M. Balamurugan, Y. I. Jo, M. Y. Lee, S. Choi, S. W. Im and K. T. Nam, *Angew. Chem., Int. Ed.*, 2021, **60**, 21943–21951.
- 242 X. Liu, Y. Jiao, Y. Zheng, M. Jaroniec and S. Z. Qiao, *Nat. Commun.*, 2022, **13**, 5471.
- 243 M. Shibata, K. Yoshida and N. Furuya, *J. Electroanal. Chem.*, 1995, **387**, 143–145.
- 244 M. Shibata, K. Yoshida and N. Furuya, *Denki Kagaku oyobi Kogyo Butsuri Kagaku*, 1998, **66**, 584–589.
- 245 M. Shibata, K. Yoshida and N. Furuya, *J. Electrochem. Soc.*, 1998, **145**, 2348–2353.
- 246 M. Shibata, K. Yoshida and N. Furuya, *J. Electroanal. Chem.*, 1998, **442**, 67–72.
- 247 M. Shibata, K. Yoshida and N. Furuya, *J. Electrochem. Soc.*, 1998, **145**, 595–600.
- 248 M. Dunwell, Q. Lu, J. M. Heyes, J. Rosen, J. G. Chen, Y. Yan, F. Jiao and B. Xu, *J. Am. Chem. Soc.*, 2017, **139**, 3774–3783.
- 249 J. Y. Wang, H. X. Zhang, K. Jiang and W. B. Cai, *J. Am. Chem. Soc.*, 2011, **133**, 14876–14879.
- 250 M. Aresta, A. Dibenedetto and A. Angelini, *Chem. Rev.*, 2014, **114**, 1709–1742.
- 251 F. Barzagli, F. Mani and M. Peruzzini, *Green Chem.*, 2011, **13**, 1267.
- 252 D. B. Kayan and F. Köleli, *Appl. Catal., B*, 2016, **181**, 88–93.
- 253 M. Pérez-Fortes, A. Bocin-Dumitriu and E. Tzimas, *Energy Proc.*, 2014, **63**, 7968–7975.
- 254 G. F. Chen, S. Ren, L. Zhang, H. Cheng, Y. Luo, K. Zhu, L. X. Ding and H. Wang, *Small Methods*, 2018, **3**, 1800337.
- 255 M. Alfian and W. W. Purwanto, *Energy Sci. Eng.*, 2019, **7**, 292–304.
- 256 M. Appl, *Ullmann's Encyclopedia of Industrial Chemistry*, DOI: [10.1002/14356007.a02\\_143.pub2](https://doi.org/10.1002/14356007.a02_143.pub2).
- 257 J. H. Meessen, *Ullmann's Encyclopedia of Industrial Chemistry*, DOI: [10.1002/14356007.a27\\_333.pub2](https://doi.org/10.1002/14356007.a27_333.pub2).
- 258 M. Rahmatullah and T. R. C. Boyde, *Clin. Chim. Acta*, 1980, **107**, 3–9.
- 259 C. Chen, D. Yan, Y. Wang, Y. Zhou, Y. Zou, Y. Li and S. Wang, *Small*, 2019, **15**, 1805029.
- 260 G. W. Watt and J. D. Chriss, *Anal. Chem.*, 1952, **24**, 2006–2008.
- 261 Y.-C. Hao, Y. Guo, L.-W. Chen, M. Shu, X.-Y. Wang, T.-A. Bu, W.-Y. Gao, N. Zhang, X. Su, X. Feng, J.-W. Zhou, B. Wang, C.-W. Hu, A.-X. Yin, R. Si, Y.-W. Zhang and C.-H. Yan, *Nat. Catal.*, 2019, **2**, 448–456.
- 262 W. Zhang, Y. Yang, B. Huang, F. Lv, K. Wang, N. Li, M. Luo, Y. Chao, Y. Li, Y. Sun, Z. Xu, Y. Qin, W. Yang, J. Zhou, Y. Du, D. Su and S. Guo, *Adv. Mater.*, 2019, **31**, 1805833.
- 263 R. L. Melen, *Angew. Chem., Int. Ed.*, 2018, **57**, 880–882.
- 264 D. W. Stephan, *J. Am. Chem. Soc.*, 2015, **137**, 10018–10032.
- 265 D. W. Stephan and G. Erker, *Angew. Chem., Int. Ed.*, 2015, **54**, 6400–6441.
- 266 J. Liu, G. Chen, Y. Yu, Y. Wu, M. Zhou, W. Zhang, H. Qin, C. Lv and W. Fu, *New J. Chem.*, 2015, **39**, 1930–1937.
- 267 Y. He, Q. He, L. Wang, C. Zhu, P. Golani, A. D. Handoko, X. Yu, C. Gao, M. Ding, X. Wang, F. Liu, Q. Zeng, P. Yu, S. Guo, B. I. Yakobson, L. Wang, Z. W. Seh, Z. Zhang, M. Wu, Q. J. Wang, H. Zhang and Z. Liu, *Nat. Mater.*, 2019, **18**, 1098–1104.
- 268 T. Yan, N. Li, L. Wang, W. Ran, P. N. Duchesne, L. Wan, N. T. Nguyen, L. Wang, M. Xia and G. A. Ozin, *Nat. Commun.*, 2020, **11**, 6095.
- 269 Y. Yao, S. Zhu, H. Wang, H. Li and M. Shao, *J. Am. Chem. Soc.*, 2018, **140**, 1496–1501.
- 270 H. Shin, S. Jung, S. Bae, W. Lee and H. Kim, *Environ. Sci. Technol.*, 2014, **48**, 12768–12774.
- 271 P. Siva, P. Prabu, M. Selvam, S. Karthik and V. Rajendran, *Ionics*, 2017, **23**, 1871–1878.
- 272 Y. Huang, R. Yang, C. Wang, N. Meng, Y. Shi, Y. Yu and B. Zhang, *ACS Energy Lett.*, 2021, **7**, 284–291.
- 273 Y. Wang, T. Li, Y. Yu and B. Zhang, *Angew. Chem., Int. Ed.*, 2022, **61**, e202115409.
- 274 C. L. Rooney, Y. Wu, Z. Tao and H. Wang, *J. Am. Chem. Soc.*, 2021, **143**, 19983–19991.
- 275 B. Kim, S. Ma, H.-R. Molly Jhong and P. J. A. Kenis, *Electrochim. Acta*, 2015, **166**, 271–276.
- 276 L. Wang, S. A. Nitopi, E. Bertheussen, M. Orazov, C. G. Morales-Guio, X. Liu, D. C. Higgins, K. Chan, J. K. Nørskov, C. Hahn and T. F. Jaramillo, *ACS Catal.*, 2018, **8**, 7445–7454.
- 277 F. Calle-Vallejo and M. T. Koper, *Angew. Chem., Int. Ed.*, 2013, **52**, 7282–72855.
- 278 L. Chen, C. Tang, Y. Zheng, K. K. Ostrikov and Y. Jiao, *Energy Fuel.*, 2022, **36**, 7213–7218.
- 279 H. Chen, A. D. Handoko, T. Wang, J. Qu, J. Xiao, X. Liu, D. Legut, Z. Wei Seh and Q. Zhang, *ChemSusChem*, 2020, **13**, 5690–5698.
- 280 Y. Luo, G.-F. Chen, L. Ding, X. Chen, L.-X. Ding and H. Wang, *Joule*, 2019, **3**, 279–289.
- 281 I. K. Phelps and C. D. Deming, *Am. J. Sci.*, 1907, **s4-24**, 173–175.
- 282 T. Kakumoto, K. Saito and A. Imamura, *J. Phys. Chem.*, 1985, **89**, 2286–2291.
- 283 C. J. Gerack and L. McElwee-White, *Molecules*, 2014, **19**, 7689–7713.
- 284 N. Darla and S. Sitha, *J. Phys. Chem. A*, 2019, **123**, 8921–8931.
- 285 D. Shindell and C. J. Smith, *Nature*, 2019, **573**, 408–411.
- 286 F. Lin, Z. Dong, Y. Yao, L. Yang, F. Fang and L. Jiao, *Adv. Energy Mater.*, 2020, **10**, 2002176.
- 287 H. Bünger, *Chem. Ing. Tech.*, 1990, **62**, 434.
- 288 G. Li, J. Yu, J. Jia, L. Yang, L. Zhao, W. Zhou and H. Liu, *Adv. Funct. Mater.*, 2018, **28**, 1801332.
- 289 Z. H. Zhu, B. H. Zhao, S. L. Hou, X. L. Jiang, Z. L. Liang, B. Zhang and B. Zhao, *Angew. Chem., Int. Ed.*, 2021, **60**, 23394–23402.
- 290 L. Fan, C. Xia, P. Zhu, Y. Lu and H. Wang, *Nat. Commun.*, 2020, **11**, 3633.
- 291 B. Shan, S. Vanka, T.-T. Li, L. Troian-Gautier, M. K. Brennaman, Z. Mi and T. J. Meyer, *Nat. Energy*, 2019, **4**, 290–299.
- 292 M. Rumayor, A. Dominguez-Ramos, P. Perez and A. Irabien, *J. CO<sub>2</sub> Util.*, 2019, **34**, 490–499.
- 293 P. Zhu and H. Wang, *Nat. Catal.*, 2021, **4**, 943–951.

- 294 A. Vasileff, Y. Zhu, X. Zhi, Y. Zhao, L. Ge, H. M. Chen, Y. Zheng and S. Z. Qiao, *Angew. Chem., Int. Ed.*, 2020, **59**, 19649–19653.
- 295 X. Wang, Y. Jiao, L. Li, Y. Zheng and S. Z. Qiao, *Angew. Chem., Int. Ed.*, 2022, **61**, 202114253.
- 296 A. Wuttig, C. Liu, Q. Peng, M. Yaguchi, C. H. Hendon, K. Motobayashi, S. Ye, M. Osawa and Y. Surendranath, *ACS Cent. Sci.*, 2016, **2**, 522–528.
- 297 X. Zhou, J. Dong, Y. Zhu, L. Liu, Y. Jiao, H. Li, Y. Han, K. Davey, Q. Xu, Y. Zheng and S. Z. Qiao, *J. Am. Chem. Soc.*, 2021, **143**, 6681–6690.
- 298 S. Zhu, B. Jiang, W. B. Cai and M. Shao, *J. Am. Chem. Soc.*, 2017, **139**, 15664–15667.
- 299 K. Yamaguchi, H. Kobayashi, T. Oishi and N. Mizuno, *Angew. Chem., Int. Ed.*, 2012, **51**, 544–547.
- 300 K. Yamaguchi, M. Matsushita and N. Mizuno, *Angew. Chem., Int. Ed.*, 2004, **43**, 1576–1580.
- 301 T. Oishi, K. Yamaguchi and N. Mizuno, *Angew. Chem., Int. Ed.*, 2009, **48**, 6286–6288.
- 302 P. Daw, A. Kumar, N. A. Espinosa-Jalapa, Y. Ben-David and D. Milstein, *J. Am. Chem. Soc.*, 2019, **141**, 12202–12206.
- 303 L. Zhang, W. Wang, A. Wang, Y. Cui, X. Yang, Y. Huang, X. Liu, W. Liu, J.-Y. Son, H. Oji and T. Zhang, *Green Chem.*, 2013, **15**, 2680.
- 304 C. Gunanathan, Y. Ben-David and D. Milstein, *Science*, 2007, **317**, 790–792.
- 305 W. J. Sun, H. Q. Ji, L. X. Li, H. Y. Zhang, Z. K. Wang, J. H. He and J. M. Lu, *Angew. Chem., Int. Ed.*, 2021, **60**, 22933–22939.
- 306 S. Bähn, S. Imm, L. Neubert, M. Zhang, H. Neumann and M. Beller, *ChemCatChem*, 2011, **3**, 1853–1864.
- 307 K. Das, R. Shibuya, Y. Nakahara, N. Germain, T. Ohshima and K. Mashima, *Angew. Chem., Int. Ed.*, 2012, **51**, 150–154.
- 308 G. Hahn, P. Kunnas, N. de Jonge and R. Kempe, *Nat. Catal.*, 2018, **2**, 71–77.
- 309 S. Gomez, J. A. Peters and T. Maschmeyer, *Adv. Synth. Catal.*, 2002, **344**, 1037–1057.
- 310 K. Tokmic, B. J. Jackson, A. Salazar, T. J. Woods and A. R. Fout, *J. Am. Chem. Soc.*, 2017, **139**, 13554–13561.
- 311 D. B. Bagal and B. M. Bhanage, *Adv. Synth. Catal.*, 2015, **357**, 883–900.
- 312 M. Yuan, J. Chen, Y. Bai, Z. Liu, J. Zhang, T. Zhao, Q. Shi, S. Li, X. Wang and G. Zhang, *Chem. Sci.*, 2021, **12**, 6048–6058.
- 313 L. Pan, J. Wang, F. Lu, Q. Liu, Y. Gao, Y. Wang, J. Jiang, S. Chao, J. Wang and X. Wang, *Angew. Chem., Int. Ed.*, 2022, **62**, e202216835.